CZECH TECHNICAL UNIVERSITY IN PRAGUE

Faculty of Mechanical Engineering
Department of Technical Mathematics

MASTER'S THESIS

Numerical simulations of atmospheric fluids flows using finite volume method

Numerické simulace atmosférického proudění užitím metody konečných objemů

Vít Uhlíř

2022/2023

Declaration

I declare that I have prepared this thesis independently and I have only used the literature sources and information that I cite and list in the attached list of reference literature. I agree to lending of the thesis and its publication.

Date: Signature:

Acknowledgment

First and foremost, I would like to thank doc. Ing. Tomáš Bodnár, Ph.D., for his immense willingness, patience, helpful approach and extremely valuable advice and insights during the years of our cooperation. In addition, I would like to express my appreciation of the whole Department of Technical Mathematics at CTU, for all the information and skills I had been given opportunity to develop. The approach and enthusiasm of the all the members of the department was very helpful throughout the whole study.

Furthermore, I would like to thank all my family and friends, who have been supportive and created psychological well-being throughout my studies. Special thanks belongs to my dearest Verča for her support, for sharing and highlighting the good times and enduring the hard ones.

MASTER'S THESIS ASSIGNMENT

I. Personal and study details

Student's name: **Uhlíř Vít** Personal ID number: **466633**

Faculty / Institute: **Faculty of Mechanical Engineering**

Department / Institute: **Department of Technical Mathematics**

Study program: **Applied Sciences in Mechanical Engineering**

Specialisation: **Mathematical Modeling in Engineering**

II. Master's thesis details

Master's thesis title in English:

Numerical simulations of atmospheric fluids flows using finite volume method

Master's thesis title in Czech:

Numerické simulace atmosférického proudění užitím metody konečných objemů

Guidelines:

Bibliography / sources:

[1] Feistauer, M., Felcman, J., Straškraba, I.: Mathematical and Computational Methods for Compressible Flow. Clarendon Press, Oxford, 2003, ISBN 0-19-850588-4.
[2] Lions, P.L.: Mathematical Topics in Fluid Mechanics: Volume 1: Incompressible Models, Oxford Lecture Series in Mathematics and Its Applications, Clarendon Press 1996, ISBN 10: 0198514875ISBN 13: 9780198514879
[3] Viollet, P.L.: Mècanique des fluides à masse volumique variable. Presses de l'ecole nationale des ponts et chausées, 1997.
[4] Hirsch, C.: Numerical computation of internal and external flows, vol. 1,2. John Willey & Sons, 1988.
[5] Dvořák, R., Kozel, K.: Matematické modelování v aerodynamice, Vydavatelství ČVUT, 1996.

Name and workplace of master's thesis supervisor:

doc. Ing. Tomáš Bodnár, Ph.D. Department of Technical Mathematics FME

Name and workplace of second master's thesis supervisor or consultant:

Date of master's thesis assignment: **18.04.2023** Deadline for master's thesis submission: **13.08.2023**

Assignment valid until: _____

doc. Ing. Tomáš Bodnár, Ph.D. Supervisor's signature	prof. Ing. Jiří Fürst, Ph.D. Head of department's signature	doc. Ing. Miroslav Španiel, CSc. Dean's signature

III. Assignment receipt

The student acknowledges that the master's thesis is an individual work. The student must produce his thesis without the assistance of others, with the exception of provided consultations. Within the master's thesis, the author must state the names of consultants and include a list of references.

Date of assignment receipt	Student's signature

Abstract

The Master's thesis deals with numerical simulations of atmospheric flows. First part of the work is devoted to the physical description of the problem of flows in the atmospheric boundary layer. It is followed by formulation of mathematical model and description of numerical methods. Thereafter, the work contains results of simulations, based mainly on finite volume method and conducted using a self-developed code. First, validation of the custom code on test cases is presented. After validation, more complex cases are simulated and studied. The studied problems consist of two-dimensional cases of flows over hills of different shapes in the atmospheric boundary layer. Apart from discussion of the physical impacts of hills, flow regimes and density stratification, impacts of different numerical approaches are also demonstrated. The investigation includes comparison of the simulations with experimental data, comparison of different numerical methods and demonstration of the effects of different numerical parameters.

Keywords: numerical simulations, atmospheric flows, variable density, turbulence, finite volume method, discretization

Abstrakt

Magisterská práce se zabývá numerickými simulacemi atmosférického proudění. První část práce je věnována fyzikálnímu popisu problému proudění v mezní vrstvě atmosféry. Následuje formulace matematického modelu a popis numerických metod. Dále práce obsahuje výsledky simulací, založených především na metodě konečných objemů a provedených pomocí vlastnoručně vyvinutého kódu. Nejprve je představena validace vlastního kódu na testovacích případech. Po ověření jsou simulovány a studovány složitější případy. Studované problémy se skládají z dvourozměrných případů proudění přes kopce různých tvarů v mezní vrstvě atmosféry. Kromě diskuse o fyzikálních dopadech kopců, režimů proudění a hustotní stratifikace jsou demonstrovány i dopady různých numerických přístupů. Zkoumání zahrnuje porovnání simulací s experimentálními daty, srovnání různých numerických metod a demonstraci vlivu různých numerických parametrů.

Klíčová slova: numerické simulace, atmosférické proudění, proměnná hustota, turbulence, metoda konečných objemů, diskretizace

Contents

Used symbols

Latin symbols

a	speed of sound
$\mathbb{D}$	tensor of deformation
$\boldsymbol{f}$	heat flux
$\mathcal{F}, \mathcal{G}$	vectors of inviscid fluxes
g	gravity acceleration
h	hill height
H	height of the computational domain
k_T	thermal diffusion coefficient
L	the length of the computational domain
L_1	half-length of the hill
ℓ	mixing length
ℓ_∞	free stream mixing length
m	mass
M	Mach number
n_t	number of iterations
n_x, n_y	number of cells in corresponding direction
p	pressure
p_{in}	inlet pressure value
p_{out}	outlet pressure value
$\boldsymbol{q}$	heat flux
r	location of the reattachment
Re	Reynolds number
Ri	Richardson number
$\mathcal{R}, \mathcal{S}$	vectors of viscous fluxes
s	slope of the hill
t	time
Δt	time-step
T	temperature
$\boldsymbol{u} = (u, v, w)$	velocity
u_{max}	maximum velocity
u_r	norm of the difference of velocities
U	internal energy
V	volume
$\mathcal{W}$	vector of unknowns
x_h	location of the centre of the hill
x, y, z	coordinates
$\Delta x, \Delta y, \Delta z$	spatial steps

Greek symbols

α	tilt angle of the plate
β	artificial compressibility coefficient
γ	density gradient vector
δ	depth of the boundary layer
Δ	Laplace operator
∇	Hamilton operator
κ	diffusion coefficient
$\varkappa$	von Kármán's constant
λ	viscosity coefficient
μ	dynamic viscosity
ν	kinematic viscosity
ρ	density
τ	shear stress

Subscripts and superscripts

a_e	value from experiment
a_s	value from simulations
a_T	turbulent component
a_0	background value
a'	perturbation
a''	fluctuation component
$\overline{a}$	mean value
a^*	characteristic value
a^a	value from analytical solution

1 Introduction

1.1 Aim of the work

Aim of the work is to describe the physical aspects of flows in the atmospheric boundary layer (ABL) and to provide results of numerical simulations that are intended to represent the real flow in a simplified way. The atmospheric boundary layer represents a complicated physical problem because of many aspects involved.

The situation in ABL is rarely simple and involves turbulent flows of a fluid with non-constant density, which is, moreover, generally speaking compressible. In addition, the Earth's surface adds complexity to the problem with roughness of the surface and even more so with the many different obstacles in the form of hills, trees, buildings etc.

Despite the complexity, the study of the nature of ABL is of great public interest, because it is closely related to people's daily lives. It is not only about the general weather conditions, temperature changes, but also about wind situation or nowadays even more arising question of air pollution and spread of the pollutants. A good understanding of the flow in the ABL can lead to suitable siting and maximization of the efficiency of wind turbines, appropriate location of buildings, power plants and industrial factories in order to improve human live and prevent and avoid dangerous situations and disasters.

Unfortunately, it is very difficult and extremely resource-demanding to measure every aspect of ABL and to conduct experiments correctly reflecting the reality may be even of the same level of difficulty. Therefore, a great effort is made to try to simulate the flows and provide some understanding of the nature with models as simple as possible. The aim of this work is not to offer a solution to these largely complicated problems and resolve a concrete issue. This work follows the path of trying to find the simplest possible way how to simulate flows close to reality and provide valuable results in order to improve understanding of the atmospheric flows. The work provides description of the physical aspects of fluid flows in ABL and presents results of numerical simulations of simplified problems with a newly (from scratch) developed numerical solver using mainly the Finite Volume Method.

The custom code is first validated on basic problems with analytical solutions and at each subsequent step more complexity is added in order to reduce the gap with reality. The simplicity of the problems go from laminar flow of incompressible fluid with density between two flat plates, over flow of a fluid with varying density (stratified fluid) up to turbulent flows over hills of different shapes.

The value of the work can also be found in the expression of the problems that were found along the way and in the implementation and testing of many different approaches. The remarks, conclusions, solutions as well as mistakes may serve well in order to improve the future work of any author in the field of mathematical modelling a numerical simulations.

1.2 Structure of the work

The work is divided to seven sections. The first section serves as **introduction** to the topic in general and a description of the scope of the thesis.

Second section provides **physical description** of the topic. It focuses on describing the physical phenomena associated with the atmospheric fluids flows. All the necessary physical properties are introduced and their significance explained.

Following is the chapter of **mathematical model**. That provides mathematical formulation of the problem, necessary simplifications involved in the model and brief derivation of the governing equations.

Then directly follows the section with detailed description of the **numerical methods** used. That involves Finite Difference Method, already used in previous work, and Finite Volume Method as a more advanced method. In addition, the section provides the description and discussion of the modelling of obstacles (reflecting e.g. hills) used in numerical solver.

Chapter five demonstrates **Validation** of the numerical solver. The methods described in the previous section are set out to test on different well-known and commonly used physical problems of fluid flows that have existing analytical solution for easy comparison.

After validation, more complicated problems are introduced and evaluated in the section **Numerical experiments**. It involves several different set-ups that were numerically solved with described methods in different conditions and using different in-put parameters.

In the final section **Conclusion & Remarks** everything above is summarized and discussed. It involves general conclusions of the work, of the accomplishments, mistakes, contributions and lessons learnt. In addition, possibilities for continuing work are described.

2 Physical description

This section provides description of important terms, definitions and parameters in fluid flows with further specification for the atmosphere.

2.1 Fluid flow

When a shear force is applied to the surface of a fluid, the fluid undergoes a continuous change in shape (deformation) and the shear stress is usually proportional to the rate of change of the deformation, see for example the classic book [1] from Anderson.

The ability of a fluid to transfer this shear stress, or in other words: the resistance to deformation at a given rate, is called *viscosity*. Meaning, viscosity gives an information about the tendency of a fluid to flow. There are two types of this important property of a fluid: *kinematic* and *dynamic viscosity*. As it is stated, for instance, in [14], dynamic viscosity is formally defined through Newton's law of friction:

$$\tau = \mu \frac{\partial u}{\partial y} \quad [N \cdot m^{-2}], \tag{2.1}$$

where τ is the shear stress, μ the *dynamic viscosity* $[Pa \cdot s]$ and $\frac{\partial u}{\partial y}$ is a shear rate of deformation, given by a gradient of velocity in the direction perpendicular to the surface. Figure 1 shows an example of velocity profile near the surface, where the proportionality of shear stress to velocity gradient is illustrated.

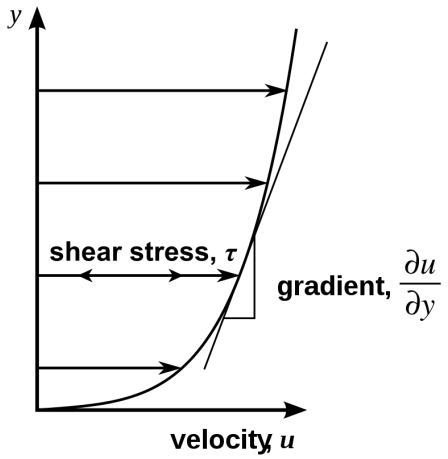

Figure 1: Shear stress, velocity gradient from

Kinematic viscosity is closely linked to dynamic viscosity in relation:

$$\nu = \frac{\mu}{\rho} \quad [m^2.s^{-1}], \tag{2.2}$$

where ρ is the *density* of the fluid.

Viscosity and density, very well-known and important properties of a fluid, are generally non-constant. In some cases, the neglect of the viscous forces can be justified due to their insignificance in a given problem, however flow in ABL is certainly not one of them. Viscosity cannot be neglected due to high importance of frictional forces at the Earth's surface and the interactions of frictional and inertial forces in the atmospheric flows of turbulent nature.

Density of a fluid can vary due to different reasons. First, the density change can be caused by pressure. Flows where fluids change their volume (density) under pressure change are called *compressible flows*. Most of the technical literature, as for example [1], refers to flows where the density of the fluid does not change as *incompressible*. However, to be precise, the incompressibility implies only that the pressure does not cause a significant change in density. In fact, incompressibility refers only to the conservation of volume as the pressure changes. Constant density is actually

an additional condition. In reality, the density of incompressible flows can vary, for example by mixing fluids with different densities.

In nature, generally every fluid is compressible. However, there are a large number of aerodynamic problems that can be modelled as being incompressible without significant loss of accuracy. In fact, it is a common practice to safely treat the flow incompressible when the flow velocity corresponds to Mach number $M < 0.3$. To be complete, Mach number is a dimensionless quantity defined as the ratio of flow velocity u and the local speed of sound a:

$$M = \frac{u}{a}, \tag{2.3}$$

At these velocity values the compression due to the flow is negligible. The compressible flows are mainly relevant to high speed flows which are not the objective of this work. Therefore, the approach in this work is to treat the flows as incompressible in all cases. However, given the interpretation of incompressibility in the previous paragraphs, we include the option of variable density to our model.

In addition, the studied fluid may consist of layers with different density (stratified fluid), caused by temperature differences or presence of additional particles or fluids. This situation is exactly what this work presents. The mathematical model is simplified by treating the flows as incompressible, but the more advanced cases in the numerical simulations involve stratification of the fluid in order to get closer to reality and to demonstrate the impacts of (commonly neglected) non-constant density.

In general, the flow of a fluid is always governed, as any other mechanical system, by the general laws of conservation. Specifically by the conservation of mass, momentum and energy. These laws and the governing equations for our problem will be expressed in detail further on.

2.2 Stratification

General meaning of stratification has already been explained in the section above. Here are presented the types of stratifications and the consequences associated with it. In addition, we want to clearly distinguish and express the limitation of the concept of stratification in this work only to density stratification due to the effect of gravitational forces.

The types of stratification include: neutral, stable and unstable. Neutral stratification means, that the fluid's density actually does not vary and stays the same throughout the whole domain. It can be referred to it as that the fluid is not stratified.

Stable stratification denotes that the density decreases with the distance in the opposite direction to the act of gravity, vertical direction. Each layer of fluid is thus less dense than the one below it. As the gravity acts on the fluid, the layers remain stable, because the layer with the greatest mass (density) already lies at the bottom. As the [33] states, stable boundary layers can be generated by the advection of warm air over a colder surface, for example by flow of warm air from land over colder coastal waters. However, according to another source [26], radiative cooling of the ground surface, as occurs with nocturnal conditions under relatively clear skies, is the most common source of stable boundary layers.

Unstable stratification indicates the exact opposite. The least dense layer lies at the bottom and the density gradually increases in each layer above. Therefore, the gravitational force causes movement, mixing of the layers in order to reach a stable state again. It evokes additional motion of the fluid that has significant effects in the total flow. Unstable condition in the atmosphere may occur as a result of local weather and is highly variable through distance and time, see [33].

The type of stratification can be described by the so-called *Richardson number*. It is a dimensionless quantity, that in our case involves the ratio of density gradient and velocity gradient, as reads:

$$Ri = \frac{g}{\rho^*} \frac{\gamma}{\sum_{i=1}^{3} (\frac{\partial u_i}{\partial z})^2}, \tag{2.4}$$

where g is the standard gravity, ρ^* the characteristic density, and $\gamma = -\frac{\partial \rho}{\partial z}$ is a vector parallel to gravity acceleration expressing the density gradient. In our cases, ρ^* is usually the prescribed

value at the ground, details will be provided in each individual case. The following Figure 2 shows graphically the types of density stratification with the corresponding Richardson number.

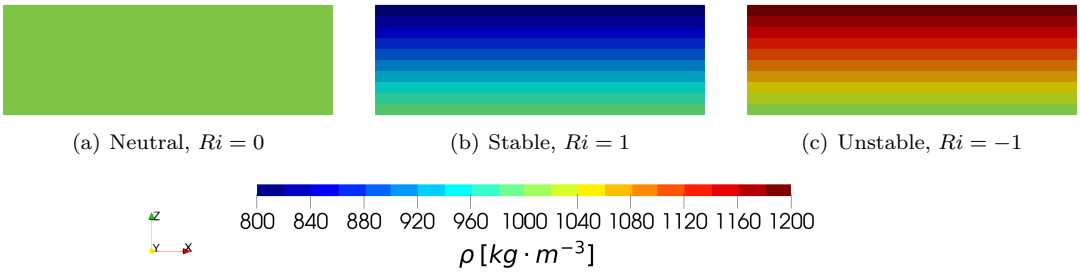

(a) Neutral, $Ri = 0$ (b) Stable, $Ri = 1$ (c) Unstable, $Ri = -1$

Figure 2: Types of stratification

In the atmosphere, it is very common to witness all types of stratification. Usually, the density changes in cycles during the day due to external influences such as solar radiation, nocturnal cooling of the ground, the presence of snow, emissions emitted by humans. Usually, during the day, when the Earth's ground absorbs the solar energy and heats up the air from below, an unstably stratified atmosphere slowly develops and vice versa at night when the Earth's surface cools down and the air becomes stably stratified. In reality, the situation is as always more complex with additional influences involved. Nevertheless, the effect of stratification near the surface should not be neglected in order to reflect reality more precisely. Therefore, this study includes stratification and the consequent effects will be shown in further sections with numerical experiments.

2.3 Turbulence

One very important aspect of a flow was not yet discussed and that is the flow regime. The flow can be either *laminar* or *turbulent*. Laminar flow, as explained for example in [38], is when the particles of a fluid follow smooth path in layers with each layer moving smoothly past the adjacent layers without mixing. Turbulent flow on the other hand, involves mixing, chaotic movement and eddies. The difference can be observed in Figure 3. Again, the more complex turbulent flow is more common in nature and the effects of turbulence cannot be neglected.

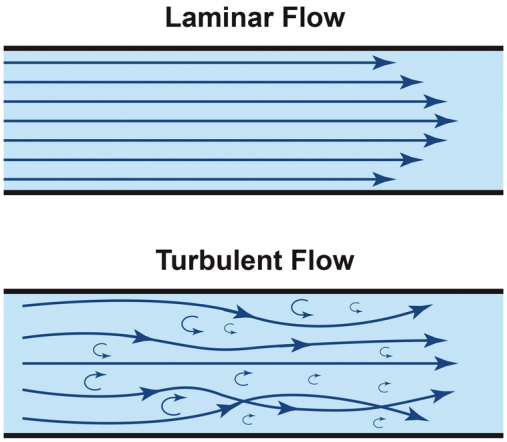

Figure 3: Flow regimes, adapted from [32]

The regime of the flow is commonly denoted by the so called *Reynolds number*. This dimensionless quantity gives the ratio of inertial to viscous forces and is given by:

$$Re = \frac{u^* \cdot L^*}{\nu}, \tag{2.5}$$

where ν is previously defined kinematic viscosity, u^* the characteristic velocity of the fluid and L^* is the characteristic linear dimension. When Reynolds number reaches a certain critical number, the laminar flow regime transforms to turbulent. As [38] describes, turbulence is a non-stationary motion of a fluid that involves vorticity with whirls of different sizes, turbulent transport of momentum, mass and heat, non-deterministic changes in time and dissipation of kinetic energy.

Therefore, modelling turbulent flows is a very complicated and challenging task. Statistical approaches and averaging of the turbulences are used to simplify the problem. However, the main challenge is to find a model that is both accurate enough for the problem at hand and simple enough to keep the computational cost reasonable. Later in this work, simple but elegant approach to turbulence modelling will be described in detail.

2.4 Atmhospheric boundary layer

In the atmospheric context, it has never been easy to define precisely what the boundary layer is. Nevertheless, a useful working definition, see [14], identifies the boundary layer as the layer of air directly above the Earth's surface in which the effects of the surface (friction, heating and cooling) are felt directly on time scales less than a day, and in which significant fluxes of momentum, heat or matter are carried by turbulent motions on a scale of the order of the depth of the boundary layer or less.

In the atmospheric boundary layer, turbulence plays a crucial role. Not only that the flows are chaotic (turbulences are generated) due to variation of wind speeds or changes in temperature (density stratification), but the flows in ABL also interact with the mean flow caused by the rotation of the Earth. This is the main difference between flows in nature and those created in wind tunnels. Nevertheless, study of atmospheric flows, although simplified, in wind tunnels and using numerical simulations provide valuable insight and useful results in well set up cases.

The ABL can be further divided, first into outer layer (or so-called Ekman layer), where Coriolis force caused by Earth's rotation plays an important role and is quite independent from the surface. The other sublayer consist of inner region where the roughness of the Earth's surface cannot be neglected. The division of the sublayers can be seen in the following Figure 4. The inner sublayer

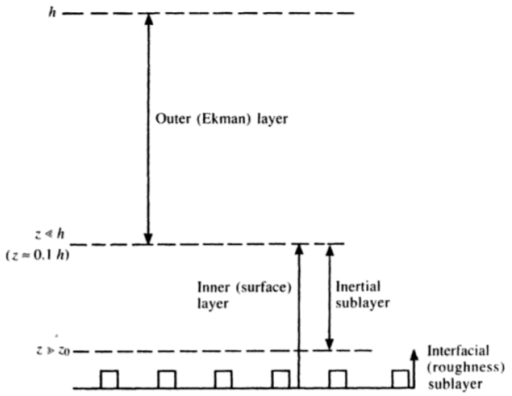

Figure 4: The Atmospheric Boundary Layer, adapted from [14]

is a case where the rotation of the Earth is of little importance. Different sources differ on the exact region of influence, but for example [18] states that within 50-100m from the ground, the flow is insensitive to Earth's rotation. Turbulences arise in this region mainly due to friction caused by roughness of the surface. Therefore, the inner sublayer can rather accurately be modelled and studied in wind tunnels. In addition, as [14] describes, the inertial sublayer is the region within which the velocity profile in neutrally buoyant conditions is logarithmic. Which provides useful information about expected results for wind tunnel testing or numerical simulations.

It is the inner sublayer, that is also the main objective of this work. Moreover, the influence of the roughness and the approach of modelling the surface will be thoroughly discussed in the following sections and numerical experiments.

3 Mathematical model

3.1 Governing equations

The flow of a fluid is commonly described by partial differential equations that are derived from the general laws of conservation. Therefore, the governing equations include the laws of conservation of mass, momentum and energy.

Complete derivation of the equations is not the purpose of this text. The approach was also already presented in bachelor's thesis preceding this work [36]. For the more rigorous and specific description you may, for example, go to [10], which is also the main source for this section. The origin and the resulting form of the equations alongside with the assumptions made are described in the following paragraphs. In addition, the specific used forms of equations are expressed and discussed in each of the simulated problems presented later on in this work.

3.1.1 Conservation of mass

Following [10], the conservation of mass can be expressed in a differential form:

$$\frac{\partial \rho}{\partial t} + \sum_{j=1}^{3} \frac{\partial(\rho u_j)}{\partial x_j} = 0 \tag{3.1}$$

We can rewrite the equation (3.1) to more compact form using the vector notation:

$$\frac{\partial \rho}{\partial t} + \operatorname{div}(\rho \boldsymbol{u}) = 0 \tag{3.2}$$

The above equation is also called the **Continuity equation**. In this from, it is valid for any fluid. However, in many cases it is possible to make simplifications. When we consider the density ρ constant, the equation 3.2) reduces to:

$$\operatorname{div}\boldsymbol{u} = 0 \tag{3.3}$$

3.1.2 Conservation of momentum

In general form, again following [10] and using vector notation, we can express the conservation of momentum ($\rho \boldsymbol{u}$) in the conservative form as:

$$\frac{\partial(\rho \boldsymbol{u})}{\partial t} + \operatorname{div}(\rho \boldsymbol{u} \otimes \boldsymbol{u}) = \rho \boldsymbol{f} - \operatorname{grad} p + \operatorname{grad}(\lambda \operatorname{div} \boldsymbol{u}) + \operatorname{div}(2\mu \mathbb{D}(\boldsymbol{u})) \tag{3.4}$$

On the left hand side, the first term desribes time-dependent acceleration, second term convection. The terms on the right hand side express the external forces, where the vector $\boldsymbol{f}$ stands for volume forces, p denotes pressure, λ viscosity coefficient, μ dynamic viscosity and $\mathbb{D}$ tensor of deformation velocity defined as:

$$\mathbb{D} = (d_{i,j}) = \frac{1}{2}\left(\frac{\partial u_i}{\partial x_j} + \frac{\partial u_j}{\partial x_i}\right), \tag{3.5}$$

where i, j here and also in all the following expressions in this chapter denotes $i, j = 1, 2, 3$.

For greater clarity, the equations can be rewritten component-wise:

$$\frac{\partial(\rho u_i)}{\partial t} + \sum_{j=1}^{3} \frac{\partial(\rho u_j u_i)}{\partial x_j} = \rho f_i - \frac{\partial p}{\partial x_i} + \frac{\partial}{\partial x_i}\left(\lambda \sum_{j=1}^{3} \frac{\partial u_j}{\partial x_j}\right) + \sum_{j=1}^{3} \frac{\partial}{\partial x_j}\left(\mu\left(\frac{\partial u_i}{\partial x_j} - \frac{\partial u_j}{\partial x_i}\right)\right) \tag{3.6}$$

Assumption is made concerning the volume forces $\boldsymbol{f}$. As it was described in the previous section, for atmospheric boundary layer close to the ground we can neglect the Earth's rotation. Thus $\boldsymbol{f}$ will reduce only to gravitational forces $\boldsymbol{g}$.

Moreover, if we take into account the assumption of incompressibility, that is the requirement of divergence-free velocity field, the third therm on the right hand side (involving divergence of velocity) will disappear along with part of the last term and we get the following form:

$$\frac{\partial(\rho u_i)}{\partial t} + \sum_{j=1}^{3} \frac{\partial(\rho u_j u_i)}{\partial x_j} = \rho g_i - \frac{\partial p}{\partial x_i} + \sum_{j=1}^{3} \frac{\partial}{\partial x_j}\left(\mu \frac{\partial u_i}{\partial x_j}\right) \tag{3.7}$$

When we apply the continuity equation (3.2) to the momentum equations (3.7) we can express the moment conservation in the non-conservative form:

$$\rho \frac{\partial u_i}{\partial t} + \rho \sum_{j=1}^{3} u_j \frac{\partial u_i}{\partial x_j} = \rho g_i - \frac{\partial p}{\partial x_i} + \sum_{j=1}^{3} \frac{\partial}{\partial x_j}\left(\mu \frac{\partial u_i}{\partial x_j}\right) \tag{3.8}$$

In addition, it can be simplified by dividing the equation (3.8) by the density ρ

$$\frac{\partial u_i}{\partial t} + \sum_{j=1}^{3} u_j \frac{\partial u_i}{\partial x_j} = g_i - \frac{1}{\rho}\frac{\partial p}{\partial x_i} + \sum_{j=1}^{3} \frac{\partial}{\partial x_j}\left(\nu \frac{\partial u_i}{\partial x_j}\right), \tag{3.9}$$

where ν represents previously defined kinematic viscosity.

3.1.3 Conservation of energy

In order to describe the flow in ABL with all real aspects, the law of conservation of energy has to be included. However, for our purposes and the problems studied, we do not necessarily need the equation. Since for incompressible flow, the energy equation is decoupled, solvable separately and not tied up with the equations of motion. Nevertheless, to be complete we present the conservation of energy in the form, following [20]:

$$\rho \frac{\partial U}{\partial t} + \rho \sum_{j=1}^{3} v_j \frac{\partial U}{\partial x_j} = -p\mathrm{div}\boldsymbol{u} + \lambda(\mathrm{div}\boldsymbol{u})^2 + \frac{1}{2}\sum_{j=1}^{3}\left(\frac{\partial u_i}{\partial x_j} + \frac{\partial u_j}{\partial x_i}\right)^2 + \rho q - \mathrm{div}\boldsymbol{q}, \tag{3.10}$$

where U denotes the internal energy and $\boldsymbol{q}$ the heat flux commonly described by Fourier's law:

$$\boldsymbol{q} = -k_t \mathrm{grad} T \tag{3.11}$$

In this equation k_t stands for thermal diffusivity coefficient and T for absolute temperature. In our cases

3.1.4 Navier-Stokes equations

In this work, mathematical model of incompressible flow is used with small adjustments in each case. The set of governing equations involving conservation of mass and momentum is often referred to as **Navier-Stokes equations**. Proper study of this model and justifications of the assumptions can be found in [23]. In our case, it consists of continuity equation (3.3) and equations of motion, for example in the form of (3.9). Here for the greater clarity it is presented in component-wise form with expressed equation for each component as follows:

$$\frac{\partial u}{\partial x} + \frac{\partial v}{\partial y} + \frac{\partial w}{\partial z} = 0 \tag{3.12}$$

$$\frac{\partial u}{\partial t} + u\frac{\partial u}{\partial x} + v\frac{\partial u}{\partial y} + w\frac{\partial u}{\partial z} = g_x - \frac{1}{\rho}\frac{\partial p}{\partial x} + \frac{\partial}{\partial x}\left(\nu\frac{\partial u}{\partial x}\right) + \frac{\partial}{\partial y}\left(\nu\frac{\partial u}{\partial y}\right) + \frac{\partial}{\partial z}\left(\nu\frac{\partial u}{\partial z}\right) \tag{3.13}$$

$$\frac{\partial v}{\partial t} + u\frac{\partial v}{\partial x} + v\frac{\partial v}{\partial y} + w\frac{\partial v}{\partial z} = g_y - \frac{1}{\rho}\frac{\partial p}{\partial y} + \frac{\partial}{\partial x}\left(\nu\frac{\partial v}{\partial x}\right) + \frac{\partial}{\partial y}\left(\nu\frac{\partial v}{\partial y}\right) + \frac{\partial}{\partial z}\left(\nu\frac{\partial v}{\partial z}\right) \tag{3.14}$$

$$\frac{\partial w}{\partial t} + u\frac{\partial w}{\partial x} + v\frac{\partial w}{\partial y} + w\frac{\partial w}{\partial z} = g_z - \frac{1}{\rho}\frac{\partial p}{\partial z} + \frac{\partial}{\partial x}\left(\nu\frac{\partial w}{\partial x}\right) + \frac{\partial}{\partial y}\left(\nu\frac{\partial w}{\partial y}\right) + \frac{\partial}{\partial z}\left(\nu\frac{\partial w}{\partial z}\right) \tag{3.15}$$

Alternatively, in conservative form we get:

$$\frac{\partial u}{\partial x} + \frac{\partial v}{\partial y} + \frac{\partial w}{\partial z} = 0 \tag{3.16}$$

$$\frac{\partial \rho u}{\partial t} + \frac{\partial \rho uu}{\partial x} + \frac{\partial \rho uv}{\partial y} + \frac{\partial \rho uw}{\partial z} = \rho g_x - \frac{\partial p}{\partial x} + \frac{\partial}{\partial x}\left(\mu \frac{\partial u}{\partial x}\right) + \frac{\partial}{\partial y}\left(\mu \frac{\partial u}{\partial y}\right) + \frac{\partial}{\partial z}\left(\mu \frac{\partial u}{\partial z}\right) \tag{3.17}$$

$$\frac{\partial \rho v}{\partial t} + \frac{\partial \rho uv}{\partial x} + \frac{\partial \rho vv}{\partial y} + \frac{\partial \rho vw}{\partial z} = \rho g_y - \frac{\partial p}{\partial y} + \frac{\partial}{\partial x}\left(\mu \frac{\partial v}{\partial x}\right) + \frac{\partial}{\partial y}\left(\mu \frac{\partial v}{\partial y}\right) + \frac{\partial}{\partial z}\left(\mu \frac{\partial v}{\partial z}\right) \tag{3.18}$$

$$\frac{\partial \rho w}{\partial t} + \frac{\partial \rho uw}{\partial x} + \frac{\partial \rho vw}{\partial y} + \frac{\partial \rho ww}{\partial z} = \rho g_z - \frac{\partial p}{\partial z} + \frac{\partial}{\partial x}\left(\mu \frac{\partial w}{\partial x}\right) + \frac{\partial}{\partial y}\left(\mu \frac{\partial w}{\partial y}\right) + \frac{\partial}{\partial z}\left(\mu \frac{\partial w}{\partial z}\right) \tag{3.19}$$

This set of equations serves for solving 4 unknowns: pressure p and three velocity components: $\boldsymbol{u} = (u, v, w)$ in the directions x, y, z. The density ρ and viscosity ν are here assumed not to vary. However, as previously stated, the situation in atmospheric flows is more complex and neither density nor viscosity are constants. In order to deal with the non-constant nature of these variables we introduce the **Boussinesq approximation**.

3.1.5 Boussinesq approximation

The main idea behind the Boussinesq approximation, first described in [5], is based on the idea that the density changes resulting from pressure changes are negligible. Therefore the non-constant nature of density comes only from temperature changes as they directly affect buoyancy. That allows us to use incompressible model = density not changing upon pressure changes.

In general, following [37], the density ρ and pressure p can be decomposed to large scale time-independent components denoted by subscript $_0$ and a small scale perturbation components marked with prime:

$$p(x, y, z, t) = p_0(z) + p'(x, y, z, t) \tag{3.20}$$

$$\rho(x, y, z, t) = \rho_0(z) + \rho'(x, y, z, t) \tag{3.21}$$

The background components denoted by $_0$ are assumed to vary only linearly in the vertical direction z. The perturbation components of much smaller magnitude containing the changes over time and in all directions. In addition, we assume the background components satisfying the hydrostatic equality equation:

$$\nabla p_0 = \rho_0 \boldsymbol{g} \tag{3.22}$$

The more detailed explanation behind this approximation and its application can be found, for example, in [37] or [6].

In the case of our system we apply the Boussinesq approximation of pressure and density to simplify the equations of motion. When we take the relations (3.20), (3.21) and insert them in (3.8) we result in:

$$(\rho_0 + \rho')\left(\frac{\partial u_i}{\partial t} + \sum_{j=1}^{3} u_j \frac{\partial u_i}{\partial x_j}\right) = \rho_0 g_i + \rho' g_i - \frac{\partial p_0}{\partial x_i} - \frac{\partial p'}{\partial x_i} + \sum_{j=1}^{3} \frac{\partial}{\partial x_j}\left(\mu \frac{\partial u_i}{\partial x_j}\right) \tag{3.23}$$

Applying the equation (3.22), we eliminate two terms on the right hand side. Now the next step is to divide the equation by the term $(\rho_0 + \rho')$. Assuming the density perturbation is much smaller, i.e. $\rho' \ll \rho_0$, we can replace the term by the background density ρ_0 alone. That leaves us with the following:

$$\frac{\partial u_i}{\partial t} + \sum_{j=1}^{3} u_j \frac{\partial u_i}{\partial x_j} = \frac{\rho'}{\rho_0} g_i - \frac{1}{\rho_0} \frac{\partial p'}{\partial x_i} + \sum_{j=1}^{3} \frac{\partial}{\partial x_j}\left(\nu \frac{\partial u_i}{\partial x_j}\right) \tag{3.24}$$

In addition, in order to be able to solve the density variable we derive one additional equation by applying the Boussinesq approximation on continuity equation. We take the equation expressing

conservation of mass in the form (3.1) with additional term representing diffusion mass transfer:

$$\frac{\partial \rho}{\partial t} + \nabla \cdot (\rho \boldsymbol{u}) = \nabla \cdot (\kappa \nabla \rho), \tag{3.25}$$

where κ is diffusion coefficient, which is part of corresponding source term, that is introduced to represent the local mass balance.

Again, assuming the incompressible model with divergence-free (div $\boldsymbol{u} = 0$) constraint and applying the Boussinesq approximation we get:

$$\frac{\partial \rho_0}{\partial t} + \frac{\partial \rho'}{\partial t} + \boldsymbol{u} \cdot \Delta \rho_0 + \boldsymbol{u} \cdot \Delta \rho' = \nabla \cdot (\kappa \nabla \rho_0) + \nabla \cdot (\kappa \nabla \rho') \tag{3.26}$$

The basis of the approximation is that the background density ρ_0 varies only linearly in the vertical direction z. Therefore, the first terms on both sides will disappear. After a slight rearrangement we can write:

$$\frac{\partial \rho'}{\partial t} + \boldsymbol{u} \cdot \Delta \rho' = \nabla \cdot (\kappa \nabla \rho') + \boldsymbol{u} \cdot \nabla \rho_0 \tag{3.27}$$

Considering the conservative form and following the same logic, we would get the equations:

$$\frac{\partial u_i}{\partial t} + \sum_{j=1}^{3} \frac{\partial (u_j u_i)}{\partial x_j} = \frac{\rho'}{\rho_0} g_i - \frac{1}{\rho_0} \frac{\partial p'}{\partial x_i} + \sum_{j=1}^{3} \frac{\partial}{\partial x_j} \left(\nu \frac{\partial u_i}{\partial x_j} \right) \tag{3.28}$$

$$\frac{\partial \rho'}{\partial t} + \nabla \cdot (\rho' \boldsymbol{u}) = \nabla \cdot (\kappa \nabla \rho') + \boldsymbol{u} \cdot \nabla \rho_0 \tag{3.29}$$

Now we have included the consideration of density stratification in our model and additional equation for computing the density perturbation ρ'. However, we have not yet addressed the variable viscosity and diffusivity included in the equations (3.24) and (3.27) or alternatively (3.28) and (3.29). In other words, the turbulence model has not yet been incorporated.

3.2 Turbulence modelling

The atmospheric flows are inevitably with the presence of turbulences, which are chaotic and thus very hard to predict or simulate. Therefore, modelling a turbulence becomes a very difficult task. Over the time several approaches to model turbulences were developed. The three basic methods are the following:

- **Direct Numerical Simulation (DNS)**
- **Large Eddy Simulasion (LES)**
- **Reynolds Averaged Navier-Stokes equations model (RANS)**

DNS is the most complex and accurate approach. It computes the fluid's motion at all temporal and spatial scales with the basic set of governing equations with no additional turbulence model involved. That leads to very high computational costs, which makes it unsuitable for the purpose of this work.

The principal idea behind **LES**, as described in [35], is to ignore (filter) the smallest scales, which are the most computationally expensive to resolve. Only the large scale eddies are resolved by the model equations, which reduces the computational costs, but additional small scale parametrization is necessary.

In **RANS** approach, originally proposed by [31], the flow quantities are decomposed into a mean (time-averaged) and fluctuating (turbulent) component. Mean flow field is then obtained by solving averaged equations and the turbulent fluctuations are resolved using suitable turbulence model. This approach is widely used and for its simplicity alongside with solid accuracy it is very well suited method for many application including problems studied in this work.

3.2.1 RANS model

Following [31], we decompose ρ', $\boldsymbol{u}$ and p' into a mean flow component and a turbulent fluctuation, namely

$$\rho' = \overline{\rho'} + \rho'', \qquad \boldsymbol{u} = \overline{\boldsymbol{u}} + \boldsymbol{u}'', \qquad p' = \overline{p'} + p'', \tag{3.30}$$

where $\overline{\rho}'$, $\overline{\boldsymbol{u}}$ and $\overline{p'}$ represent the mean quantities, and ρ'', $\boldsymbol{u}''$ and p'' the turbulent components. Plugging the decomposition (3.30) into (3.12), (3.24) and (3.27), averaging the equations, noting that the average of the turbulent fluctuations are zero, using vector notation we can write the following:

$$\nabla \cdot \overline{\boldsymbol{u}} = 0, \tag{3.31}$$

$$\frac{\partial \overline{\rho'}}{\partial t} + \overline{\boldsymbol{u}} \cdot \nabla \overline{\rho'} = \nabla \cdot \left(\kappa \nabla \overline{\rho'} \right) - \nabla \cdot \boldsymbol{h} - \overline{\boldsymbol{u}} \cdot \nabla \rho_0, \tag{3.32}$$

$$\left(\frac{\partial \overline{\boldsymbol{u}}}{\partial t} + (\overline{\boldsymbol{u}} \cdot \nabla) \overline{\boldsymbol{u}} \right) = - \frac{\nabla \overline{p'}}{\rho_0} + \nabla \cdot \left(\nu \nabla \overline{\boldsymbol{u}} \right) - \nabla \cdot \boldsymbol{\tau} + \frac{\overline{\rho'}}{\rho_0} \boldsymbol{g}, \tag{3.33}$$

where $h_j = \overline{\rho' u_j}$ and $\tau_{ij} = \overline{u_i u_j}$ are turbulent mass and momentum fluxes, respectively. For a detailed derivation see, for example, [14].

Furthermore, to completely determine the equations (3.31) - (3.33), we assume, as originally described in [5], that the turbulent fluxes can be written in terms of the flux-gradient approximation:

$$\boldsymbol{\tau} = -\nu_T \nabla \overline{\boldsymbol{u}}, \qquad \boldsymbol{h} = -\kappa_T \nabla \overline{\rho}, \tag{3.34}$$

where the turbulent viscosity ν_T and the turbulent diffusivity κ_T are quantities to be determined, for example, as functions of the average fields. This approximation leads to the following system of equations:

$$\nabla \cdot \overline{\boldsymbol{u}} = 0 \tag{3.35}$$

$$\frac{\partial \overline{\rho'}}{\partial t} + \overline{\boldsymbol{u}} \cdot \nabla \overline{\rho'} = \nabla \cdot \left((\kappa + \kappa_T) \nabla \overline{\rho'} \right) + \overline{\boldsymbol{u}} \cdot \boldsymbol{\gamma} \tag{3.36}$$

$$\frac{\partial \overline{\boldsymbol{u}}}{\partial t} + (\overline{\boldsymbol{u}} \cdot \nabla) \overline{\boldsymbol{u}} = - \frac{\nabla \overline{p'}}{\rho_0} + \nabla \cdot \left((\nu + \nu_T) \nabla \overline{\boldsymbol{u}} \right) + \frac{\overline{\rho'}}{\rho_0} \boldsymbol{g}, \tag{3.37}$$

or in conservative form:

$$\nabla \cdot \overline{\boldsymbol{u}} = 0 \tag{3.38}$$

$$\frac{\partial \overline{\rho'}}{\partial t} + \nabla \cdot \left(\overline{\rho'} \overline{\boldsymbol{u}} \right) = \nabla \cdot \left((\kappa + \kappa_T) \nabla \overline{\rho'} \right) + \overline{\boldsymbol{u}} \cdot \boldsymbol{\gamma} \tag{3.39}$$

$$\frac{\partial \overline{\boldsymbol{u}}}{\partial t} + \nabla \cdot \left(\overline{\boldsymbol{u}} \otimes \overline{\boldsymbol{u}} \right) = - \frac{\nabla \overline{p'}}{\rho_0} + \nabla \cdot \left((\nu + \nu_T) \nabla \overline{\boldsymbol{u}} \right) + \frac{\overline{\rho'}}{\rho_0} \boldsymbol{g}, \tag{3.40}$$

where $\boldsymbol{\gamma} = (0, 0, \gamma)$, with $\gamma = -\frac{\partial \rho_0}{\partial z}$ being a constant vector parallel to the gravity acceleration.

3.2.2 Mixing length model

In order to be able to determine the turbulent viscosity ν_T and the turbulent diffusivity κ_T a suitable turbulence model has to be introduced. There are many models existing with wide variety of complexity and accuracy. To name a few: one-equation models such as Mixing length, Spalart-Allmaras, or 2 equation models, namely $\kappa - \omega$, $\kappa - \epsilon$ or Reynolds stress equation model. Detailed description of the aforementioned is not the objective of this work. The focus will be only on the selected model.

For the purposes of studied problems, one simple but elegant algebraic model is used - **Mixing length model**. The main advantage is its plainness and the ease of implementation to the system.

However, even with this simple model many promising and accurate results were already reached by different authors, see for example [3] or [7].

The idea behind this model, originally proposed by [30], is that a parcel of fluid is keeping its original momentum for a characteristic length ℓ before mixing with the surrounding fluid. The velocities of the parcels arriving at the height z will be those of the neighbouring layers a distance ℓ away. Thus the neighbouring parcels arriving at height z contribute to the turbulent (fluctuating) velocity components of level z.

A relation between the turbulent viscosity and the mixing length ℓ has been originally proposed by [2]. It is based on the idea of replacing the velocity fluctuations by gradients of mean velocity components rescaled with ℓ. It takes into account the influence of changes in momentum in different directions. However, assumptions are made, that in ABL horizontal velocity gradients are omitted as negligible and that vertical velocity tends to zero, thus its gradients also negligible. That leaves us with the following formula for the turbulent viscosity $\nu_{_T}$:

$$\nu_{_T} = \ell^2 \left[\left(\frac{\partial \overline{u}}{\partial z} \right)^2 + \left(\frac{\partial \overline{w}}{\partial z} \right)^2 \right]^{1/2}, \tag{3.41}$$

with mixing length defined as:

$$\ell = \frac{\varkappa z}{1 + \frac{\varkappa z}{\ell_\infty}}, \tag{3.42}$$

where z is the distance from the ground, $\varkappa$ is von Kármán's constant and ℓ_∞ is a suitable asymptotic value such that $\ell \approx \ell_\infty$ at large distances from the ground.

Nevertheless, in order to take into account the effects of the stratification, the above model was generalized by [9] introducing a stability function $\mathcal{G}$ such that:

$$\nu_{_T} = \ell^2 \left[\left(\frac{\partial u}{\partial z} \right)^2 + \left(\frac{\partial w}{\partial z} \right)^2 \right]^{1/2} \cdot \mathcal{G}, \tag{3.43}$$

where

$$\begin{aligned} \mathcal{G} &= (1 + 3Ri)^{-2}, \qquad \text{for} \quad Ri > 0, \\ \mathcal{G} &= (1 - 3Ri)^{2}, \qquad \text{for} \quad Ri \leq 0. \end{aligned} \tag{3.44}$$

The Figure 5 shows the dependency of the stability function $\mathcal{G}$ on the Richardson number Ri with marking of the three specific values, used in simulations. Thus it is obvious, how the choice of Ri increases or lowers the magnitude of turbulent kinematic viscosity. For our purposes of density stratification Ri is determined by the formula (2.4).

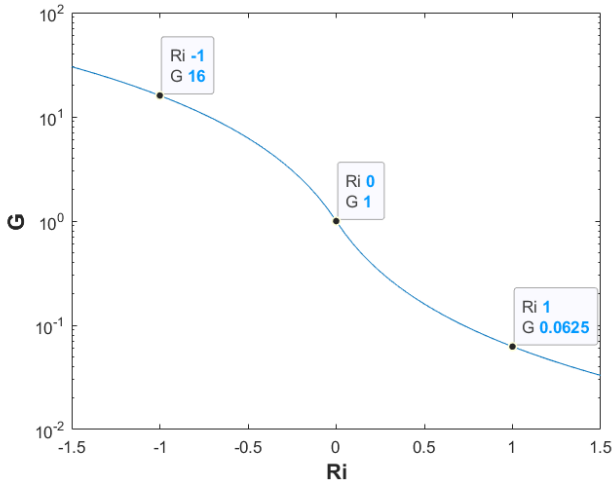

Figure 5: Graph of the stability function $\mathcal{G}$ versus the Richardson number

Finally, the turbulent diffusivity is expressed through the turbulent Prandtl number $Pr_{_T}$ as:

$$\kappa_{_T} = \frac{\nu_{_T}}{Pr_{_T}}. \tag{3.45}$$

The above mentioned relations contain several constants that were not yet discussed. Due to the reason that they may differ in individual cases, we will discuss the specific value in each case, where its necessary, separately in section of numerical experiments.

4 Numerical methods

In this section, all the numerical approaches used in order to discretize and solve the set of equations are described. Apart from the discretization provided by the numerical methods, additional **Artificial Compressibility Method** is used in order to be able to solve equation for necessary variable - pressure.

In regards of discretization, two basic and commonly used methods in CFD were used to study atmospheric flows. This work is a continuation of the previous bachelor's theses [36], where only the **Finite Difference Method** was used. On one hand, the method is straightforward and easy to implement. On the other hand, has its limits in terms of accuracy. Consequently, in this current work, more robust, versatile and powerful **Finite Volume Method** is incorporated in order to solve the more complex problems. This method is the most commonly used for the application of simulating fluid flows.

Finite Volume Method is the main objective of this work, however throughout the studied problems, obtained results and comparisons with the Finite Difference Method will be provided. For brevity and clear distinction, we introduce abbreviations for the two methods, which will be used in the rest of the work. **DIF** denotes the Finite Difference method and **FVM** the Finite Volume Method. In both methods, the **MacCormack scheme** plays crucial role. Although, the numerical scheme is the same, the implementation differs and will be explained for both cases. One other scheme and several modifications of the two were studied and tested. However, for the lack of improvement with the modifications, the results will not be presented within this work.

This section also contains the description of different approaches of meshing the computational domain and modelling an obstacle. The different ways of refining the domain are discussed along with differing approaches to represent obstacles within the domain. Naturally, many obstacles (such as hills, buildings, trees, ...) occur close to the ground. In this work, we study the flows over hills (=obstacles) that have to be modelled a certain way. Different meshing of the computational domain are studied in order to reflect reality as closely as possible. Again, comparison of simple approach of **Immersed Boundary method** used in the preceding work and more advanced **Wall Fitted Mesh** will be discussed.

In addition, last simplification involved will be made in terms of considered dimensions. Primarily to reduce the computational complexity, all the problems studied in this work were simplified to two dimensions. This approach will be justified and discussed in more detail later on specific cases. Nevertheless, due to this simplification the discretization in this section will also be shown only for two dimensions, which will add clarity to the explanation.

Therefore, from now on, we will only be using the horizontal direction x with corresponding velocity component u and vertical direction z with corresponding velocity component w. Correspondingly we introduce the discretization description and notation. Figure 6 shows the layout graphically,

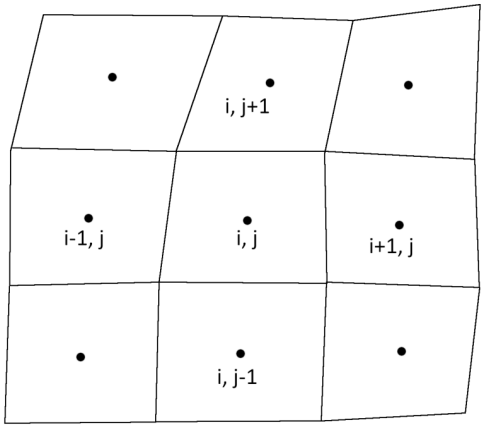

Figure 6: Stencil for numerical discretization

where i indicates the position in the x direction and j the position in the z direction.

4.1 Artificial Compressibility Method

In order to complete our model, additional method is necessary to be able to numerically solve for an indispensable variable - pressure. Artificial Compressibility Method, originally described in [8], is the method used in this work.

It is widely used approach to address the pressure in Navier-Stokes equations. More details about its derivation and application can be also found in [20] or [16]. The method is based on expanding the Continuity equation (3.3) to the form:

$$\frac{1}{\beta^2}\frac{\partial p}{\partial t} + \nabla \cdot \boldsymbol{u} = 0, \tag{4.1}$$

where β is the artificial compressibility coefficient. It has the dimension of speed and it can be also understood as the artificial speed of sound. It affects the course of the solution method but not the final result. In case, the solution converges to steady solution, the time derivative of pressure will become zero, thus the original form of continuity equation will be solved, see [3].

With the Artificial Compressibility Method implemented, we have the complete set of equations to be discretized and solved for every necessary variable.

4.2 Finite Difference Method (DIF)

Method of finite differences approximates the original set of differential equations itself. DIF is the oldest and most traditional method, which remains the reference for all studies of numerical discretization, although it is only applicable in practice to structured grids. [15]

The computational domain is discretized into mesh consisting of finite number of points in each direction and the derivatives are approximated with suitable proportional finite differences of the values at the neighbouring grid points. In addition, the boundary conditions are directly applied to the grid points located at the boundary of the computational domain. The finite differences approximating derivatives are based on Taylor series expansion with omitting the terms that are assumed to be negligible.

DIF was thoroughly explained with provided examples in the preceding thesis [36]. Therefore, it will not be here again studied in detail. Only general description of the differences replacing derivatives in the equations and the used numerical scheme is explained as follows.

For illustration, we provide the overview of the finite difference applied only to one spatial derivative. However, the exact same discretization can be made other space coordinates and for time. The basic approximations of the derivatives that occur in our mathematical models can be summarized, following [20] as:

Forward difference (First Order):

$$\frac{\partial u(x,t)}{\partial x} \approx \frac{u_{i+1} - u_i}{\Delta x} \tag{4.2}$$

Backward difference (First Order):

$$\frac{\partial u(x,t)}{\partial x} \approx \frac{u_i - u_{i-1}}{\Delta x} \tag{4.3}$$

Central difference (First Order):

$$\frac{\partial u(x,t)}{\partial x} \approx \frac{u_{i+1} - u_{i-1}}{2\Delta x} \tag{4.4}$$

Central difference (Second Order):

$$\frac{\partial^2 u(x,t)}{\partial x^2} \approx \frac{u_{i+1} - 2u_i + u_{i-1}}{\Delta x^2} \tag{4.5}$$

where u, in this case, represents an arbitrary general quantity and i the position of the point in the direction x .

4.2.1 Numerical schemes

Lax-Friedrichs, described for example in [22], is a simple explicit scheme that uses central differences (4.4), (4.5) to discretize spatial derivatives and forward difference (4.2) for time with replacement of previous value u_i^n by the average of the surrounding points $u_i^n = \frac{1}{2}(u_{i+1}^n + u_{i-1}^n)$.

This method is of first order of accuracy. It was previously used in order to test the setup of the problems and to provide first quick results. However, due to its accuracy limitations, the scheme was further left out and not used in the more complex problems involving turbulence flow. Thus, more accurate scheme was preferred and the results obtained with the use of Lax-Friedrichs will not be shown in this work.

MacCormack scheme, first published in 1969 by [25], belongs to the group of Lax-Wendroff schemes of second-order accuracy in both space and time. Lax-Wendroff schemes use central differences (4.4), (4.5) to discretize derivatives. However, the speciality of MacCormack scheme is a two-step approach. In the first step - *predictor* - it uses forward differencing (4.2), and in the second step - *corrector* - it follows with backward differencing (4.3), which together results in central difference.

This approach provides more accurate solution, than for example the Lax-Friedrichs. In addition, the scheme can be controlled and modified during each step of the computation, which offers various options for improving the simulations.

Since MacCormack scheme plays crucial role in our simulations, its application is provided for greater clarity. Following [21], we apply MacCormack scheme on the equation of motion (3.37) for the horizontal velocity component u, namely:

Predictor:

$$\begin{aligned} u_{i,j}^{n+1/2} = \; & u_{i,j}^n - \Delta t \left[\frac{p_{i+1,j}^n - p_{i,j}^n}{\rho_0 \Delta x} + u_{i+1/2,j}^n \frac{u_{i+1,j}^n - u_{i,j}^n}{\Delta x} + w_{i,j+1/2}^n \frac{u_{i,j+1}^n - u_{i,j}^n}{\Delta z} - \right. \\ & - \left(\frac{\nu_{i+1/2,j}^n \cdot \left(u_{i+1,j}^n - u_{i,j}^n\right) - \nu_{i-1/2,j}^n \cdot \left(u_{i,j}^n - u_{i-1,j}^n\right)}{\Delta x^2} + \right. \\ & \left. \left. + \frac{\nu_{i,j+1/2}^n \cdot \left(u_{i,j+1}^n - u_{i,j}^n\right) - \nu_{i,j-1/2}^n \cdot \left(u_{i,j}^n - u_{i,j-1}^n\right)}{\Delta z^2} \right) \right] \end{aligned} \tag{4.6}$$

Corrector:

$$\begin{aligned} u_{i,j}^{n+1} = \; & \frac{u_{i,j}^n + u_{i,j}^{n+1/2}}{2} - \frac{\Delta t}{2} \left[\frac{p_{i,j}^n - p_{i-1,j}^n}{\rho_0 \Delta x} + u_{i-1/2,j}^{n+1/2} \frac{u_{i,j}^{n+1/2} - u_{i-1,j}^{n+1/2}}{\Delta x} + w_{i,j-1/2}^{n+1/2} \frac{u_{i,j}^{n+1/2} - u_{i,j-1}^{n+1/2}}{\Delta z} - \right. \\ & - \left(\frac{\nu_{i+1/2,j}^{n+1/2} \cdot \left(u_{i+1,j}^{n+1/2} - u_{i,j}^{n+1/2}\right) - \nu_{i-1/2,j}^{n+1/2} \cdot \left(u_{i,j}^{n+1/2} - u_{i-1,j}^{n+1/2}\right)}{\Delta x^2} + \right. \\ & \left. \left. + \frac{\nu_{i,j+1/2}^{n+1/2} \cdot \left(u_{i,j+1}^{n+1/2} - u_{i,j}^{n+1/2}\right) - \nu_{i,j-1/2}^{n+1/2} \cdot \left(u_{i,j}^{n+1/2} - u_{i,j-1}^{n+1/2}\right)}{\Delta z^2} \right) \right]. \end{aligned} \tag{4.7}$$

Here the over bars for Reynolds averaged values and primes for perturbations already left out. Nevertheless, we still bear in mind all the approximations made in chapter 3. Moreover, to stay consistent with the (3.40), we consider the values of viscosity ν involving both the laminar and turbulent part.

4.3 Finite Volume Method (FVM)

Finite Volume Method is more versatile method that can be used on any type of mesh. The main part is to divide the computational domain into finite number of volumes (for instance hexahedral cells in 3D or quadrilateral cells in 2D). Regardless the number of dimensions, in **FVM** we always refer to these cells as volumes. Moreover, we do not have to limit ourselves only to structured grids and can even use unstructured grids (e.g. triangular shapes). Nevertheless, in this work we stay with the quadrilateral shapes to represent the domain.

In addition, there are also two main approaches to where to store the unknowns in the control volume. First, cell-centred approach, where the unknowns are stored at the centres and the grid lines define the finite volumes and surfaces. Second, the vertex-centred, where the unknowns are defined at the vertices (corners), thus the variables are attached to the mesh points. In this work, we strictly follow the cell-centred approach, therefore any mention of Finite Volume Method further on, is considered with unknowns located in the centre of the control volume.

The strength of FVM is its direct connection to the physical flow properties. As it is thoroughly described and derived in [15], the basis of the method relies on the direct discretization of the integral form of the conservation law. In contrast to DIF, where the differential form of the equations is discretized and the nodal values are used, in Finite Volume Method the terms are evaluated as fluxes at surfaces of each volume.

In order to clarify the discretization using the Finite Volume Method, let us rewrite the set of equation into a different vector form. First, we shorten the notation of partial derivatives as follows:

$$u_t = \frac{\partial u}{\partial t}, u_x = \frac{\partial u}{\partial x}, u_z = \frac{\partial u}{\partial z} \tag{4.8}$$

In addition we denote the meaning of newly defined vectors. First, vector $\mathcal{W}$ contains the computed quantities and $\mathcal{P}$ multiplying constants:

$$\mathcal{W} = \begin{pmatrix} p \\ \rho' \\ u \\ w \end{pmatrix}, \quad \mathcal{P} = \begin{pmatrix} \frac{1}{\beta^2} \\ 1 \\ 1 \\ 1 \end{pmatrix}, \tag{4.9}$$

inviscid flux vectors are defined as:

$$\mathcal{F} = \begin{pmatrix} u \\ \rho' u \\ u^2 + \frac{p}{\rho_0} \\ uw \end{pmatrix}, \quad \mathcal{G} = \begin{pmatrix} w \\ \rho' w \\ uw \\ w^2 + \frac{p}{\rho_0} \end{pmatrix} \tag{4.10}$$

Viscous fluxes are the following:

$$\mathcal{R} = \begin{pmatrix} 0 \\ (\nu + \nu_T)\rho'_x \\ (\nu + \nu_T)u_x \\ (\nu + \nu_T)w_x \end{pmatrix}, \quad \mathcal{S} = \begin{pmatrix} 0 \\ (\nu + \nu_T)\rho'_z \\ (\nu + \nu_T)u_z \\ (\nu + \nu_T)w_z \end{pmatrix} \tag{4.11}$$

Lastly, the vector representing the force effects in a stratified fluid:

$$\boldsymbol{f} = \begin{pmatrix} 0 \\ w \cdot \gamma \\ 0 \\ -\frac{\rho'}{\rho_0} g \end{pmatrix} \tag{4.12}$$

Then we can express our system of non-homogenous, two-dimensional Navier-Stokes equations in conservative form to model variable density incompressible flow, as follows:

$$\mathcal{P}\mathcal{W}_t + \mathcal{F}_x + \mathcal{G}_z = \mathcal{R}_x + \mathcal{S}_z + \boldsymbol{f} \tag{4.13}$$

This is the system used for Finite Volume Method in numerical simulations presented in this thesis.

Next we approach to the discretization of this system. In the derivation, we mostly follow [16]. First step is to integrate the set of equations over the control volumes. Each and individual control volume has its own corresponding set of equations. Since we consider only two dimensions, we will refer to the control volume as a 2D cell $D = D_{i,j}$.

Starting with rearrangement of the system (4.13):

$$\mathcal{P}\mathcal{W}_t + (\mathcal{F} - \mathcal{R})_x + (\mathcal{G} - \mathcal{S})_z = \boldsymbol{f} \tag{4.14}$$

after integrating over the cell D we get:

$$\mathcal{P}\int_D \mathcal{W}_t dS + \int_D (\mathcal{F}-\mathcal{R})_x dS + \int_D (\mathcal{G}-\mathcal{S})_z dS = \int_D \boldsymbol{f}\, dS \tag{4.15}$$

We can also combine the two integrals with spatial derivatives:

$$\mathcal{P}\int_D \mathcal{W}_t dS + \int_D \Big[(\mathcal{F}-\mathcal{R})_x + \int_D (\mathcal{G}-\mathcal{S})_z\Big] dS = \int_D \boldsymbol{f}\, dS \tag{4.16}$$

Next step is to apply Green's theorem, establishing a relationship between a line integral around a simple closed curve in a two-dimensional plane and a double integral over the region enclosed by that curve. For our given situation with structured grid and $dS = dxdz$, we replace the surface integral by line integral over the cell boundary ∂D and obtain:

$$\mathcal{P}\int_D \mathcal{W}_t dS + \oint_{\partial D} (\mathcal{F}-\mathcal{R})dz + (\mathcal{G}-\mathcal{S})dx = \int_D \boldsymbol{f}\, dS \tag{4.17}$$

Furthermore, if we denote $W_{i,j} = \frac{1}{|D|}\int_D \mathcal{W} dS$ as the cell average of $\mathcal{W}$ over the cell $D_{i,j}$, we can then rewrite (4.17) as:

$$P\frac{\partial W_{i,j}}{\partial t} + \frac{1}{|D|}\oint_{\partial D} (F-R)dz + (G-S)dx = \frac{1}{|D|}\int_D \boldsymbol{f}\, dS \tag{4.18}$$

Now to obtain fully discrete system we have to address the infinitesimal integrals and derivations. As it was proposed earlier in this work, we deal with it using MacCormack scheme. Thus, we choose the discrete approach. Meaning the integrals both in space and time are approximated simultaneously into discrete form. However, in order to discretize both inviscid and viscous forces (involving additional derivation), we are forced to construct two adjoint finite volume meshes as it is depicted in the Figure 7, where solid lines represent the primary grid and dashed lines are used for dual cells.

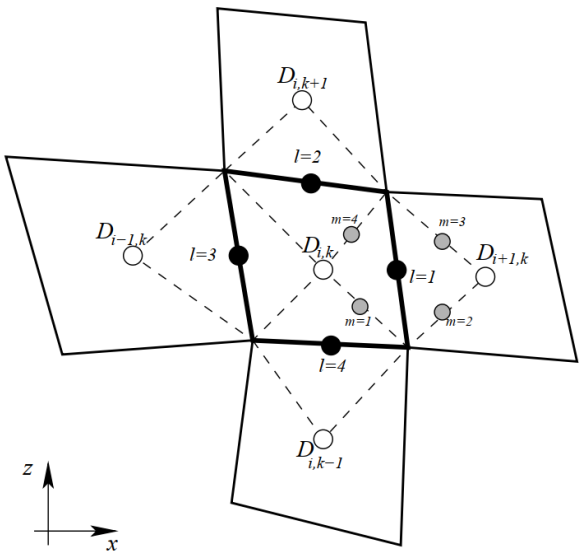

Figure 7: Discretization of the viscous fluxes, retrieved from [3]

4.3.1 MacCormack scheme

The approach of using MacCormack scheme in FVM follows the same as in the Finite Difference Method (see section 4.2). The discretization if performed in two steps: *predictor-corrector*, combining forward with backward discretization. Moreover, in contrast to DIF, the integrals are approximated by sums of the fluxes over the faces (edges) of the control volumes. The values of the fluxes at the faces are computed as average of the values in the centre of the cells adjacent to the face. This evaluation of fluxes, following the MacCormack logic, is again performed in two steps. In general the MacCormack scheme for Finite Volume Method can be formulated as follows:

Predictor:

$$W_{i,j}^{n+\frac{1}{2}} = W_{i,j}^{n} - \frac{\Delta t}{|D_{i,j}|}\left(\sum_{k=1}^{4}\left[(F_k^n - R_k^n)\Delta z_k - (G_k^n - S_k^n)\Delta x_k\right] + f_{i,j}\right) \tag{4.19}$$

Corrector:

$$W_{i,j}^{n+1} = \frac{1}{2}\left(W_{i,j}^{n} + W_{i,j}^{n+\frac{1}{2}} - \frac{\Delta t}{|D_{i,j}|}\left(\sum_{k=1}^{4}\left[(F_k^{n+\frac{1}{2}} - R_k^{n+\frac{1}{2}})\Delta z_k - (G_k^{n+\frac{1}{2}} - S_k^{n+\frac{1}{2}})\Delta x_k\right] + f_{i,j}\right)\right) \tag{4.20}$$

with $f_{i,j}$ being directly evaluated as a cell average of $\boldsymbol{f}$:

$$f_{i,j} = \int_{D_{i,j}} \boldsymbol{f}\, dS \tag{4.21}$$

Now we proceed to discretization of the fluxes. First we address the inviscid terms. Following Figure 8 illustrates the process.

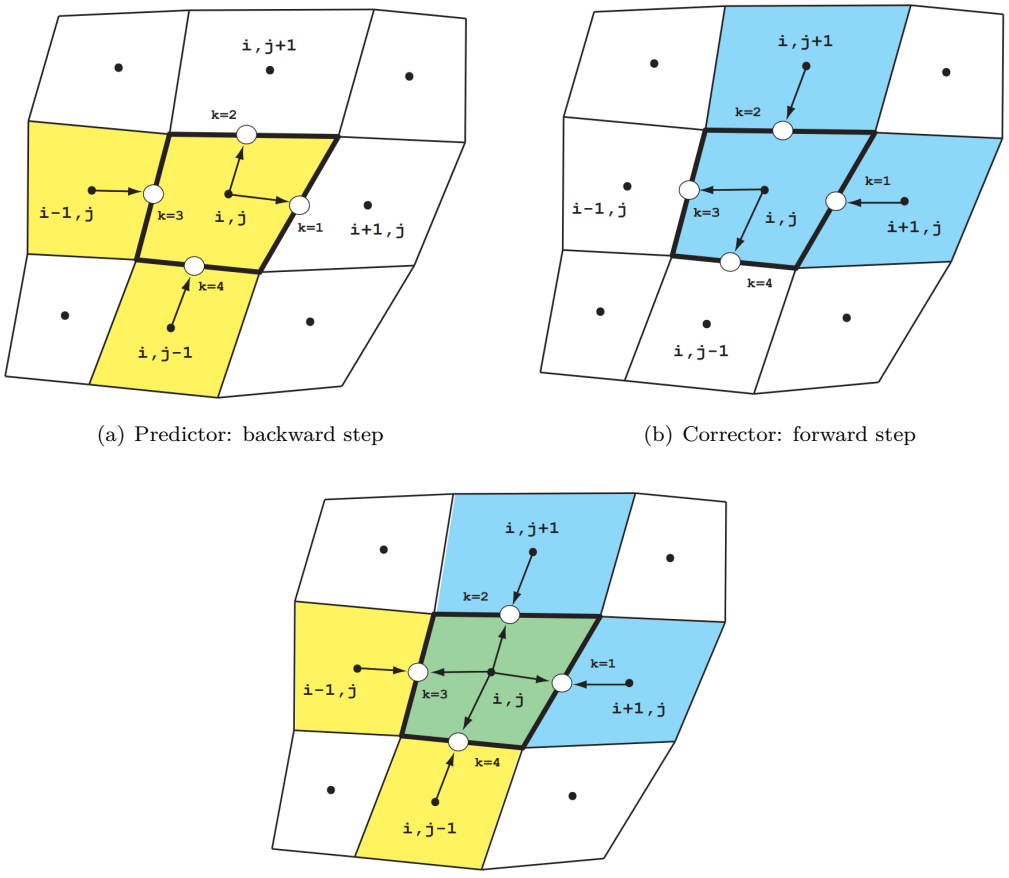

(a) Predictor: backward step

(b) Corrector: forward step

(c) Predictor+Corrector

Figure 8: Discretization using MacCormack scheme, retrieved from [29]

The fluxes discretization using MacCormack scheme goes as follows:

Predictor:

$$F_1 = F_{i,j}, \quad F_2 = F_{i,j}, \quad F_3 = F_{i-1,j}, \quad F_4 = F_{i,j-1} \tag{4.22}$$

$$G_1 = G_{i,j}, \quad G_2 = G_{i,j}, \quad G_3 = G_{i-1,j}, \quad G_4 = G_{i,j-1} \tag{4.23}$$

Corrector:

$$F_1 = F_{i+1,j}, \quad F_2 = F_{i,j+1}, \quad F_3 = F_{i,j}, \quad F_4 = F_{i,j} \tag{4.24}$$

$$G_1 = G_{i+1,j}, \quad G_2 = G_{i,j+1}, \quad G_3 = G_{i,j}, \quad G_4 = G_{i,j} \tag{4.25}$$

In order to discretize viscous fluxes, we need dual volumes to evaluate the velocity gradients, as it is depicted in the Figure 9. After evaluation of the additional derivatives over the dual volumes, the vectors R, S are then discretized similarly to inviscid fluxes in (4.22)-(4.25).

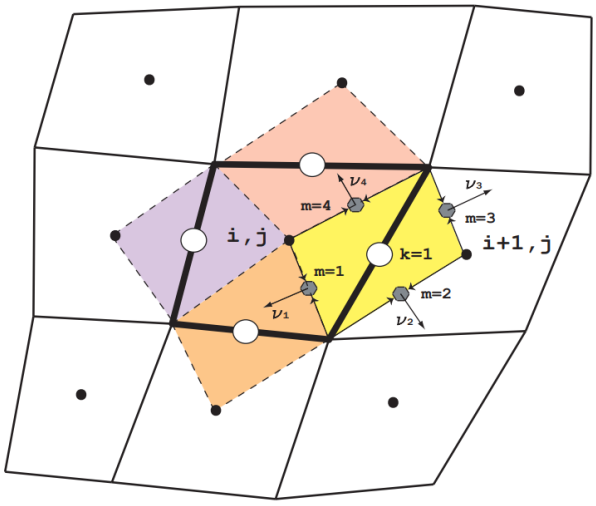

Figure 9: Discretization of the viscous fluxes, retrieved from [29]

The approximation of the gradients in viscous terms begins with replacing of the partial derivative by line integral over the dual cell boundary $\partial\tilde{D}$:

$$u_x \approx \frac{1}{|\tilde{D}|} \oint_{\partial\tilde{D}} u\nu^x dxdy, \tag{4.26}$$

where $\tilde{D}$ is the area of the appropriate dual cell and ν^x represents the outer normal to the dual cell boundaries. That is followed by approximation of the line integral by discrete sum over the dual cell faces:

$$u_x \approx \frac{1}{|\tilde{D}|} \oint_{\partial\tilde{D}} u\nu^x dxdy \approx \frac{1}{|D_m|} \sum_{m=1}^{4} u_m \nu^x l_m, \tag{4.27}$$

where u_m is the value in the centre of m-th dual cell face and l_m is the length of the given face (edge). Computed as average of the value in the centre and corresponding vertex of the primary cell, with the vertex value being evaluated as average of the four surrounding cell-centred values.

4.4 Meshing of the domain

This section deals with meshing of the computational domain and addressing the problem of modelling an obstacle within the domain.

In the preceding thesis, only structured and uniform (orthogonal and equidistant) grid was used. However, when refining the mesh in order to achieve better accuracy, the computational cost gradually increases, due to the reason that the whole domain is refined. This approach may be sufficient for simple problems, such cases will be presented in the Validation chapter, where the mesh can be relatively coarse. As the complexity of the problems increases, the practicality of simple uniform mesh declines rapidly.

In general, results of numerical simulations strongly depend on the mesh used. Therefore, more sophisticated approach is introduced in this work. Structural grid still holds, primarily to maintain the ability to build on the previous work and to easily present comparison of the different approaches. The improvement lies in refining the mesh only locally in the expected areas of large or sudden changes in values of computed quantities. In the studied problems of this work, it is exclusively the area close to the ground, to correctly resolve the boundary layer.

In addition, we will perform the refinement gradually. The main idea of the gradual refinement (and coarsening) is based on refining by reducing the size of the cells to minimum in the area of interest along with coarsening (increasing the size of cells) further in the domain. Since we expect the largest velocity gradients close to the ground and more uniform flow in the top of the domain, this approach suits perfectly for our purposes. In this way, the same number of cells is kept while the accuracy is improved. The grid created using this approach will be referred to as **gradually refined mesh**. The following Figure 10 shows the comparison of uniform and gradually refined mesh (in the vertical direction) with the same number of cells.

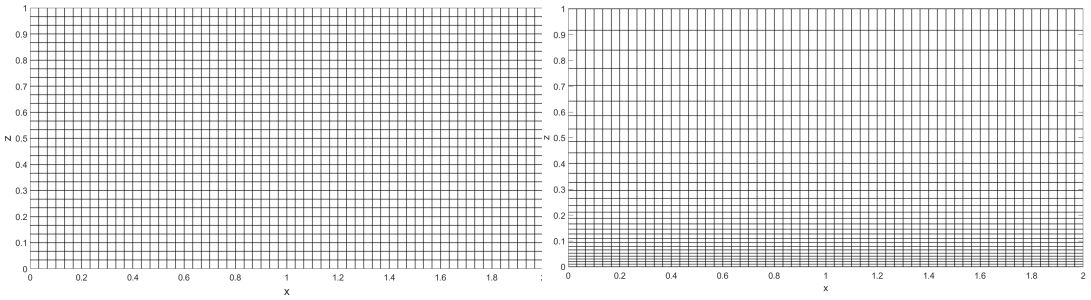

(a) Uniform mesh

(b) Gradually refined mesh

Figure 10: Mesh refinement

However, this approach may be accompanied by several problems. Besides the need to pay attention to the choice of time step, it is necessary to guarantee a smooth change in size of the cells. In case, we increase (decrease) the size unduly or choose too big of time-step not respecting the smallest of cells, the stability of the numerical method will not be maintained. The choice of the time step will be discussed later in the numerical simulations chapter. In case of gradual refinement, we maintain the procedure of increasing (decreasing) the cell sizes by maximum of 3%. Moreover, to sustain the most stability and accuracy close to the ground, we keep the first few cells at the bottom constant in the smallest size before proceeding to smooth increase in size.

4.4.1 Immersed boundary method

Building on the previous work, we first present simple but elegant approach to implement an obstacle inside the computational domain. It is called **Immersed boundary method**, first introduced in [27]. The method is based on meshing the whole domain regardless of the obstacle and then enforcing zero values for all velocity components inside of the computation domain where the obstacle lies. Thus, the boundary is immersed into the domain by zeroing velocity to represent the interaction of fluid with solid boundary.

The main advantage of this method is its simplicity. It does not require any complex intervention to the mesh or code, only enforcing zero velocity at desired location. Application of the method is shown in the Figure 11, where black colour represents the mesh area where the fluid flows freely and red shows the immersed boundary, where velocity is forced to be zero.

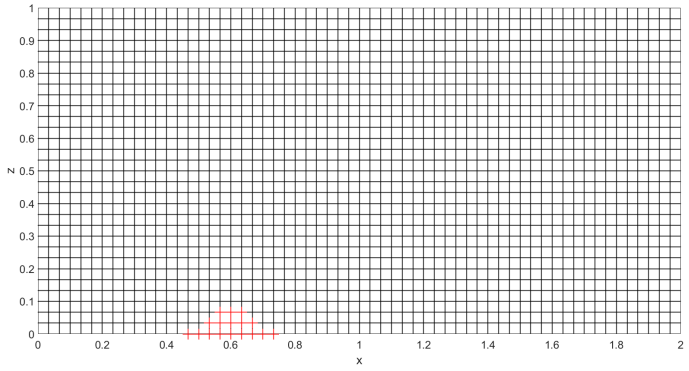

Figure 11: Immersed boundary method

The accuracy of this method is mesh-dependent again. It may result in incorrectly high gradient of velocity in the area around the obstacle, because the transition between solid boundary (obstacle) and the flow is not otherwise resolved and depends only on the appropriate position and number of grid points in that area.

4.4.2 Wall fitted mesh

Other, more realistic approach is so called **Wall fitted mesh**. The meshing is performed only in the area where the fluid flows, thus copies the solid boundary. The mesh is therefore curved along the obstacle by moving the corresponding grid points to desired location. Such meshing is shown in Figure 12.

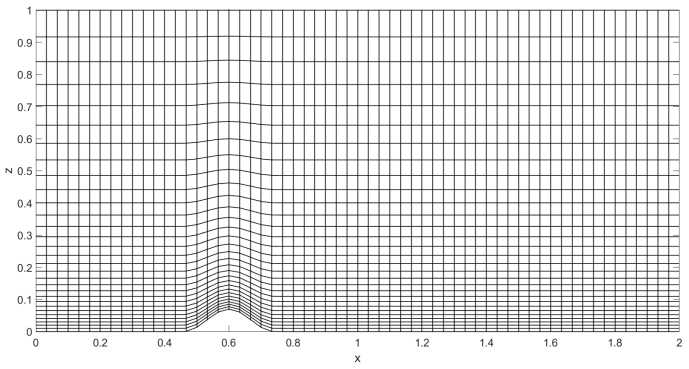

Figure 12: Wall fitted mesh

Wall fitted mesh represents the more intuitive and closer to reality approach of representing the domain. Additionally, higher accuracy can be achieved due to better control over the position of the grid points and imposition of the proper boundary conditions at the edge of the obstacle. On the other side, this approach is more complicated to implement. The mesh has to be additionally curved, grid points above the obstacle gradually shifted and the sizes of the cells and its faced recalculated in order to use the correct values in the equations.

Selecting and constructing the suitable mesh for a given problem may become a very challenging task. Therefore, we will elaborate on it more later in this work. The specific mesh and obstacle

modelling approach will be presented in each case and the study of mesh dependency will be discussed in the chapter of numerical simulations.

4.5 Implementation and monitoring

Implementation of the numerical methods takes place in the programming environment MATLAB. The code consists exclusively of self-developed scripts. This custom solver includes: meshing of the domain, declaring all the necessary variables, computing of the discretized equations and processing basic graphical visualizations of the results. Although MATLAB is suitable for numerical computing, for the purpose of better quality visualization, more powerful tool - Paraview - is additionally used. Therefore, data obtained from conducted simulations in MATLAB are then post-processed in Paraview. These graphical outputs are then presented in this work.

In order to track the convergency of the numerical solutions, i. e. reaching a steady-state solution, we introduce the residues. Residues represent the difference between the values in the current and the previous iteration. We use the information to map the rate of the convergence and to check the achievement of a steady-state solution.

For the purposes of this work, we define residues using the Euclidean norm of the difference of the two consequent iterations related to the size of the computational field. This way of tracking convergence is propagated for example in [20]. Mathematically speaking it can be written as follows:

$$Rez\,(W) = \frac{\|W^{n+1} - W^{n}\|_2}{nx \cdot nz} = \frac{\sqrt{\sum_{i,j} \left(W_{i,j}^{n+1} - W_{i,j}^{n}\right)^2}}{nx \cdot nz} \tag{4.28}$$

In addition, to more thoroughly compare the results of numerical simulations with analytical solution, we introduce another quantity to track the accuracy during simulation. It is a quantity evaluating the norm of the difference between the horizontal velocity of numerical u and analytical u^a solution related to the average in one cell. The determination of is similar to the calculation of residues ()4.28) except the difference of two iterations is substituted with difference of the two solutions, as reads:

$$u_r = \frac{\|\,\mathrm{u}^a - u\|_2}{nx \cdot nz} = \frac{\sqrt{\sum_{i,j} \left(\,\mathrm{u}_{i,j}^a - u_{i,j}\right)^2}}{nx \cdot nz} \tag{4.29}$$

5 Validation

The mathematical model representing and approximating the physical reality was presented in chapter 3. It was followed by numerical methods providing discretization in order to implement the set of equations in code and conduct simulations of the fluid flows. In this section a validation of this code is presented. It contains two classic problems with existing analytical solution. First, we take the well-known and widely used validation case - laminar channel flow in two dimension, to simply test the basic function of the methods. Then we test the solver on a problem of stratified fluid flow on a slope.

5.1 Laminar channel flow

First test case consists of commonly used problem, that can be imagined either as a flow between two plates or a channel flow. In each case, in 2D, the setup is identical. At the top and bottom a solid boundary is considered, following the so called no-slip condition, where the velocity at the wall equals zero and the fluid flows from inlet to outlet due to existing pressure gradient. Figure **??** shows the setup of the case, where the flow in the direction x is caused by the difference between the inlet pressure p_1 and the outlet pressure p_2.

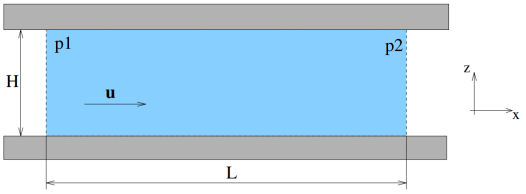

Figure 13: Channel flow setup

The flow is simplified to be steady, laminar and incompressible with constant density ρ. That leads to the system of Navier-Stokes equations in the following (conservative) form:

$$0 = \frac{\partial u}{\partial x} + \frac{\partial w}{\partial z} \tag{5.1}$$

$$\frac{\partial u}{\partial t} = -\frac{\partial (uu)}{\partial x} - \frac{\partial (uw)}{\partial z} - \frac{1}{\rho}\frac{\partial p}{\partial x} + \nu\left(\frac{\partial^2 u}{\partial x^2} + \frac{\partial^2 u}{\partial z^2}\right) \tag{5.2}$$

$$\frac{\partial w}{\partial t} = -\frac{\partial (uw)}{\partial x} - \frac{\partial (ww)}{\partial z} - \frac{1}{\rho}\frac{\partial p}{\partial z} + \nu\left(\frac{\partial^2 w}{\partial x^2} + \frac{\partial^2 w}{\partial z^2}\right), \tag{5.3}$$

This system of equation describes the laminar channel flow fully. Next we approach to solving this system both analytically and numerically.

5.1.1 Analytical solution

Analytical solution of this setup can be obtained with the help of few simple considerations. Nevertheless, it was already derived in the preceding work [36]. Thus, only the result is provided here.

Considering only two-dimensional domain, constant density, steady state and fully developed one-dimensional flow, it simplifies to horizontal velocity equation:

$$u(z) = \frac{p_{out} - p_{in}}{L}\frac{z(z-H)}{2\mu}, \tag{5.4}$$

where the velocity depends on vertical direction z and the pressure gradient caused by the difference of inlet p_{in} outlet pressure p_{out}. From the equation (5.4) it is apparent that the maximum velocity occurs in the middle of the channel, namely:

$$u_{max} = u\left(\frac{H}{2}\right) = \frac{p_{in} - p_{out}}{L}\frac{H^2}{8\mu}. \tag{5.5}$$

The resulting parabolic velocity profile is presented in Figure (14).

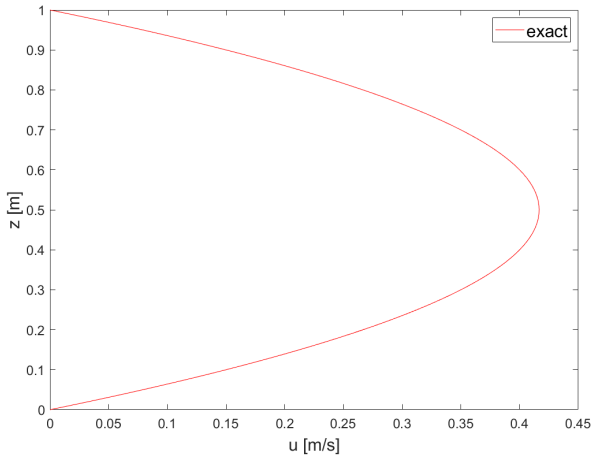

Figure 14: Velocity profile - analytical solution

5.1.2 Numerical solution

The validation was performed for both Finite Difference Method and Finite Volume Method (discretization described in the previous chapter). The solutions by both methods were carried out on the same uniform mesh, using artificial compressibility method and MacCormack scheme. The parameters defining the settings of the case are the subject of the following paragraphs.

Mesh

Computational domain has length L and height H and is covered by mesh of n_x number of points in the x direction and n_z number points in z direction. Thus the equidistant distances between the grid points (size of the cells) are determined by $\Delta x = L/n_x$ and $\Delta z = H/n_z$. The specific numbers used in this case are:

- $L = 3.0$
- $n_x = 30$
- $\Delta x = 0.1$
- $H = 1.0$
- $n_z = 100$
- $\Delta z = 0.01$

We assume a fully developed flow with parabolic velocity profile in z and no significant changes in the x. Thus small number of points n_x in horizontal direction is justified, because only the vertical direction needs to be resolved in detail.

Initial parameters

The test case is designed for laminar flow. The flow regime is controlled by Reynolds number $Re < 2300$. The following parameters meet the condition. The simulation always runs until the prescribed number of iterations n_t.

- $\rho = 1000\, kg \cdot m^{-3}$
- $p_{in} = 10.0\, Pa$
- $n_t = 1.0 \cdot 10^6$
- $\nu = 1.0 \cdot 10^{-3}\, m^2 \cdot s^{-1}$
- $p_{out} = 0.0\, Pa$
- $\beta = 5.0\, m \cdot s^{-1}$
- $\Delta t = 5.0 \cdot 10^{-3}$

The above mentioned parameters are the ones used to obtain the presented results. Simulations testing other setups and mesh refinements were undertaken. These, however, present the best practice for the given situation and code.

Initial conditions were always chosen uniformly for the whole velocity and pressure fields. Specifically in this test case as:

$$u_0 = 0, \quad w_0 = 0, \quad p_0 = p_{in}$$

Boundary conditions

Next, values at the boundaries need to be prescribed. In case of velocity components, the values represent the physical reality at the given domain (e.g the zero velocity at the wall). For pressure the boundary conditions are not in the traditional physical meaning. However, to be able to numerically compute the pressure field from the modified continuity equation (4.1), the boundary conditions for pressure have to be imposed. Nevertheless, in order to be completely transparent about how the numerical simulation was set up, we present the so-called boundary conditions in each case in this work.

Boundary conditions for both methods were set up in following manner. On the inlet (left) boundary are for both velocity components prescribed homogenous Neumann conditions and Dirichlet condition for inlet pressure.

$$\frac{\partial u}{\partial x} = 0, \quad \frac{\partial w}{\partial z} = 0, \quad p = p_{in}$$

Oulet boundary is resolved in similar manner:

$$\frac{\partial u}{\partial x} = 0, \quad \frac{\partial w}{\partial z} = 0, \quad p = p_{out}$$

Top and bottom boundaries have the exact same conditions prescribed. Velocity components follow the no-slip condition and homogenous Neumann condition is used for pressure.

$$u = 0, \quad w = 0, \quad \frac{\partial p}{\partial z} = 0$$

Numerical results

The Figure 15 presents the contours of the velocity. That represents the horizontal velocity fields across the whole computational domain, where the maximum value is reached in the middle of the channel. On the left hand side is the result of DIF solution and the sub-figure on the right belongs to FVM.

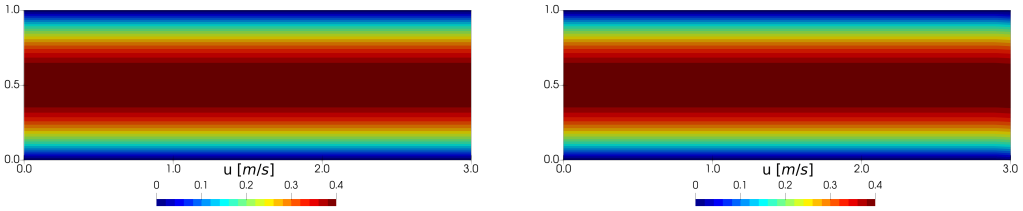

(a) Finite Diference Method (b) Finite Volume Method

Figure 15: Canal - horizontal velocity fields

The next Figure 16 shows the comparison of velocity profiles in the middle of the channel obtained from analytical solution (red line) and numerical simulation (blue markers).

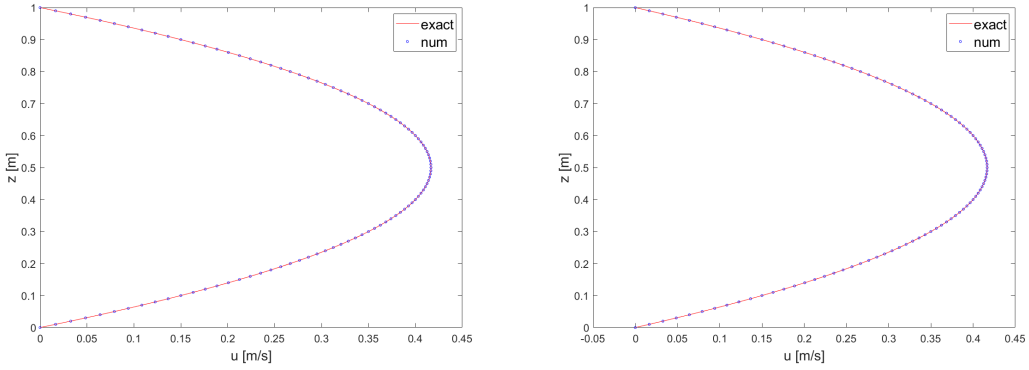

(a) Finite Diference Method (b) Finite Volume Method

Figure 16: Canal - horizontal velocity profiles

It is obvious that from both methods we have obtained accurate results matching the analytical solution. Therefore, validation of the code on this simple test case was successful.

The convergence can be reviewed in the Figure 17. Residues are shown for both methods and all computed quantities: u, w, p. Both solutions reached a steady state solution, where both solutions did not change significantly after $4 \cdot 10^5$ iterations. However, in case of DIF, the residues are still chaotically changing for another three hundred thousand iterations, after which the values stabilize and become constant. FVM converges surely after $4 \cdot 10^5$ iterations with residues slightly oscillating the whole time of the simulation. Nevertheless, we let both of the solutions run significantly longer, up to 1 million iterations, to ensure that no further changes occur.

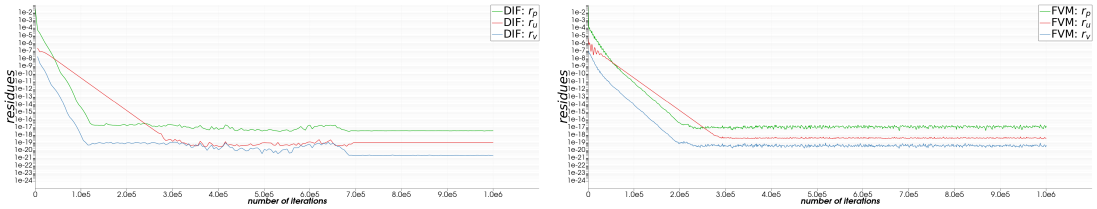

(a) Finite Diference Method

(b) Finite Volume Method

Figure 17: Channel flow - residues

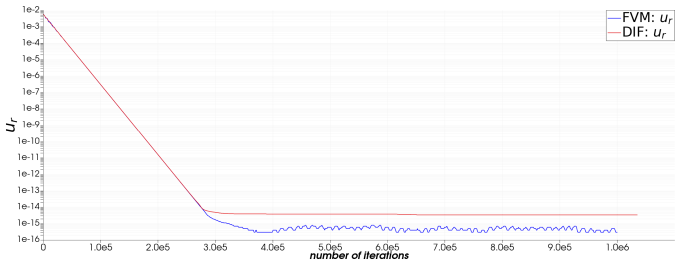

Figure 18: Horizontal velocity difference

To further compare the methods in terms of accuracy, we present the Figure 18 that maps the norm of the difference u_r between the numerical solutions and analytical solution during the simulation. Both solutions have very similar course with steep decline in the first three hundred thousand iterations. After that DIF reaches constant value for the rest of the simulation. FVM achieves lower values by approximately one degree of magnitude, but it is accompanied by a steady slight oscillations of the values.

Therefore, FVM provides higher accuracy, but needs to be carefully implemented in other cases to avoid the increase in oscillations of values. Nevertheless, both methods have provided convincing accuracy.

5.2 Stratified fluid flow on a slope

Second test case consists of more complex problem, flow of a stratified fluid on a slope. More specifically, we consider a stable stratification with density decreasing with distance from the wall in the direction opposite to the act gravity.

The computational domain is simplified to two-dimensional region on an infinite inclined flat plate. For an easier description of the case, the physical coordinates of horizontal and vertical directions are transformed by the plate tilt angle α. The coordinate x is thus parallel with the plate and the expected flow direction and z is perpendicular to the plate and indicates the distance from the wall. The setup is shown in the Figure 19, where the blue region highlights the computational domain, that is filled by stratified fluid.

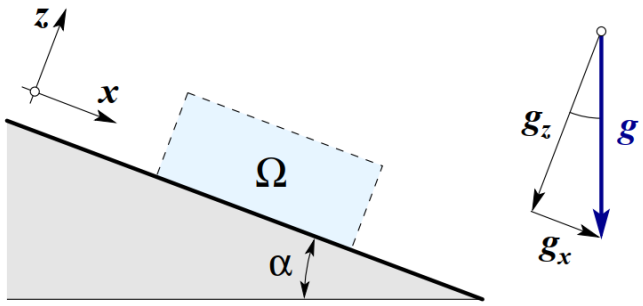

Figure 19: Stratified fluid flow on a slope setup, adapted from [3]

Due to the transformed coordinates x, z, the gravity acceleration from the original system $\boldsymbol{g} = (0, -g)$ is also transformed to $\boldsymbol{g} = (g_x, g_z) = (g \sin\alpha, -g\cos\alpha)$. The stratification is assumed to be constant and stable. Density is thus changing only linearly in the opposite direction to gravity acceleration $\boldsymbol{g}$ from the highest to the lowest. Therefore, the density gradient $\boldsymbol{\gamma}$ must also be expressed in the new coordinate system as $\boldsymbol{\gamma} = (\gamma \sin\alpha, -\gamma\cos\alpha)$. The background density of the fluid can be thus described as follows:

$$\rho_0 = \rho^* + \gamma x \sin\alpha - z\gamma\cos\alpha. \tag{5.6}$$

where ρ^* is the density at the origin of the coordinates.

The case is again assumed to be steady, laminar and incompressible. The flow is induced by setting density perturbation ρ'_w on he wall. The expected results are the velocity u and density perturbation ρ' profiles changing only with the distance from the wall. Navier-Stokes equations describing this fluid problem can be written in the (conservative) form as follows:

$$0 = \frac{\partial u}{\partial x} + \frac{\partial w}{\partial z} \tag{5.7}$$

$$\frac{\partial \rho'}{\partial t} = -\frac{\partial(\rho' u)}{\partial x} - \frac{\partial(\rho' w)}{\partial z} + \kappa\left(\frac{\partial^2 \rho'}{\partial x^2} + \frac{\partial^2 \rho'}{\partial z^2}\right) - u\gamma\sin\alpha + w\gamma\cos\alpha \tag{5.8}$$

$$\frac{\partial u}{\partial t} = -\frac{\partial(uu)}{\partial x} - \frac{\partial(uw)}{\partial z} - \frac{1}{\rho*}\frac{\partial p}{\partial x} + \nu\left(\frac{\partial^2 u}{\partial x^2} + \frac{\partial^2 u}{\partial z^2}\right) + \frac{\rho'}{\rho*} g\sin\alpha \tag{5.9}$$

$$\frac{\partial w}{\partial t} = -\frac{\partial(uw)}{\partial x} - \frac{\partial(ww)}{\partial z} - \frac{1}{\rho*}\frac{\partial p}{\partial z} + \nu\left(\frac{\partial^2 w}{\partial x^2} + \frac{\partial^2 w}{\partial z^2}\right) - \frac{\rho'}{\rho*} g\cos\alpha, \tag{5.10}$$

Again, analytical solution is available for this setup. In the following sections, we will show the analytical and numerical solutions for the system above.

5.2.1 Analytical solution

Analytical solution of this problem was also already derived in the preceding work [36]. After including consideration of time-steady, fully-developed flow and linearly stratified fluid and using

basic differential and integral calculus, we can, from the set of equations (5.7)-(5.10), arrive at equations for velocity and density perturbation as follows:

$$\rho'(z) = \rho'_w \exp\left(-\frac{z}{l}\right)\cos\left(\frac{z}{l}\right) \tag{5.11}$$

$$u(z) = \rho'_w \sqrt{\frac{g\kappa}{\gamma\mu}} \exp\left(-\frac{z}{l}\right)\cos\left(\frac{z}{l}\right) \tag{5.12}$$

where ρ'_w is the density perturbation at the wall and the length l is determined by:

$$l = \sqrt[4]{\frac{4\mu\kappa}{g\gamma\sin^2\alpha}} \tag{5.13}$$

Dependencies of the quantities on the distance from the wall, obtained analytically, are shown in the Figure 20 on the logarithmic scale.

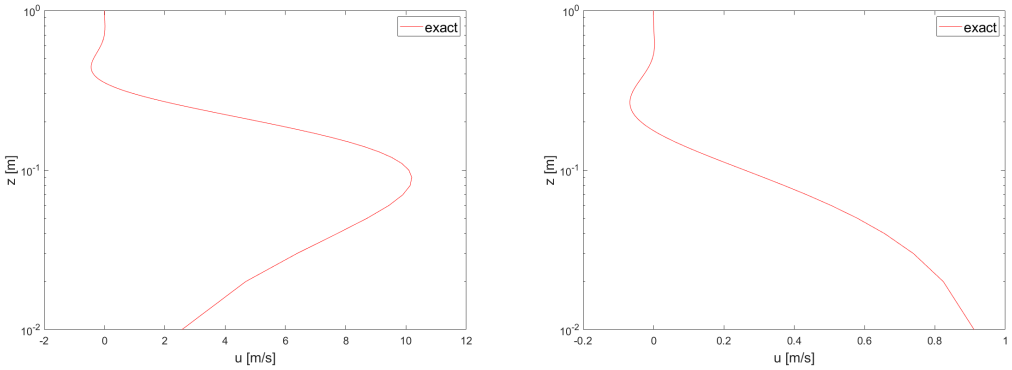

(a) Velocity u profile

(b) Density perturbation ρ' profile

Figure 20: Analytical solution - velocity and density perturbation profiles

5.2.2 Numerical solution

As in the previous case, validation was performed for both Finite Difference Method and Finite Volume Method. Again, both solutions were carried out on the same uniform mesh with artificial compressibility method and MacCormack scheme. We also keep the same notation for the following parameters, that represent the best practice for the given case and solver.

Mesh

- $L = 3.0$
- $n_x = 100$
- $\Delta x = 0.03$
- $H = 1.0$
- $n_z = 100$
- $\Delta z = 0.01$

In this case, due to the increase of complexity, the number of cells also increased in comparison to the previous problem.

Initial parameters

Initial parameters were chosen to maintain laminar flow. Moreover, it is necessary to prescribe additional parameters for the stratified fluid, which were explained in the previous sections.

- $\rho'_w = 1\ kg \cdot m^{-3}$
- $\beta = 15.0\ m \cdot s^{-1}$
- $\alpha = 30$
- $\nu = 1.0 \cdot 10^{-3}\ m^2 \cdot s^{-1}$
- $g = 10.0\ m \cdot s^{-2}$
- $\Delta t = 5.0 \cdot 10^{-4}$
- $\kappa = 1.0 \cdot 10^{-3}\ m^2 \cdot s^{-1}$
- $\gamma = 1.0 \cdot 10^{-2}\ kg \cdot m^{-4}$
- $n_t = 5.0 \cdot 10^6$

Initial conditions, inducing the flow, are represented by setting the density perturbation at the wall $\rho'_w = 1\ kg \cdot m^{-3}$. All the other values: velocity components u_0, w_0, pressure p_0 and the rest of the density perturbation field ρ'_0 are set to zero.

Boundary conditions

On the wall (inclined plate) the velocity components follow the no-slip condition, density perturbation keeps the the value ρ'_w and pressure at the solid boundary is determined by quadratic extrapolation. That can be summarized as:

$$u = 0, \quad w = 0, \quad p_{i,j} = 3 \cdot p_{i,j+1} - 3 \cdot p_{i,j+2} + p_{i,j+3}, \quad \rho' = \rho'_w$$

The top is considered as an open boundary, thus the conditions are prescribed as follows:

$$\frac{\partial u}{\partial z} = 0, \quad \frac{\partial w}{\partial z} = 0, \quad p = 0, \quad \frac{\partial \rho'}{\partial z} = 0.$$

The computational domain is considered as a part of a larger region consisting of steady developed flow in one direction parallel to the ground. Therefore, only homogenous Neumann conditions are imposed on the inlet and outlet:

$$\frac{\partial u}{\partial x} = 0, \quad \frac{\partial v}{\partial x} = 0, \quad \frac{\partial p}{\partial x} = 0, \quad \frac{\partial \rho'}{\partial x} = 0.$$

Numerical results

Results obtained from both methods (DIF, FVM) are shown in the following figures. Again, we follow the order of DIF being on the left hand side and FVM on the right hand side.

First the profiles of fully developed horizontal velocity (parallel to the ground) and density perturbation are shown in Figure 21 and Figure 22 respectively. The profiles are depicted depending on the distance from the wall (z coordinate in this setup) on a logarithmic scale in comparison with the analytical solution. Blue markers represent the values obtained from numerical solutions and red line the analytical result.

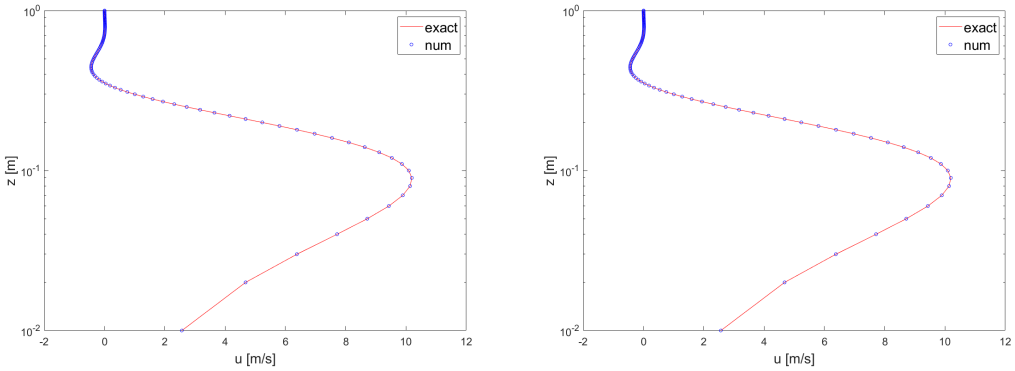

(a) Finite Diference Method (b) Finite Volume Method

Figure 21: Stratified flow on a slope - horizontal velocity profiles

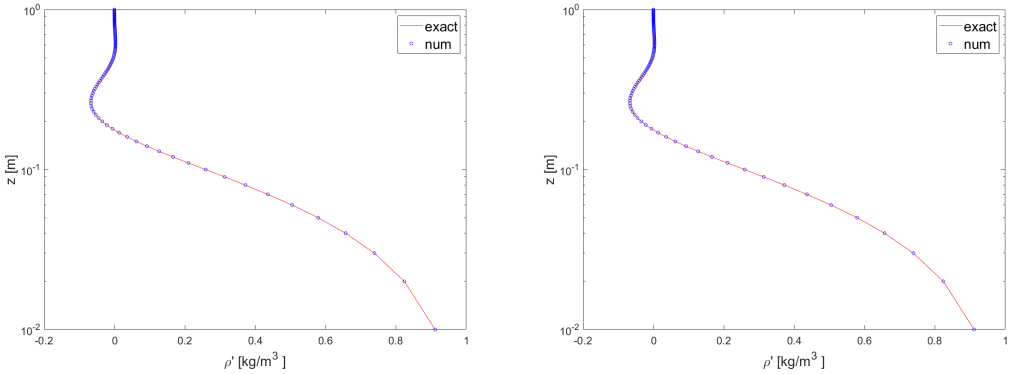

(a) Finite Diference Method (b) Finite Volume Method

Figure 22: Stratified flow on a slope: density perturbation profiles

It is worth noting that the logarithmic scale does not show the exact value on the wall where $z = 0$. However, both solutions asymptotically reach to the value prescribed on the wall by boundary conditions. In this form the results are presented mainly to illustrate the dependency on the z as clearly as possible.

Additionally, the following Figures 23 and 24 show the contours of u and ρ', obtained by both methods, to display the values across the computational domain. One can see that the values of both quantities are constant along the x coordinate in the whole domain. That means, fully-developed steady flow is indeed achieved.

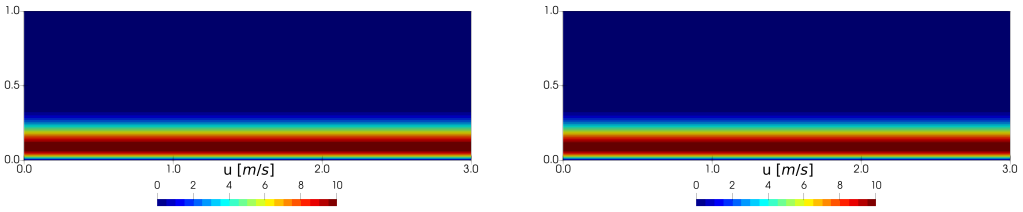

(a) Finite Diference Method (b) Finite Volume Method

Figure 23: Stratified flow on a slope - horizontal velocity fields

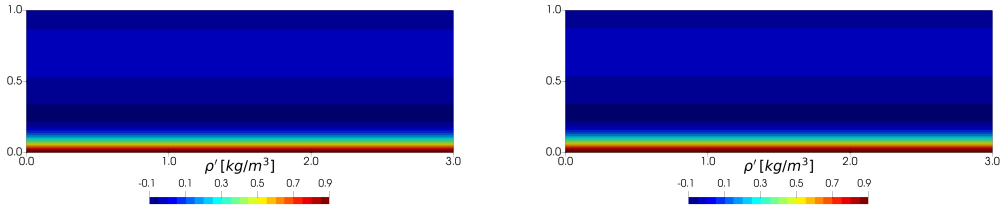

(a) Finite Diference Method (b) Finite Volume Method

Figure 24: Stratified flow on a slope - density perturbation fields

The residues do not provide any distinction between the methods. For that reason, we excluded them from this section to avoid redundancy. Both solutions however, reached a developed steady-state flow and are consistent with the analytical solution, as demonstrated above. To compare the course of the simulations, the Figure 25 shows the norm of the difference of velocity between numerical and analytical solutions depending on the number of iterations. FVM takes longer to obtain a constant value. During the course of the simulation the FVM solution oscillates more around the exact seeking value, but eventually arrives closer to the exact analytical solution. Nevertheless, the final value of the difference is lower than in DIF. Therefore we may state, that the solution from FVM is again slightly more accurate.

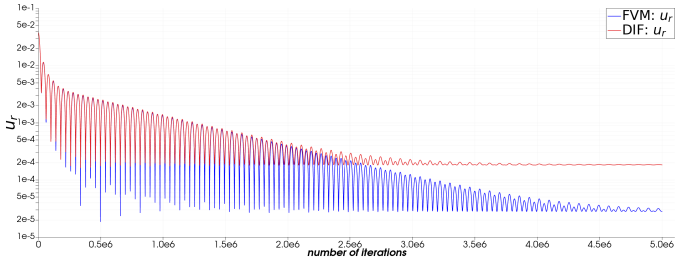

Figure 25: Horizontal velocity difference

We have presented the results of flow of stratified fluid on the slope. Results obtained from our simulations using both methods convincingly correspond with the analytical solution, as it was demonstrated on the velocity and density perturbation profiles. However, FVM provided more accurate results in terms of smaller difference between horizontal velocity. On the other hand, DIF possesses the advantage of less computational effort. Nevertheless, we can state that the solver, with 2 different methods included, was validated even for the case of stratified fluid flow.

6 Numerical experiments

In this chapter, numerical experiments conducted by custom validated code are presented. The dealt problems are no longer possible to be simply solved analytically. The aim is to provide results closer to real atmospheric flows while sustaining relative simplicity in numerical simulations. Therefore, in all following cases we consider flows in the atmospheric boundary layer and introduce obstacles in the computational domain, that represent hills in the real nature.

First, we introduce a case where only laminar flow is considered and a very simple form of an obstacle. Next, turbulence model, described in Chapter 3, is incorporated. Afterwards the main objective will be presented - atmospheric turbulent flow over various hills, where the simulations will be compared with wind tunnel experiments performed by other authors.

In connection with this case, thorough discussion of mesh-dependency, boundary conditions, accuracy and applicability of the methods will be provided. Furthermore, the studied case will be extended to stratified fluid flow.

Results will be again presented from both numerical methods used. The main emphasis is on the Finite Volume Method with the use of wall fitted mesh. However, to expand the discussion and to highlight differences and shortcomings, the Finite Different Method with immersed boundary method to model obstacles is also included.

All the following cases have similar general setups. The computational domain is considered to reflect part of a flow region close to the ground and represents the atmospheric flow in reduced scale, similar to wind tunnel experiments. In addition, all systems are again simplified to two dimension, mainly to reduce computational effort. The initialization, obstacle shape and the flow regime and other parameters differ in each case.

Generally, all the cases can be described by the same set of Navier-Stokes equations, namely (3.38), (3.39) and (3.40), which includes all possible aspects of the mathematical model presented in Chapter 3. In each case, the individual simplifications and parameters will be mentioned. The main differences between the cases lie in the geometry of the hill and whether or not we consider the fluid to be densely stratified. From now on, however, we will refer only to this complete system of governing equations in all cases.

6.1 Laminar flow of stratified fluid over a hill

6.1.1 Setup

This particular case serves as an introduction to atmospheric flow over a hill. It includes a very simple geometry, the hill is represented as part of a circle of radius $r = 0.2\,m$. Height of the hill h is determined as a proportion of the height of the computational domain $\mathrm{h} = \frac{\mathrm{H}}{10}$. The location of the hill is also also proportionally determined as $x_h = 9\,\mathrm{h} = \frac{9}{10}\mathrm{H}$. The setup is depicted in the Figure 26 even with boundary conditions.

To add simplicity, the flow regime is also maintained laminar. Therefore, turbulence properties ν_T and κ_T included in equations (3.39) and (3.40) are set to zero in this case. Nevertheless, the fluid is considered to be stably stratified.

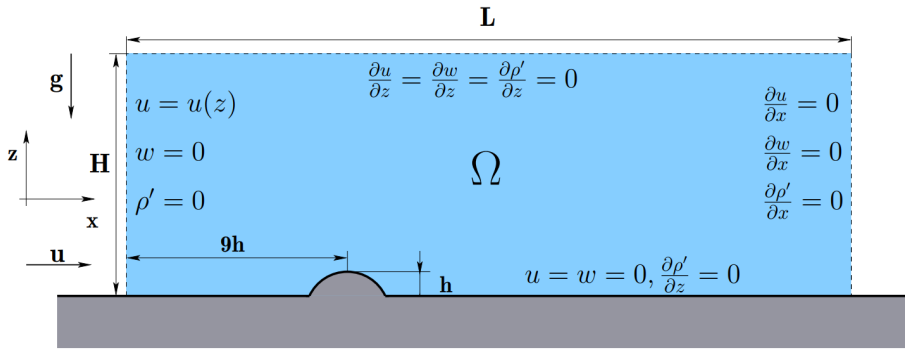

Figure 26: Laminar flow over a hill setup

In case of DIF, the hill is modelled with the Immersed boundary method, whereas in FVM the wall fitted mesh approach is used. The mesh is uniform in both cases except for the wall-fitted mesh above the hill, where the points are shifted upwards and the grid gradually smoothed up to the top of the domain. Nevertheless, for both methods the same number of grid points on the same computational domain is used, namely:

Mesh

- $L = 3.0$
- $H = 1.0$
- $n_x = 100$
- $n_z = 100$
- $\Delta x = 0.03$
- $\Delta z = 0.01$

Due to the increase of complexity, the number of cells also increased.

Initial parameters

The parameters were chosen in connection with a number of related laboratory experiments, for example [24] and [28], that study densely stratified water-based liquid in a tank. In addition, to maintain laminar flow the following input values are used:

- $\rho^* = 1000\,kg \cdot m^{-3}$
- $\nu = 1.0 \cdot 10^{-3}\,m^2 \cdot s^{-1}$
- $\kappa = 1.0 \cdot 10^{-3}\,m^2 \cdot s^{-1}$
- $\beta = 5.0\,m \cdot s^{-1}$
- $g = 10.0\,m \cdot s^{-2}$
- $\gamma = 100\,kg \cdot m^{-4}$
- $u = u(z)\,m \cdot s^{-1}$
- $u_{max} = 0.25\,m \cdot s^{-1}$
- $\Delta t = 1.0 \cdot 10^{-3}$
- $n_t = 1.0 \cdot 10^6$

The flow is initialized by inlet velocity profile. Horizontal velocity component is set as a function of vertical coordinate z (distance from the ground) assuming parabolic shape up to the half of the domain and fully developed flow above, namely:

$$u(z) = \frac{4u_{max}}{H^2} \cdot z(H - z) \qquad \text{for } z \in \left\langle 0, \frac{H}{2} \right)$$

$$u(z) = u_{max} \qquad \text{for } z \in \left\langle \frac{H}{2}, H \right\rangle$$

Other quantities are set to zero, therefore the initial conditions can be summarized as follows:

$$u_0 = u(z), \quad w_0 = 0, \quad p_0 = 0, \quad \rho'_0 = 0.$$

The background density changes again only linearly depending on the type of stratification, that is according to density gradient γ

$$\rho_0 = \rho^* - \gamma z, \tag{6.1}$$

where ρ^* is the density at the ground.

Boundary conditions

As previously demonstrated, on the wall the velocity components follow the no-slip condition. Pressure and density perturbation are on the boundary prescribed by Neumann homogenous conditions:

$$u = 0, \quad v = 0, \quad \frac{\partial p}{\partial y} = 0, \quad \frac{\partial \rho'}{\partial y} = 0.$$

The top is considered as free stream boundary, therefore Neumann homogenous conditions is applied to all computed quantities:

$$\frac{\partial u}{\partial z} = 0, \quad \frac{\partial w}{\partial z} = 0, \quad \frac{\partial p}{\partial z} = 0, \quad \frac{\partial \rho'}{\partial z} = 0.$$

On the inlet boundary the velocity profile is kept for horizontal velocity component and other conditions are set as follows:

$$u = u(z), \quad w = 0, \quad \frac{\partial p}{\partial x} = 0, \quad \rho' = 0.$$

Pressure is held at a fixed value on the outlet along with Neumann homogenous conditions for the other quantities:

$$\frac{\partial u}{\partial x} = 0, \quad \frac{\partial w}{\partial x} = 0, \quad p = 0, \quad \frac{\partial \rho'}{\partial x} = 0$$

6.1.2 Numerical results

As previously mentioned, this case serves as an introduction to the problem of flow over hill. Therefore, only a brief summarization of the results is presented. Figure 27 shows a comparison of Finite Difference and Finite Volume methods, where horizontal velocity components are depicted as contours in the whole domain. Same as before, DIF is on the left and FVM on the right.

In the immersed boundary method (used only in DIF), the hill is not physically created in the domain, only the velocity components are enforced to be zero. For that reason, the hill is only marked by white line in Figure 27a and the hill is in blue colour representing zero velocity. In FVM on the other hand, the hill is not part of the computed field, due to the use of wall-fitted mesh.

Nevertheless, the resulting velocity fields results very similar regardless of the method used. For a closer look, the comparison of vertical velocity components is provided in Figure 28. We can again see many similarities in the results from both methods.

In general, a visible vertical movement is present due to the interaction of the flow with the obstacle. That is an expected outcome. The flow is deflected upwards by the hill presence and then it again tends to fill the bottom part of the domain. However, the flow does not return to its original form, but the effect of the obstacle persists through the whole domain and we can observe waves in the flow behind the hill.

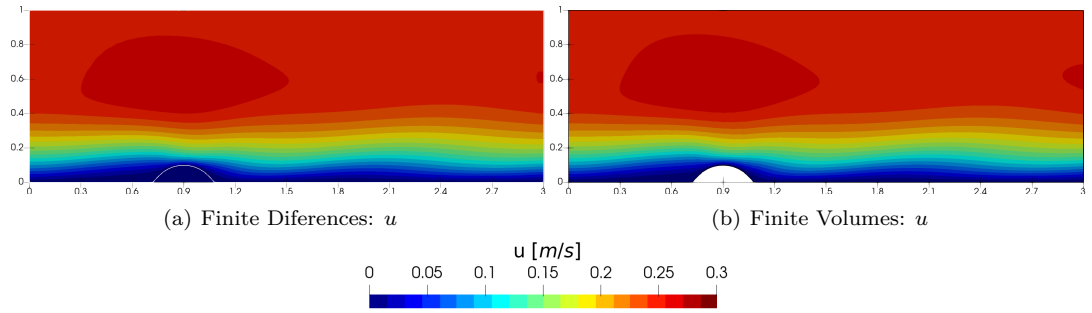

(a) Finite Diferences: u (b) Finite Volumes: u

Figure 27: Laminar flow over hill - horizontal velocity component

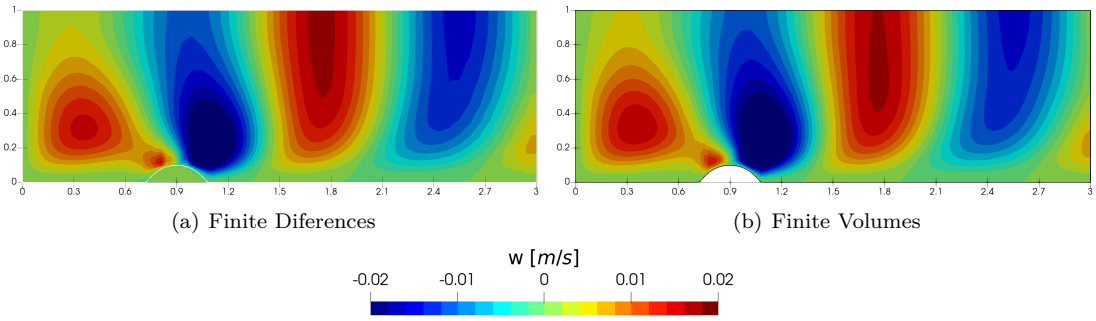

(a) Finite Diferences (b) Finite Volumes

Figure 28: Laminar flow over hill - vertical velocity component

The effect is further enhanced by the stratification of the fluid. That causes the wave patterns of vertical velocity component values in the whole domain. The flow without stratification would result in visible changes only in close vicinity of the hill, as it was demonstrated on similar case in [36]. In addition, the flow velocity would return to its original profile more easily. Therefore, this case provides first indication, that stratification should not be overlook, although this is rather an extreme case.

Due to the strong correlations between the methods using very different approaches, we assume the results to be accurate for this setup. In addition, both approaches of hill modelling are acceptable. We will now proceed to the cases involving turbulent flow.

6.2 Turbulent flow over sinusoidal hills

In this section, simulations of turbulent flows over hills are presented. The mixing length model is implemented to calculate the turbulence properties in each iteration using the equations (3.43) and (3.45).

Stratification is controlled via the Richardson number Ri defined by the relation (2.4). Along with other initial parameters, Ri is chosen as an input value and the density gradient γ is then determined according to this relation. Richardson number $Ri > 0$ defines stable stratification with γ consequently also positive. $Ri = 0$ implies $\gamma = 0$ and neutral (no) stratification and lastly $Ri < 0$ results in negative density gradient γ and unstable stratification.

6.2.1 Setup

In addition, we introduce more precise representation of a hill. Instead of a circle shape, sinusoidal profile is implemented. It represents smooth transition between the horizontal ground and the obstacle. Sinusoidal shape is commonly used in many numerical and experimental studies. The profile is given by the following expression:

$$z_s(x) = \frac{h}{2}\left[1 + \cos\left(\frac{\pi x}{2L_1}\right)\right] \tag{6.2}$$

The height of the sinusoidal hill z_s with respect to the ground is depending on the horizontal direction x, where h is the maximum height of the hill, L_1 is the half-length of the hill.

For the purpose of comparison of our simulations and wind tunnel experiments, we chose the study [19], where the flows over sinusoidal hills are measured. In addition, the mentioned study also involved numerical simulations, where the authors used more complicated approaches to resolve turbulences: the $\kappa - \epsilon$ model and low-Re-number model. Thus the goal is to reproduce the case setup and conduct simulations with the validated custom code using simple mixing length turbulence model to compare and discuss the results. The schematic setup of the studied problem with the hill properties is presented in the Figure 29.

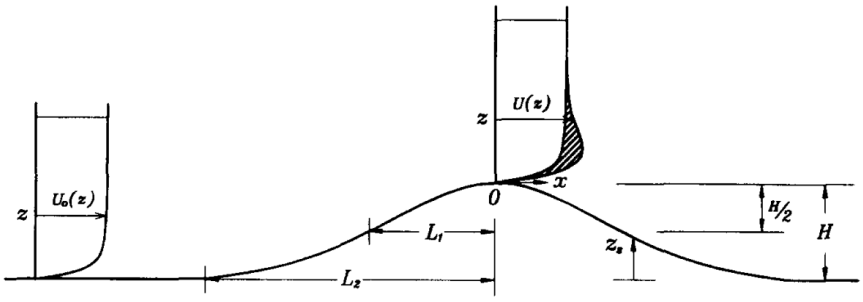

Figure 29: Sinusoidal hill setup, reprinted from [19]

The experiment of [19] was conducted in an open circuit boundary layer wind tunnel with a test section of width, height and length of $1.2\,m$, $1.2\,m$ and $6\,m$. The flow was induced by inlet velocity creating well-developed boundary layer of $z_d = 0.25m$ depth, developed wind speed above the boundary layer $u_{max} = 7\,m \cdot s^{-1}$ and logarithmic velocity profile fitting the function:

$$u_0(z) = \frac{u_*}{\varkappa} \ln \frac{z}{z_0}, \tag{6.3}$$

where $u_* = 0.33\,m \cdot s^{-1}$ is friction velocity, $\varkappa = 0.41$ von Kármán's constant, $z_0 = 0.05\,mm$ roughness parameter and z distance from the ground. It is worth noting that von Kármán's constant is usually mentioned in literature under κ, however we already used it for diffusion coefficient. Therefore, for the purposes of this work, we allow ourselves to denote it by $\varkappa$. The velocity profile $u_0(z)$ can be also seen in the Figure 29 along with the projected profile above the hill.

In our simulations we use the exact same hill shapes and inlet velocity profile as in the aforementioned study [19]. The whole computational domain is represented in the following Figure 30.

In our simulations, the centre of the hill is located at 30% of the length of the whole computational domain $x_h = 0.3L$. Since are imposing the already developed velocity profile right on the inlet, only smaller part of the domain is required upstream of the windward side. Thus we can leave the major region of the domain behind the hill in order to better map the flow on the lee side and further downwind.

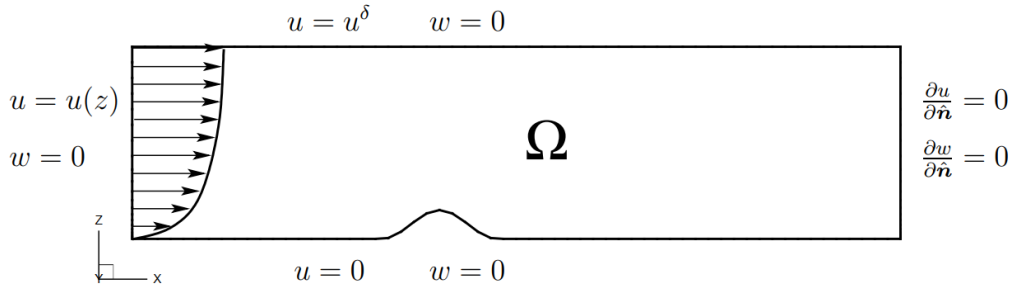

Figure 30: Flow over sinusoidal hill setup

The hills investigated in this case consist of 4 different types differing in the maximum height h and the length L_1, or in other words the slope of the hill $s = \frac{(h/2)}{L_1}$. An additional complication in the small scale wind tunnel testing is resolving the small scale turbulences. Particularly, the calculation of the mixing length ℓ strongly depending on the choice of the asymptotic value ℓ_∞, as (3.42) shows. Consequently, the parameter has strong influence on the numerical results. Therefore, it must be chosen adequately. For our simulations we used values suitable for this setup, based on [3], where one can also find thorough explanation behind the choice. The following Table 1 summarizes the hills parameters along with the corresponding ℓ_∞.

Hill	slope s	height h	length L_1	ℓ_∞
S3H4	0.3	$4\,cm$	$6.67\,cm$	$7.943\,mm$
S5H4	0.5	$4\,cm$	$4.0\,cm$	$11.44\,mm$
S3H7	0.3	$7\,cm$	$11.76\,cm$	$5.756\,mm$
S5H7	0.5	$7\,cm$	$7.0\,cm$	$8.19\,mm$

Table 1: Hill parameters

Mesh

The computational domain, simplified to 2D, remains the same for every hill shape and for both numerical methods. The meshing of the domain differs from the previous cases. Wall-fitted mesh with gradual refinement in the vertical direction is implemented. This meshing approach is exactly illustrated in the Figure 12. Additionally, to correctly resolve the area closest to the ground, several first points near the ground are kept equidistant at the minimum distance z_{min} and then gradually increased by 3% up to the top of the domain.

Horizontal refinement was also tested, but did not provide any significant improvement or change in the results. Mesh-dependency of this setup was thoroughly tested and will be shown later in this chapter. For the purpose of simulate the wind tunnel experiment and achieve matching results following wall-fitted mesh parameters were used:

- $L = 2.0\,m$
- $H = 0.5\,m$
- $n_x = 200$
- $n_z = 100$
- $\Delta x_{uni} = 1 \cdot 10^{-2}\,m$
- $\Delta z_{min} = 1 \cdot 10^{-3}\,m$

Initial parameters

The turbulent flow of this case is characterized by the Reynolds number, which is in the experiment based on the depth of the boundary layer:

$$Re_\delta = \frac{\delta \cdot u_{max}}{\nu} = 1.17 \cdot 10^5.$$

Therefore, the summarization of our corresponding initial parameters reproducing the case reads:

- $\rho^* = 1.225\, kg \cdot m^{-3}$
- $\tilde{\nu} = 1.5 \cdot 10^{-5}\, m^2 \cdot s^{-1}$
- $\tilde{\kappa} = 1.5 \cdot 10^{-5}\, m^2 \cdot s^{-1}$
- $\beta = 2.0\, m \cdot s^{-1}$
- $g = 10.0\, m \cdot s^{-2}$
- $u = u(z)\, m \cdot s^{-1}$
- $u_{max} = 7\, m \cdot s^{-1}$
- $u_* = 0.33\, m \cdot s^{-1}$
- $\varkappa = 0.41$
- $z_0 = 5 \cdot 10^{-5}\, m$
- $z_d = 0.25\, m$
- $Pr_{_T} = 0.74$
- $\Delta t = 2.0 \cdot 10^{-5}$
- $n_t = 5.0 \cdot 10^6$

where the parameters with tilde, namely $\tilde{\nu}$ and $\tilde{\kappa}$ denote only the constant (laminar) part of the quantities. Turbulent components are determined based on the mixing length turbulence model.

The experiment in [19] was designed to reflect the atmospheric boundary layer, however considering only neutrally stratified fluid. Therefore, the density is constant $\rho = \rho^*$ in the whole computational domain and density perturbation ρ' is then not computed.

The flow is initialized by setting horizontal velocity profile, that follows the function (6.3). In order to run a stable simulation, the velocity profile is initially set in the whole domain, as it is expected that the final solution will not differ dramatically in the vast majority of the domain. Other quantities are again set to zero. Initial conditions can thus be written as summarized as follows:

$$u_{_0} = u(z), \quad w_{_0} = 0, \quad p_{_0} = 0$$

Boundary conditions

Boundary conditions are again based on the study [19]. The experiment was performed in a wind tunnel, where the top boundary is solid wall. However, in order to reflect reality more closely, the actual measurement of velocity is performed only up to certain height, where the velocity is fully developed and maintains constant value u_{max} along the measured domain. Therefore, also in their numerical simulations, the velocity values are prescribed using Dirichlet conditions at the top boundary. We follow the setup in order to match the results with our own simulations. However, the approach in modelling real atmospheric flows would be different. Boundary conditions and the influence of their choice will be discussed later in this work. The settings for the purposes of comparison with experimental data is the following.

On the wall, no-slip condition is imposed for the velocity components and homogenous Neumann condition for pressure:

$$u = 0, \quad v = 0, \quad \frac{\partial p}{\partial y} = 0$$

As mentioned, the top is considered as solid boundary, specific values used are:

$$u = u_{max}, \quad w = 0, \quad \frac{\partial p}{\partial z} = 0.$$

On the inlet boundary the velocity profile is kept for horizontal velocity component and other conditions are set as follows:

$$u = u(z), \quad w = 0, \quad \frac{\partial p}{\partial x} = 0$$

Finally, pressure is held at a fixed value on the outlet along with Neumann homogenous conditions for velocity components:

$$\frac{\partial u}{\partial x} = 0, \quad \frac{\partial w}{\partial x} = 0, \quad p = 0$$

6.2.2 Comparison with experimental data

Here we present the numerical results and compare them with experimental data. The flows over different hills differ in each case. The main distinction in characteristics is the attachment or separation behind the hill. As expected, the separation occurs when the hill is steeper. On the contrary, when the slope is lower, the flow has more tendency to attach to the wall. Moreover, the higher the height of the hill, the larger the area of recirculation behind the hill. These conclusions are based on the experimental study [19]. Nevertheless, our simulations correctly achieve the same results. The Figure 31 presents the resulting velocity fields of flows over the four hill types obtained from the Finite Volume method.

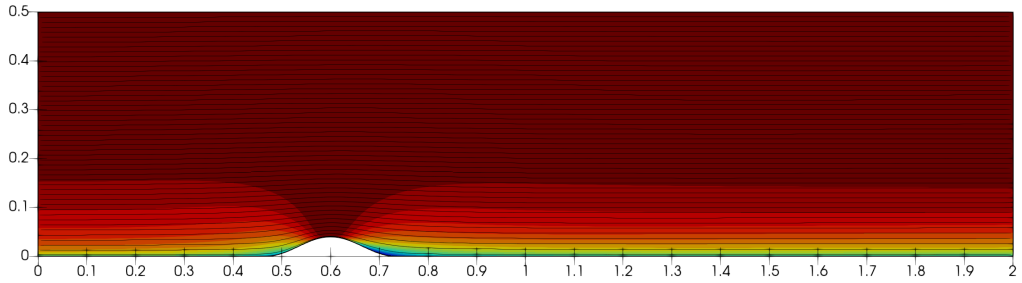

(a) S3H4

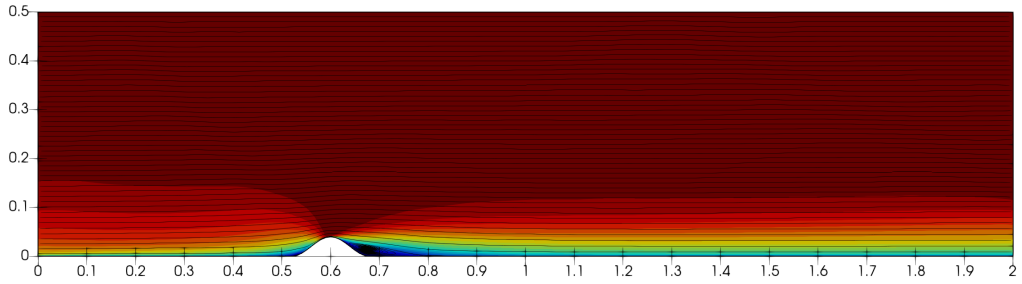

(b) S5H4

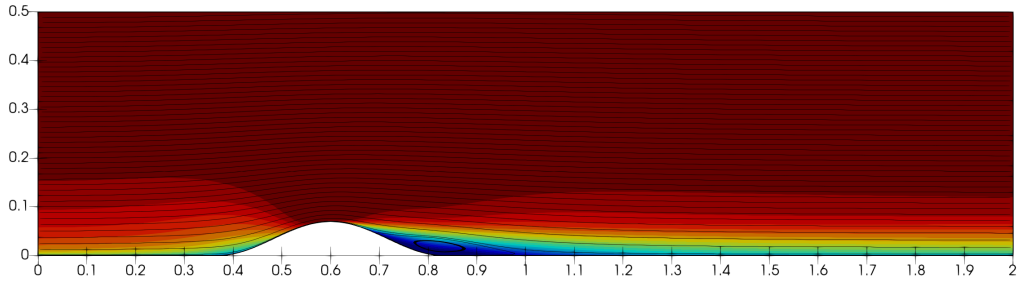

(c) S3H7

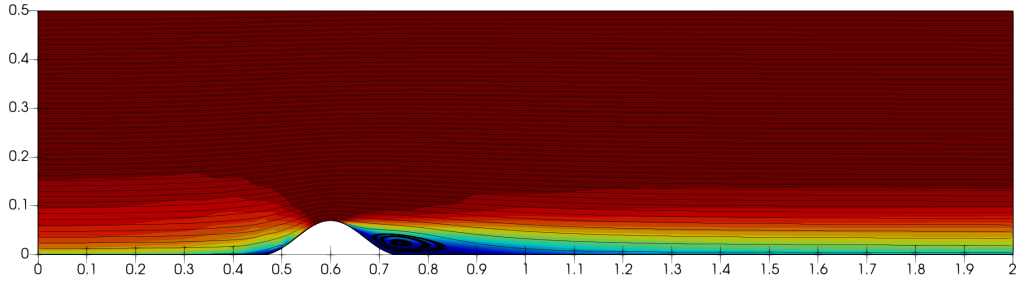

(d) S5H7

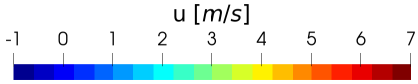

Figure 31: Turbulent flow over hills - velocity fields

The whole computational domain is depicted with total velocity contours and streamlines. The flow is completely attached over the S3H4 hill and separation with recirculation zones are visible behind all the other hills. The biggest difference can be observed between the smaller hills. With the same height only by changing the slope it goes from smooth attached flow over S3H4 to visible separation of significant length behind the S5H4. The separation is caused by more sudden change in flow direction, which is induced by the steepness of the hills S5H4 and S5H7.

To demonstrate the recirculation zones more clearly, domain-wide streamlines are shown for each hill. In the first case, over S3H4, streamlines demonstrate completely attached flow. On the contrary, S5H4, shows the circulating fluid behind the hill. As demonstrated in 32, recirculation grows with the height of the hills and tends to be larger behind the steeper hills. In flow over S3H7 the recirculation forms but only closely to the ground and does not significantly affect the over-going flow. Finally, the largest region of recirculation is behind the hill S5H7.

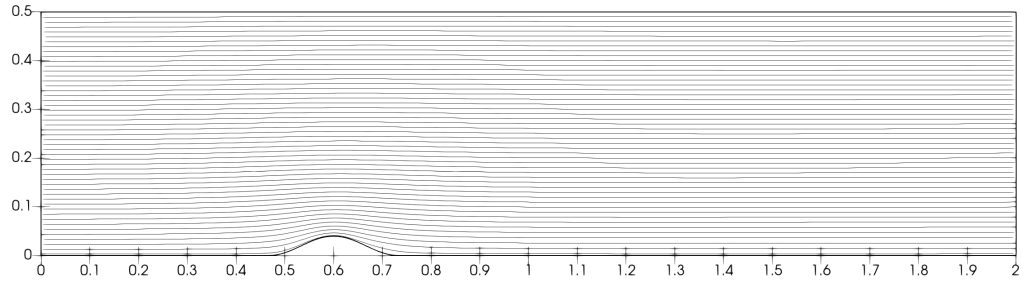

(a) S3H4

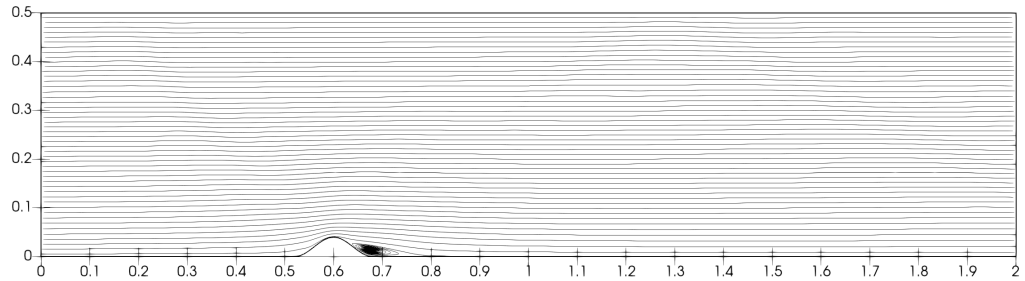

(b) S5H4

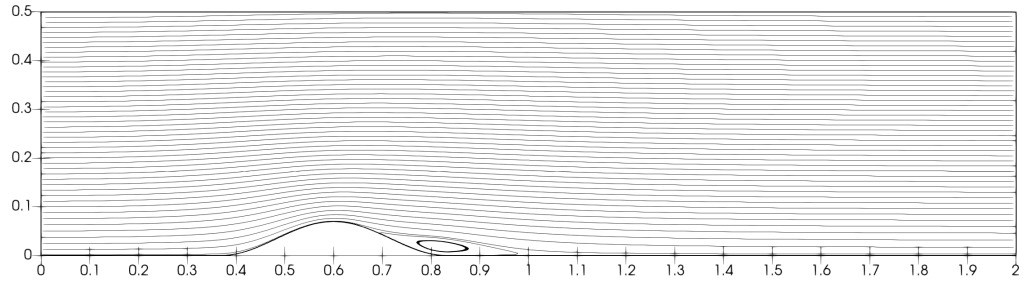

(c) S3H7

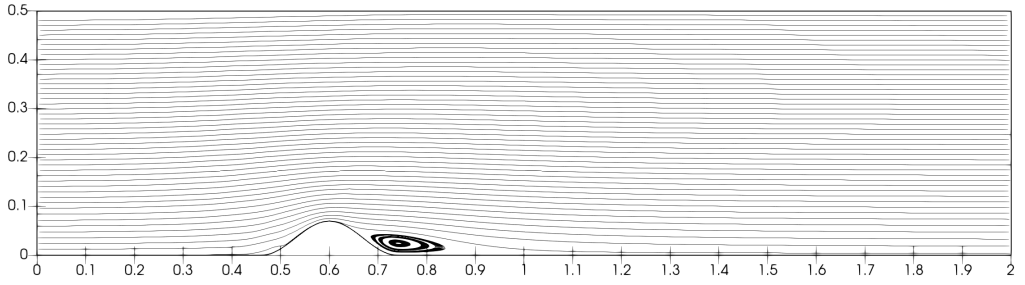

(d) S5H7

Figure 32: Turbulent flow over hill - streamlines

This general description provide expected and meaningful results that are consistent with the conclusions drawn in the study [19]. Nevertheless, in order to properly compare the results from simulations with experimental data, we will discuss the separation regions in more detail. The following two figures show details of the two distant flow regimes over hills S3H4 and S5H4 from the mentioned wind tunnel study in Figure 33 and our simulations in Figure 34. Each sub-figure always depicts only part of the domain in the close vicinity of the hill. In the Figure 33 the axes are described in the relative scale to the hill's properties and the markers ° express the experimental data and solid lines show the results from the simulations conducted in the same study.

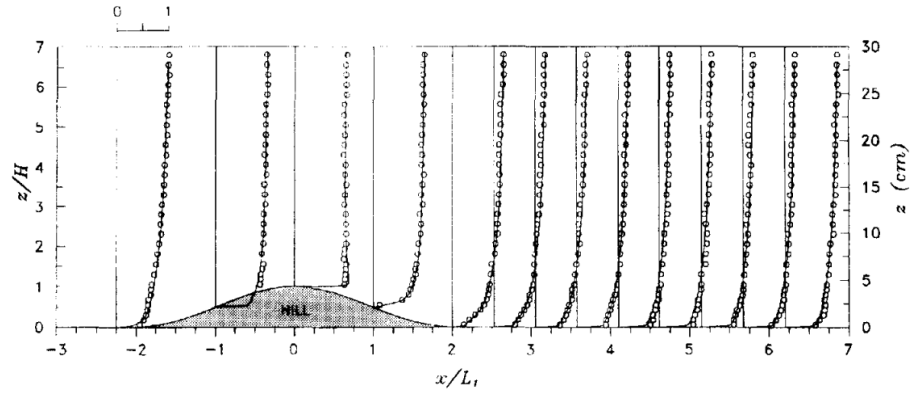

(a) S3H4

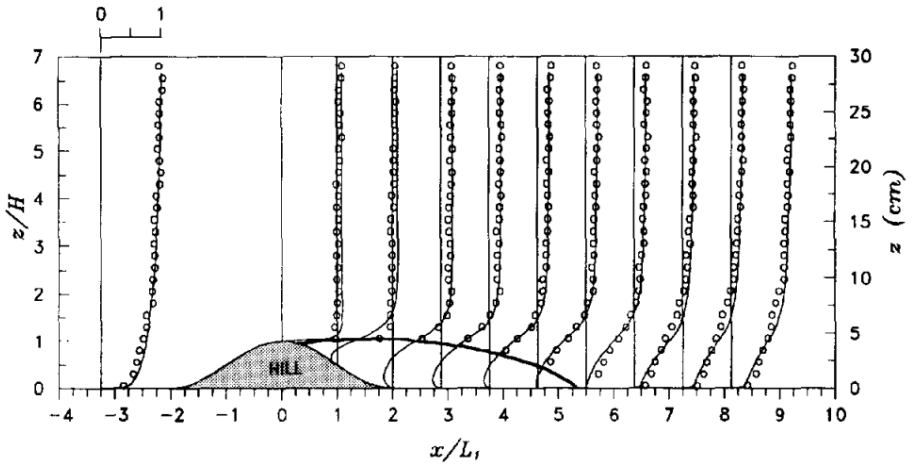

(b) S5H4

Figure 33: Turbulent flow over hills - velocity profiles from experiment, reprinted from [19]

Flow over S3H4 remains attached and no separation occurs. Only change of velocity profile over the hill is visible. The change in profile is expected, because the mass flow must remain the same in the region of the closed wind-tunnel. Therefore, the same amount of fluid mass must flow in each vertical section. Figure 33b with flow over S5H4 shows detail of the separation region. The point of reattachment is measured from the the centre of the hill x_h. In this case the reattachment point is at the position $5.25 \cdot L_1$ from x_h, as the line in the figure indicates. Thus, for S5H4 with $L_1 = 4\,cm$, the flow in the wind tunnel is reattached after $0.21\,m$.

Figure 34, containing results from our simulations, presents similar detail of the separation region, but only in the original coordinate system. However, great effort was made to reproduce the detailed view as close as possible. The centre of the hill is positioned $x_h = 0.6\,m$ and the separation and reattachment points are marked by red arrows.

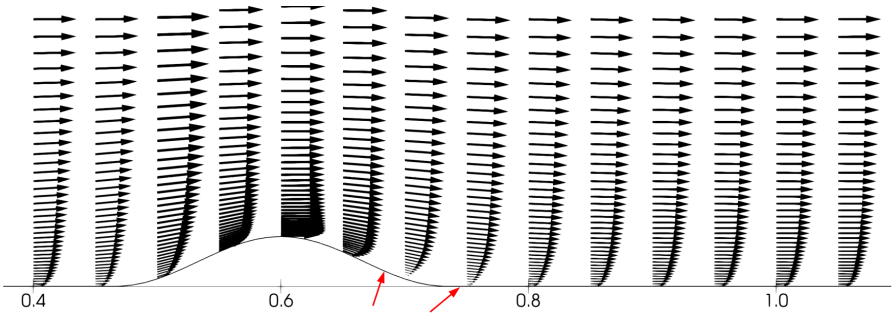

(a) S3H4

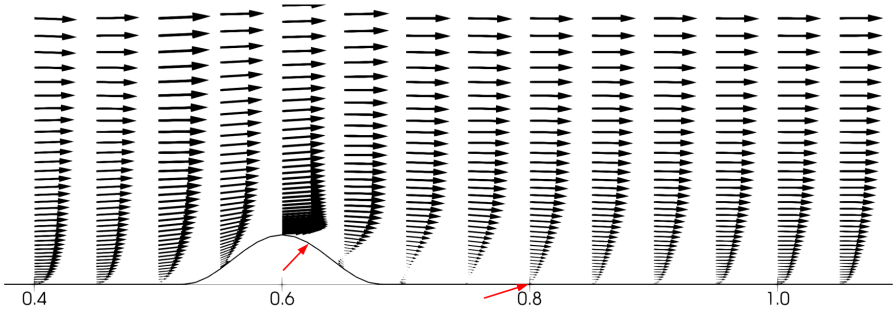

(b) S5H4

Figure 34: Turbulent flow over hills - velocity profiles from simulations using FVM

Similarities are evident in both results. Velocity profiles follow the same patterns. However, in our simulations small separation occurs even over the S3H4 hill. Minor but traceable detachment is marked by the arrows in 34a. In contrast, the authors of the experiment declare no separation in their flow over the S3H4. However, the presented results do not show any visible velocity profile near the downwind foot of the hill, where the very small separation is present in our simulation. Therefore, the minor discrepancy may also be due to the measurement method having difficulty detecting such thin separation. The inaccuracy on our side could be caused by the non-optimal choice of ℓ_∞ influencing the turbulent component of viscosity.

The flow over the second and steeper hill S5H4 results in significant separation region. On the first sight, the velocity profiles coincide. As already stated, the separation in the experiment occurs along the length $r_e = 5.25 \cdot L_1 = 0.21\,m$ behind the hill, where the flow again reattaches. In the results obtained from our simulations, the point of reattachment is at $r_s = 0.2m = (5.0) \cdot L_1$ from the hill centre x_h. In addition, the experiment always operates with a certain degree of uncertainty. The point of reattachment in the [19] was given as $r_e = (5.25 \pm 0.5) \cdot L_1$. The results are thus in a good agreement and we can confirm our data reliable.

Additionally, in order to improve clarity, we provide the velocity contours with streamlines in this detailed view in the Figure 35. The dark blue contours depict the separation areas, small and thin region at the downwind foot of S3H4 not affecting the general flow and larger significant region behind S5H4.

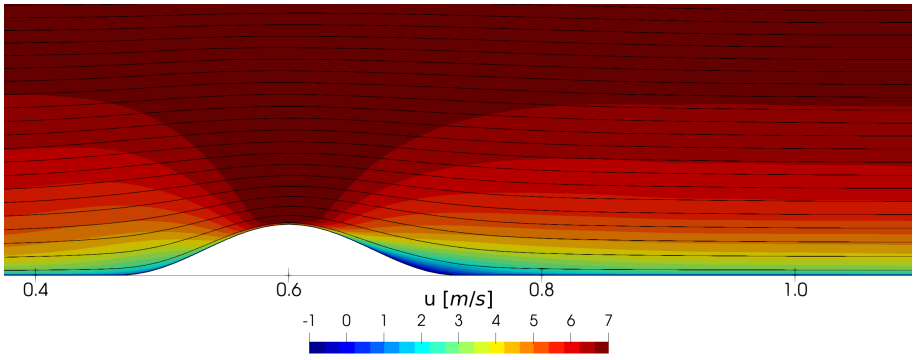

(a) S3H4

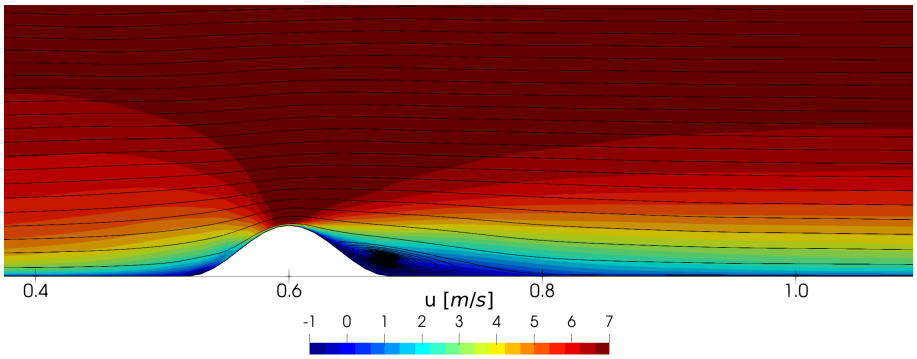

(b) S5H4

Figure 35: Detail of smaller hills regions - contours of velocity with streamlines

After demonstration of the results and discussion over the comparison, we can conclude, that we achieved sufficiently matching results with the experimental data. Therefore, we can state that our FVM simulations provide meaningful and accurate results even for turbulence flows and realistic geometries. All that only with the use of simple turbulence model. It allows us to study the problem in more detail and discuss other approaches. We will now leave the comparison and continue with further investigation of the flows over different hills and discussion of other aspects and influences of the parameters in the numerical simulations.

6.2.3 Investigation of the flows

Similarly as in the previous cases of smaller hills, that were used for comparison with experimental data, we now provide the detailed view of the separation region for the hills S3H7 and S5H7 in Figure 36.

As we can see from the marking arrows, both hills have a significantly long separation region. The reattachment point for both cases lies at the position $0.4\,m$ from the centre of the hill x_c. However, that corresponds to $3.4 \cdot L_1$ for S3H7 and $5.7 \cdot L_1$ for S5H7. Thus, o relative scale, the separation region of S5H7 is substantially (1.7 times) larger the the one of S3H7. In addition, the Figure 37 containing velocity contours with streamlines shows the recirculation zone of S5H7 being larger and more interacting with the over-going flow. The immense influence of the steepness of the hill is thus again demonstrated.

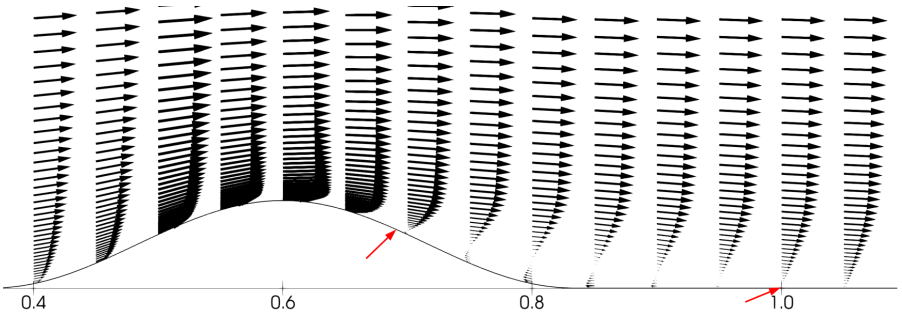

(a) S3H7

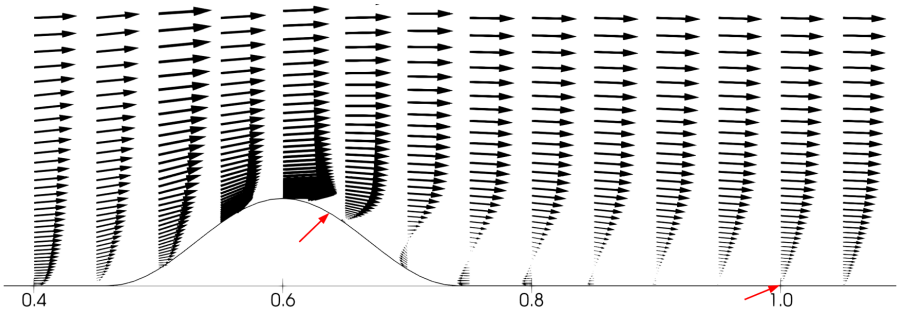

(b) S5H7

Figure 36: Turbulent flow over hills - velocity profiles over higher hills

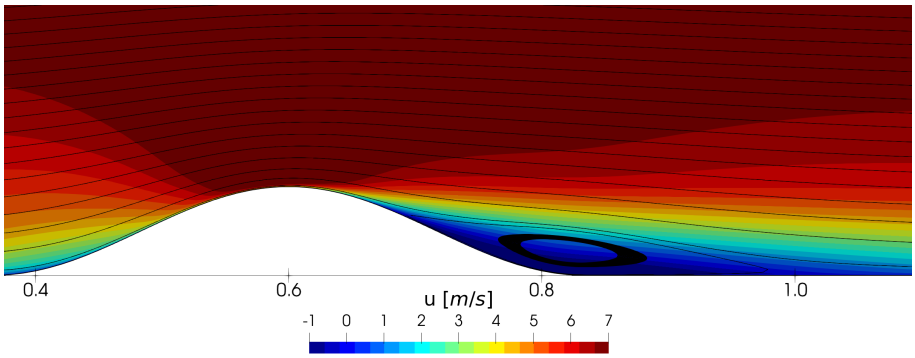

(a) S3H7

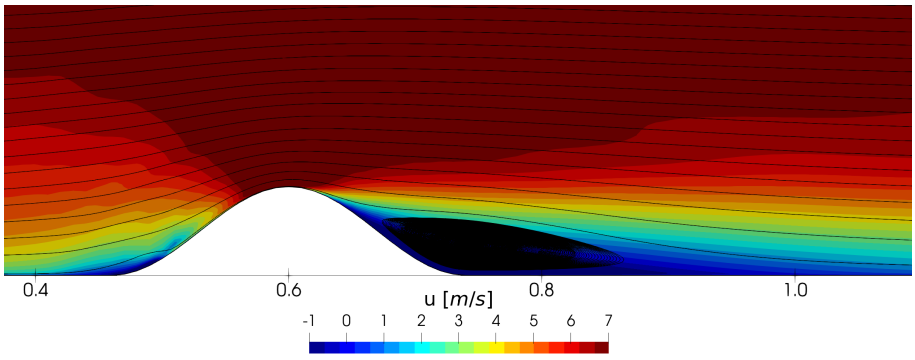

(b) S5H7

Figure 37: Detail of higher hills regions - contours of velocity with streamlines

Other than the horizontal velocity u, that represents the dominant component of the total velocity displayed in the figures above, we also compute and measure the vertical velocity component w and pressure p. Figure 38 shows the vertical flow velocity fields over different hills in the whole computational domain. In all cases, the same and expected pattern is visible. Significant increase of w on the windward side of the hill occurs as the flow is forced upwards, followed by negative values of w (blue regions) on the leeward side indicating a downward direction of the flow.

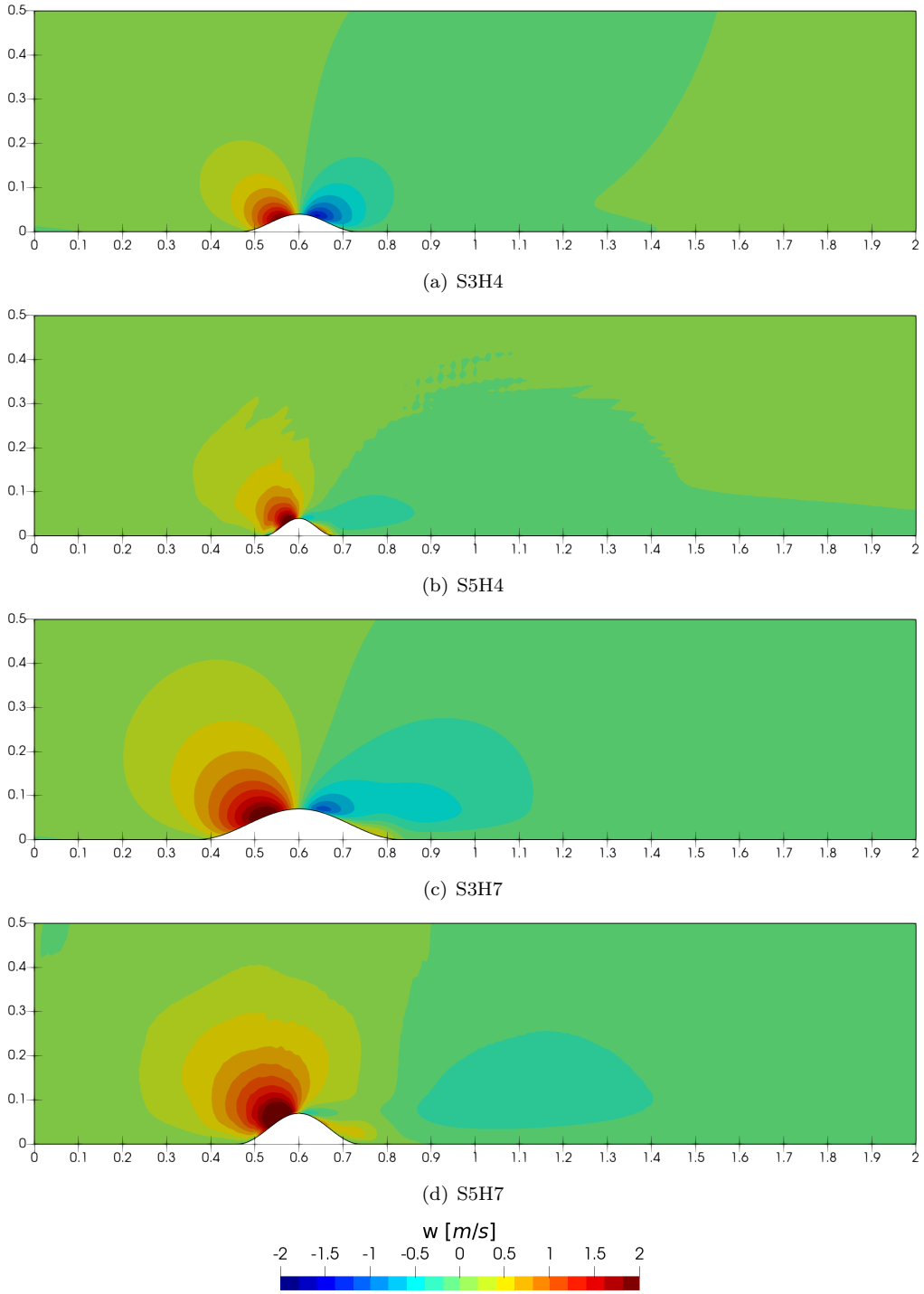

(a) S3H4

(b) S5H4

(c) S3H7

(d) S5H7

Figure 38: Turbulent flow over hills - vertical velocity w fields

However, the magnitude of downward flow varies considerably. In the case of S3H4, where no separation occurs the values of w are almost symmetric around the centre of the hill and closely

attached to it. For the the steeper hill S5H4, however, the flow is not directed downward adjacent to the hill, but slowly slopes further until it reaches the reattachment point at $0.8\,m$. In addition, the positive values of w in the close proximity of the hill on the lee side confirm the presence of recirculation zone behind the hill.

The situation is essentially the same in case of higher hills, only the magnitude of vertical movement increases. The flow over S3H7 is attached more closely to the hill with only small separation at the downwind foot of the hill and big separation with slow reattachment occurs behind the S5H7.

We can also observe the shortcomings of our simulations in the form of oscillations above the steeper hills S5H4 and S5H7. As the contours demonstrate, values of vertical velocity component w do not vary uniformly in space as expected. Due to the steeper hills and more sudden changes in the flow directions, oscillations in this quantity are visible. We have tried to make sure, that these small irregularities are not caused by unsteadiness. In all the presented cases we reached a steady solution. It is demonstrated in the Figure 39, where the residues of numerical solution of flow over the S5H7 hill are depicted.

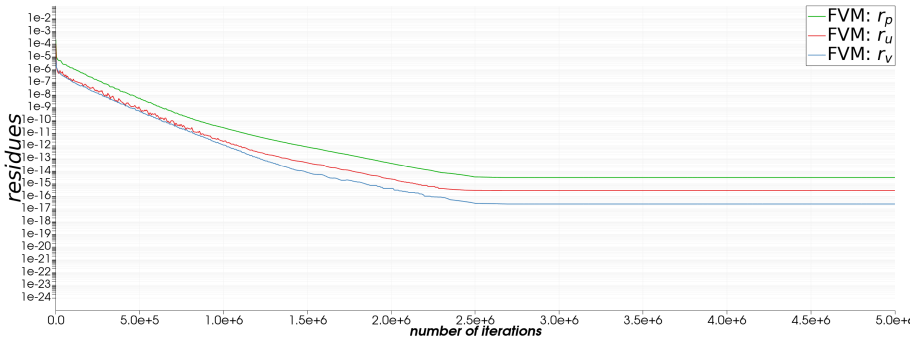

Figure 39: Turbulent flow over a hill - Residues FVM

Ideally, a damping numerical method should be implemented in order to smooth out the oscillations. Since, the main focus was to obtain reasonable overall results and present comparison of different approaches, the numerical damping was not yet implemented in our code. However, addressing this deficiency should be one of the first steps in any subsequent work in order to improve the numerical results.

The numerical oscillations are more obvious in the Figure 40, where pressure distributions around each hill are presented. It is worth reminding, that the pressure field represents the computed values of pressure perturbation component, as it was described in the section concerning mathematical model.

The distributions correspond with the velocity profiles. Above the hill the pressure decreases as the velocity increases due to the conservation of mass in the enclosed space. Consequently in flows above higher hills the low pressure areas are significantly larger as the velocity increases more. In addition, the low pressure extends to the lee side in cases, where the separation occurs. In case of steeper hills, dark blue region of high negative pressure values is extended even to the downwind foot of the hill. Whereas for S3H4 the pressure distribution is again almost symmetrical around the centre of the hill.

Nevertheless, the oscillations are again visible in the flows over steeper hills. Reasonable implementation to suppress the oscillations would be to directly change the computation of new pressure values between predictor and corrector of the MacCormack scheme. The current approach is to calculate the next value of $p_{i,j}^{n+1}$ using the values from previous step $\tilde{p}_{i,j}^{n+1/2}$ in the centre of the cells. What could help to smoothen the oscillations is to not take the centre values, but to calculate the average from the four vertices surrounding it. In this way, we suppress the sudden changes in values in neighbouring cells. Implementation to only pressure field will not aggressively effect the solution in general, but still could help to damp the oscillations. It is a damping method that was used in similar in the Lax-Friedrichs scheme in the preceding work. However, as already stated before, numerical damping of any sort in the FVM was not yet properly tested for the presented problem.

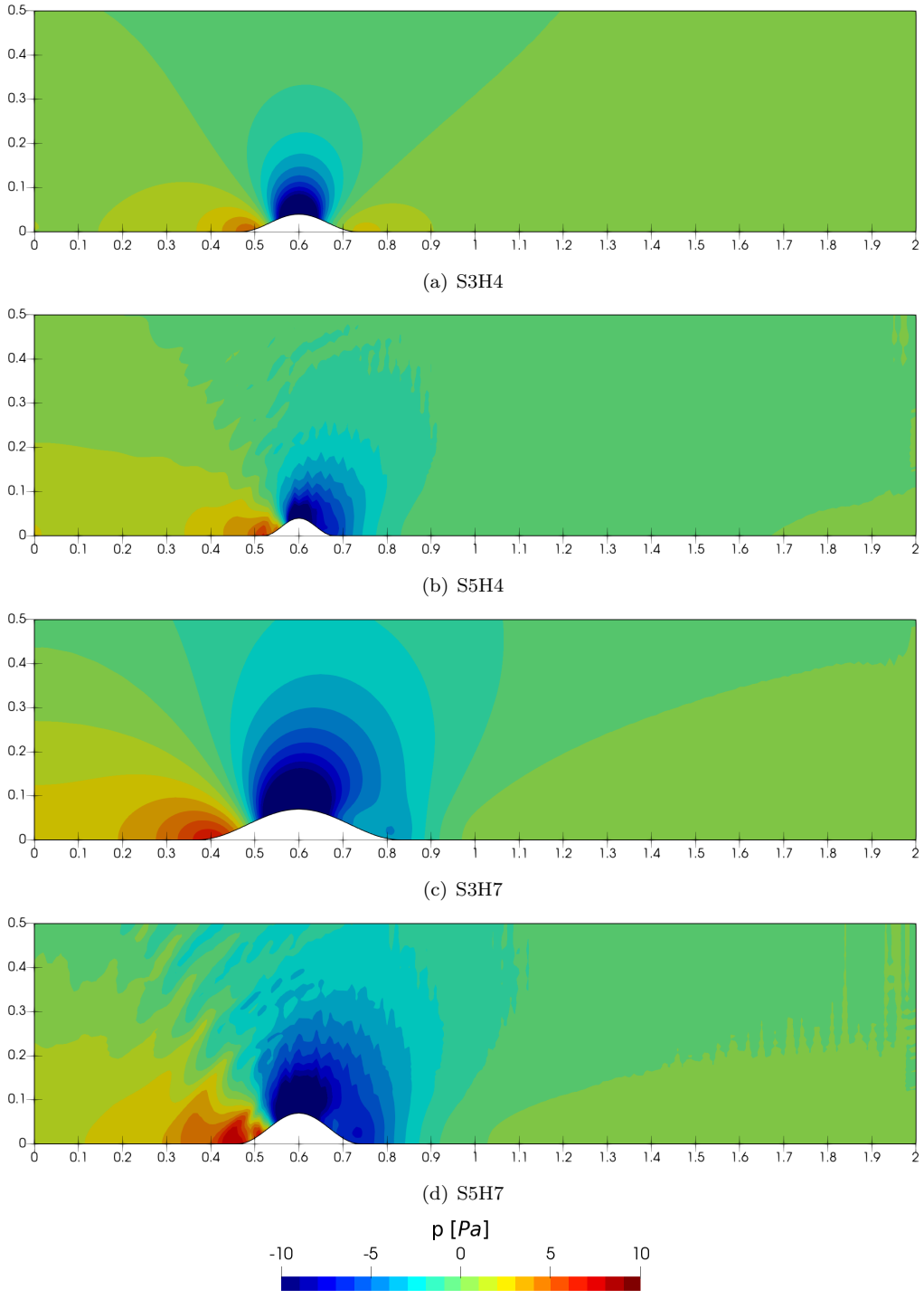

(a) S3H4

(b) S5H4

(c) S3H7

(d) S5H7

Figure 40: Turbulent flow over hills - pressure p fields

6.2.4 Mesh dependency

In this section, the mesh dependency of the results is presented. First, we focus on the influence of number of grid points used in the vertical direction of gradually refinement mesh. We stay with the same problem of atmospheric flow over a sinusoidal hill. Although, for the discussion of mesh dependency we only show the results for hill S5H4.

Many meshes were tested in order to find the optimal mesh for all the simulations. For brevity, only a subset of the results is presented. Testing of the mesh dependency of gradual refinement was performed by changing the number of grid points in the vertical direction along with a corre-

sponding change of the minimum cell size. In doing so, we kept the rate of change constant and eliminated the inaccuracy due to the lack of smoothness. The following results concern meshes varying at the scale of 2. Figure 41 displays the velocity fields of results obtained on different meshes. It proceeds from the top from the coarsest to the finest mesh. The label always states the number of points in horizontal and vertical directions as $n_x \times n_z$.

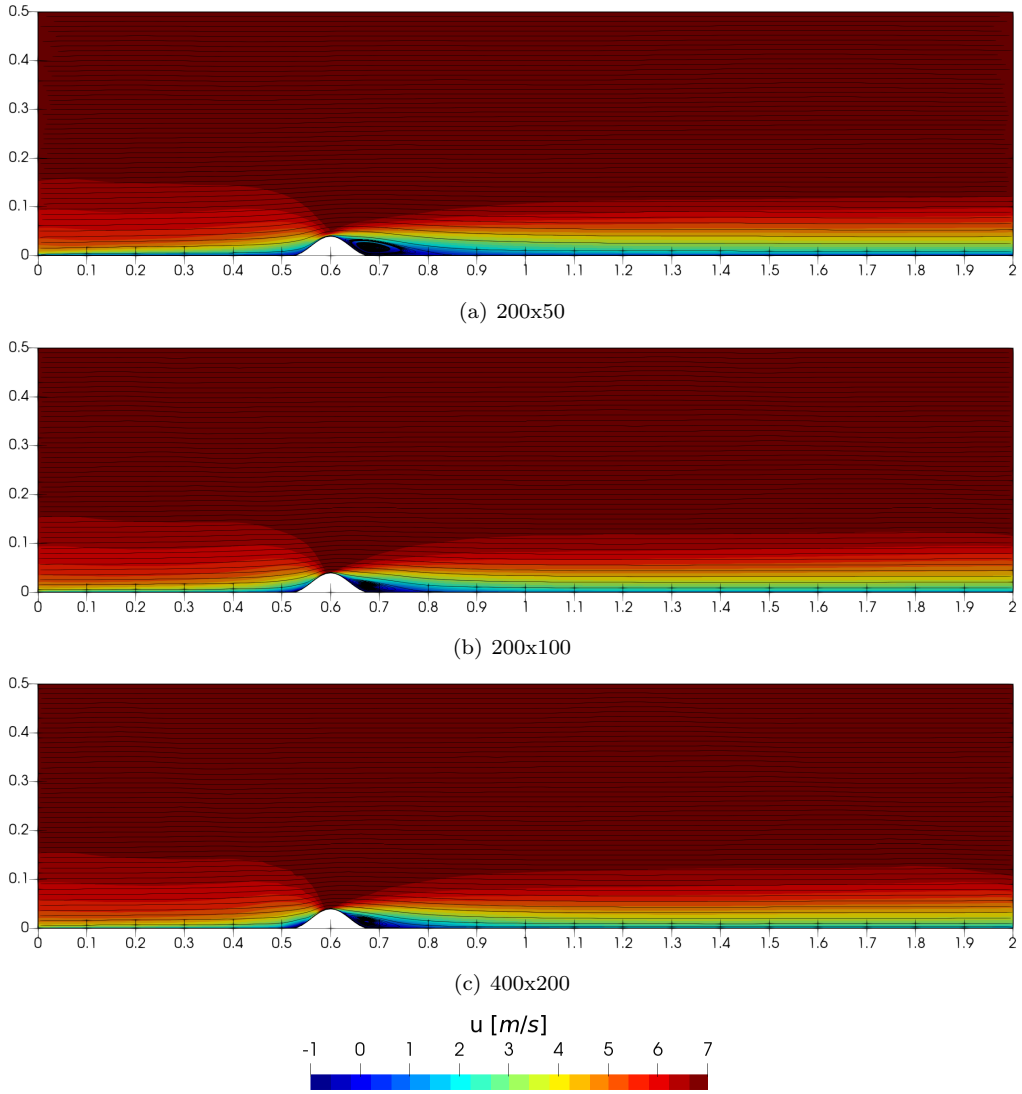

(a) 200x50

(b) 200x100

(c) 400x200

Figure 41: Mesh dependency - velocity fields

The mesh in the middle represents the one, that was finally selected and whose results were validated against experimental data in the previous section. We can see that on the mesh 200x50 the separation region behind the hill is overestimated. This means the mesh does not sufficiently resolve the near wall reagion correctly. Rest of the domain seems to be indistinguishable. Therefore, we present the detailed section around the hill with velocity profiles.

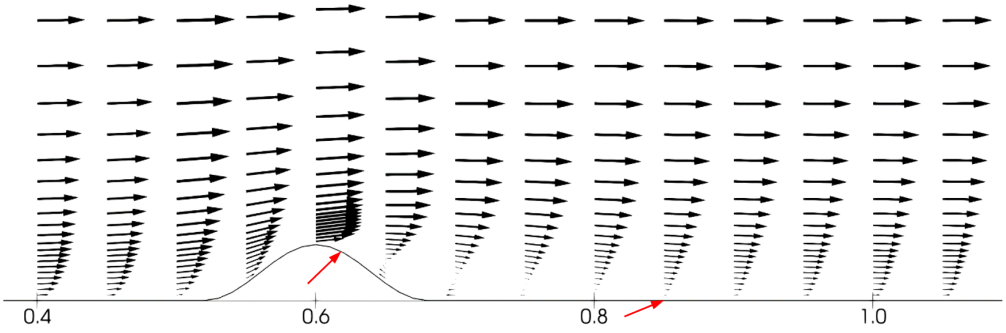

(a) 200x50

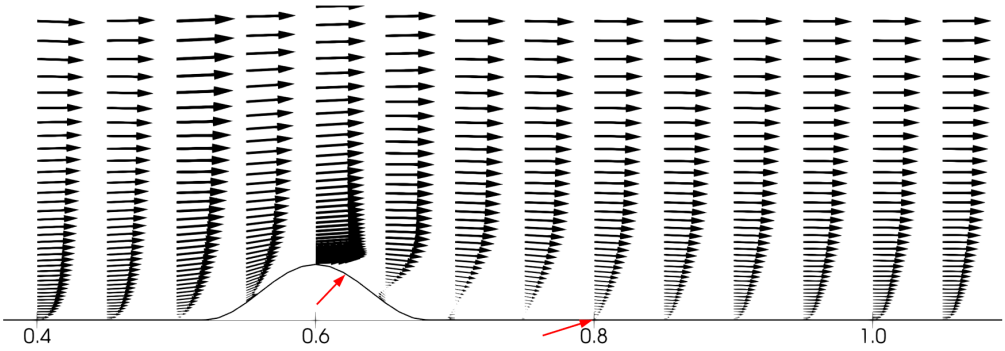

(b) 200x100

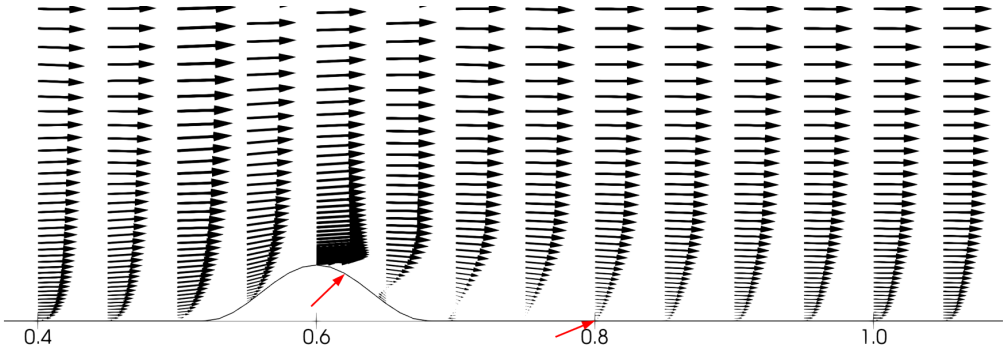

(c) 400x200

Figure 42: Mesh dependency - velocity profiles

Figure 42 confirms the first conclusion of excessive separation region on the coarsest mesh. The reattachment point is further downwind from the hill as the arrow indicates. In addition, the velocity profile above the hill does not match the expected profile with higher velocity near the ground. Therefore, it had to be refined in order to accurately capture it.

On the other hand, further refinement had no significant effect. The results are totally consistent, as can be seen in both Figure 41 with velocity contours in the whole domain and 42, where the points on velocity profiles (number of arrows with velocity magnitude) were deliberately set the same in the post-processing to demonstrate the similarities. Moreover, the double refinement was carried out not only in the vertical direction but also in the horizontal direction. However, that did not bring any improvement. Thus, no further refinement is necessary and the 200x100 grid can be declared optimal for our purposes.

Nevertheless, due to the existing oscillations in some of the results, as it was demonstrated in the previous section, for every subsequent work it would be reasonable to consider less radical coarsening in the upper parts of the domain. Slower coarsening of the mesh or using equidistant cells in the upper region may also help to mitigate the oscillations and improve the numerical results in general.

Apart from that, in order to demonstrate the advantages of gradually refined mesh we present

the following Figure 43 with comparison of gradually refined mesh and equidistant (in each direction separately) mesh. Due to the reason that the main differences occur in the close vicinity of the hill, we show only the detailed section with velocity profiles.

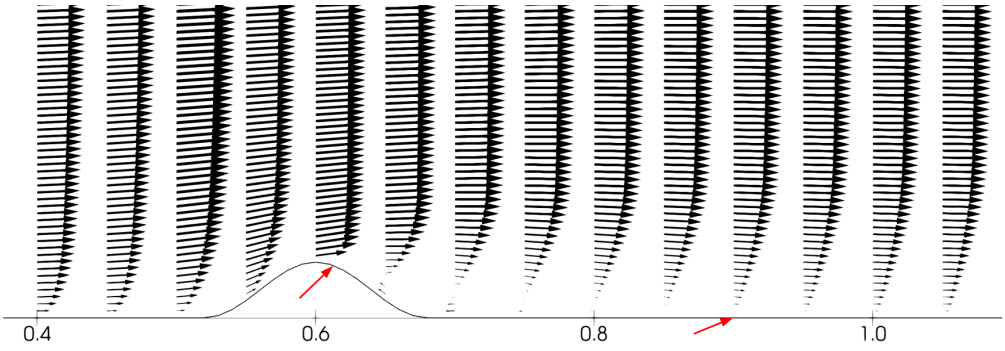

(a) Equidistant mesh - 200x100

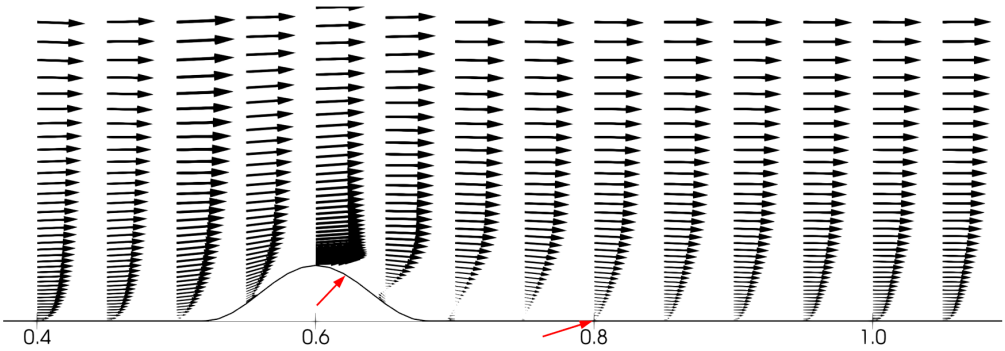

(b) Gradually refined mesh - 200x100

Figure 43: Mesh comparison: velocity profiles

Both meshes consist of the same number of points 200x100 in horizontal and vertical directions respectively. However, the differences in the results are significant. Similarly to the previous case, equidistant mesh does not resolve the region near the ground correctly. The reattachment point is 1.5 times farther downwind than when using gradually refined mesh. The velocity profiles over the hill also do coincide.

The situation is even worse than in case of 200x50 gradually refined mesh. It is so, due to the different smallest size of the cell edge length in vertical direction Δz_{min}, located near the ground. For the gradually refined mesh with 200x100 points the value $\Delta z_{min} = 1 \cdot 10^{-3}\, m$ is set. Whereas for the equidistant mesh the size of the cell near the ground equal to the size of all the other cells, which is 5 times larger.

In this mesh-dependency section we validated our choice of the computational mesh. Any further results presented in this work are also conducted on this mesh without explicitly stating so.

6.2.5 Comparison of numerical methods

Further we approach to discussion about the accuracy and practicality of the numerical methods. We present the comparison of DIF and FVM side by side of all the hills studied. The following Figure 44 contains velocity fields with streamlines of the whole computational domain. Finite Difference Method is again presented on the left side and Finite Volume Method on the right. The setup and initial parameters are exactly same in both cases. Simulations using FVM were conducted on the wall-fitted gradually refined mesh discussed in the previous section. DIF simulations on the other hand, due to simpler implementation in existing code, were conducted on equidistant mesh (of corresponding size to match the Δz_{min}) with the use of immersed boundary method. Thus, the hill is actually part of the computational domain and is only marked by white

line in the figure. Blue colour in the area of the hill reflects the enforced zero velocity instead of real obstacle.

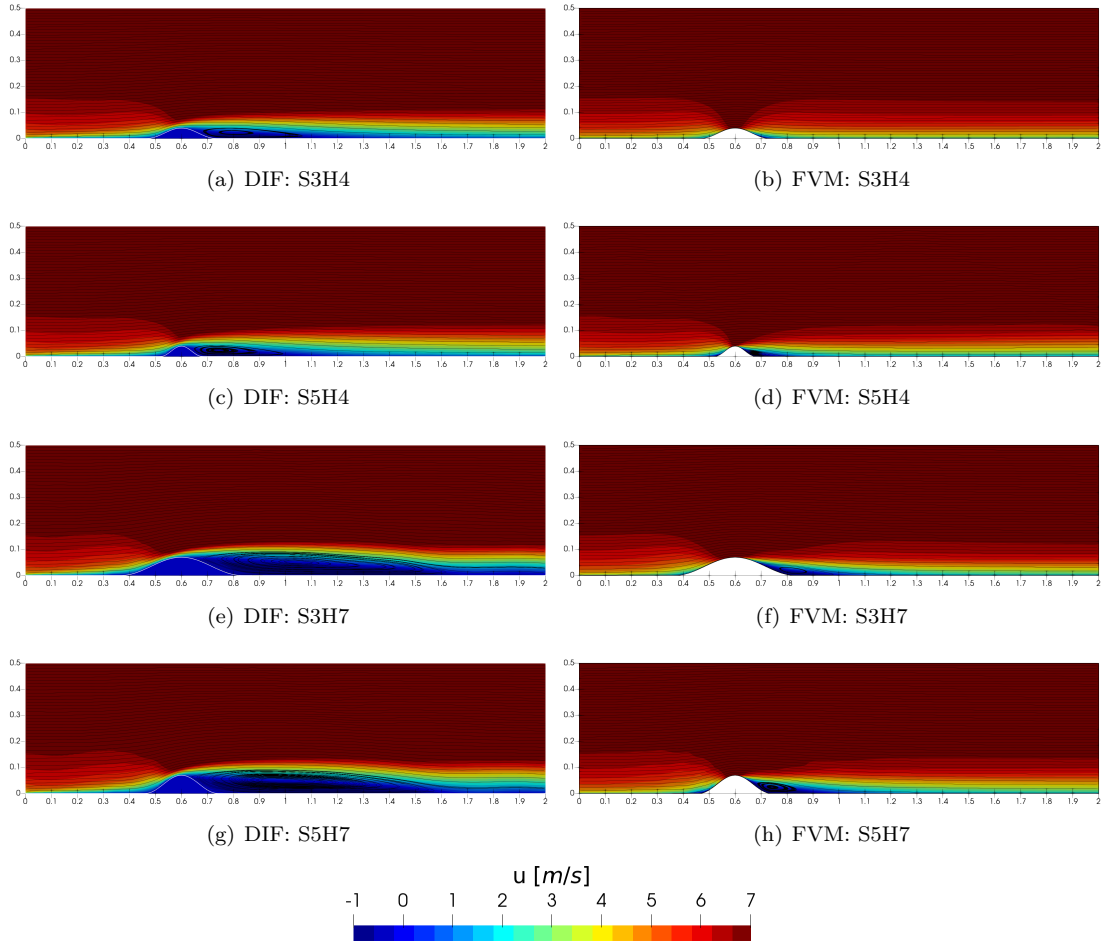

(a) DIF: S3H4 (b) FVM: S3H4

(c) DIF: S5H4 (d) FVM: S5H4

(e) DIF: S3H7 (f) FVM: S3H7

(g) DIF: S5H7 (h) FVM: S5H7

Figure 44: Comparison of methods - velocity fields

At a first glance, significant differences are clearly visible. DIF, where the separation is vastly larger than in the validated FVM case. Even for the least disruptive hill S3H4 a significant separation occurs. In the case of higher hills S3H7 and S5H7 we can even observe recirculation zones of three times the size of the hills themselves. That is clearly demonstrated in Figure 45.

As the methods were used on the exact same setup and under the exact same conditions, it is difficult to explain the significant differences only by one cause. We already discussed the reasonable accuracy of the FVM. Therefore, we consider the solutions from DIF as incorrect. Some of the inaccuracy probably falls on the approach of modelling the obstacle. The method of simple immersed boundary, where the hill is part of the meshed domain and only the velocity is enforced zero may not be sufficient enough for simulations of turbulent flows. The zero velocity persists behind the hill are much longer than it should. The flow in DIF simulations is too deflected upwards, creating an overestimating recirculation region delaying the flow reattachment.

The advantage of FVM with wall-fitted mesh is also that the shape of the hill and the position of the grid points are specifically controlled. It is determined in the meshing process, as the mesh follows the shape given by the expression 6.2. In contrast, when using the immersed boundary method, the hill is part of meshed domain and only in the points located under or on the curve of the hill the velocity is enforced zero. Which may result in sharp corners, causing additional separation. In addition, these imperfections are exposed more in the turbulent flow regime.

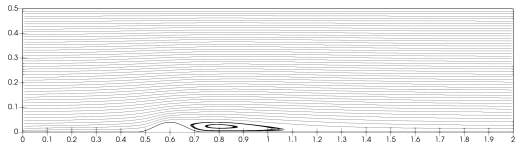

(a) DIF: S3H4

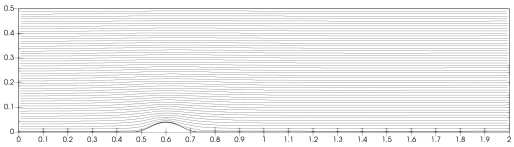

(b) FVM: S3H4

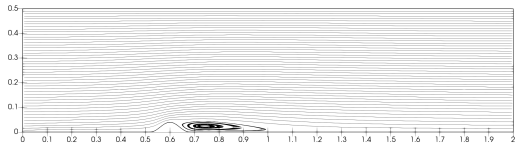

(c) DIF: S5H4

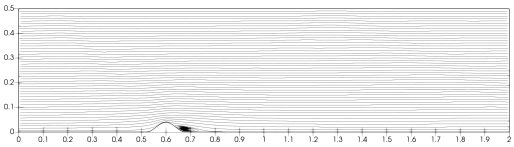

(d) FVM: S5H4

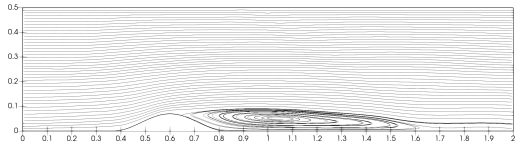

(e) DIF: S3H7

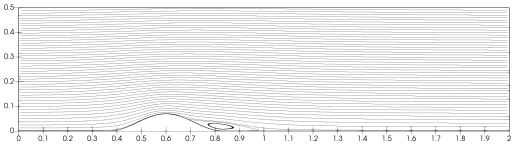

(f) FVM: S3H7

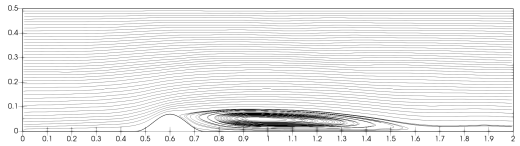

(g) DIF: S5H7

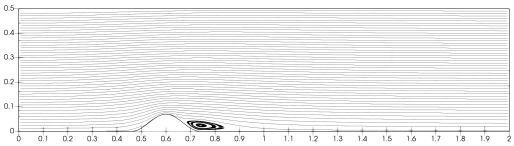

(h) FVM: S5H7

Figure 45: Comparison of methods - streamlines

However, the results are too distant to account the differences only to the immersed boundary method or the form of discretization in DIF method. At least part of the problem lies in the implementation of the turbulence model to the code with finite differences. In the laminar case, earlier in this section, we found solid correlations between the methods. However, the modelling of the turbulence is clearly not accurate in this case.

In the problem of laminar flow over a hill, a stably stratified fluid could have had additional influence on suppressing the differences between the methods. The stratification used was rather strong, therefore the induced vertical movement could outweigh other influences. Nevertheless, in this case of neutrally stratified fluid in turbulent regime, we are witnessing clearly non-matching results. The problem probably lies in some mistake in the code development, which has not yet been found, but will certainly be the objective of any further work on the custom code.

6.2.6 Boundary conditions discussion

In this section, we differ from the study [19] in regards to boundary conditions. The experiment was performed in an wind tunnel, where they have stated maximum developed velocity at a certain height from the ground. The enclosed space of a wind tunnel has its limitations and do not precisely match the open region of real flow in ABL.

Nevertheless, we achieved matching results from our simulations using corresponding boundary

conditions. On the top the following Dirichlet boundary conditions were imposed:

$$u = u_{max}, \quad w = 0.$$

With respect to studying atmospheric flows, a wind tunnel has the limitations of confined space.In nature, there are no solid top boundaries that limit the space in which the fluid flows. However, numerical simulations do not have to be constrained by these limitations. We can simply use different, however appropriate boundary conditions. The approach to more real atmospheric flow in open area is to consider the top boundary as a free stream. In the simulations we therefore impose the homogenous Neumann conditions, namely:

$$\frac{\partial u}{\partial z} = 0, \quad \frac{\partial w}{\partial z} = 0, \quad \frac{\partial p}{\partial z} = 0.$$

Many tests and simulations over all the different hill shapes were performed. We provide the summarization of the results in the following figures to clearly show differences and impacts of the boundary conditions described above.

First, the Figure 46 displays the general overview of velocity contours with streamlines in the whole domain. On the left we can find the results using Dirichlet conditions for velocity components on the top boundary and on the right the results with Neumann homogenous conditions. We can clearly see that when the conditions are set up to reflect wind tunnel testing, the separation regions behind the hills are smaller than in the case of free stream top boundary.

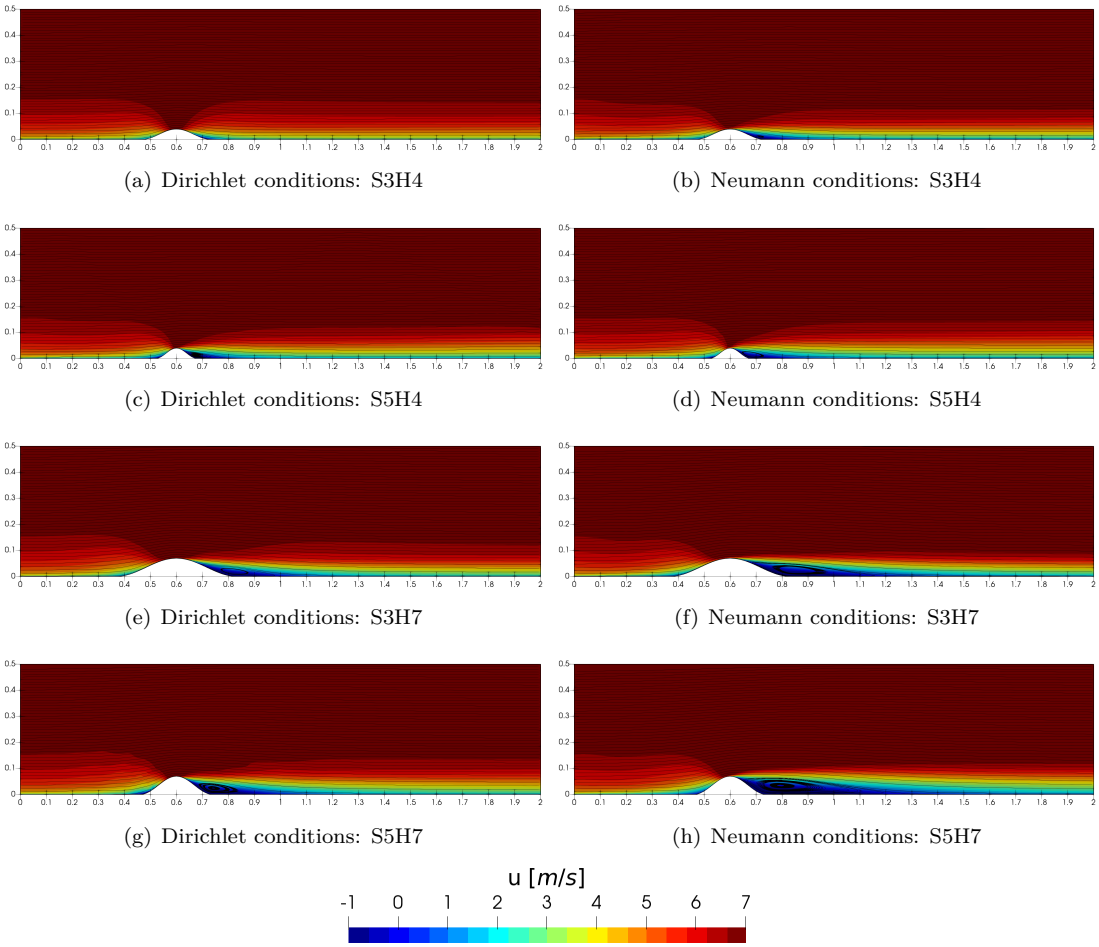

(a) Dirichlet conditions: S3H4

(b) Neumann conditions: S3H4

(c) Dirichlet conditions: S5H4

(d) Neumann conditions: S5H4

(e) Dirichlet conditions: S3H7

(f) Neumann conditions: S3H7

(g) Dirichlet conditions: S5H7

(h) Neumann conditions: S5H7

Figure 46: Comparison of boundary conditions - velocity fields

Across the free stream boundary, the flow is allowed to escape the computational domain, which we assume to be only a part of open space above the ground. For that reason, the streamlines are deflected upwards when encountering the obstacle, especially in the case of higher hills. Since the flow is not pushed downwards due to existing solid boundary, bigger recirculation zone is created behind the hill. Figure 47 shows the streamlines alone to depict the situation more clearly.

We can observe that even for the least disruptive hill S3H4 a small recirculation zone is formed. For the higher hills it is even more significant, as the recirculation is considerably larger and the reattachment of the flow is farther downwind.

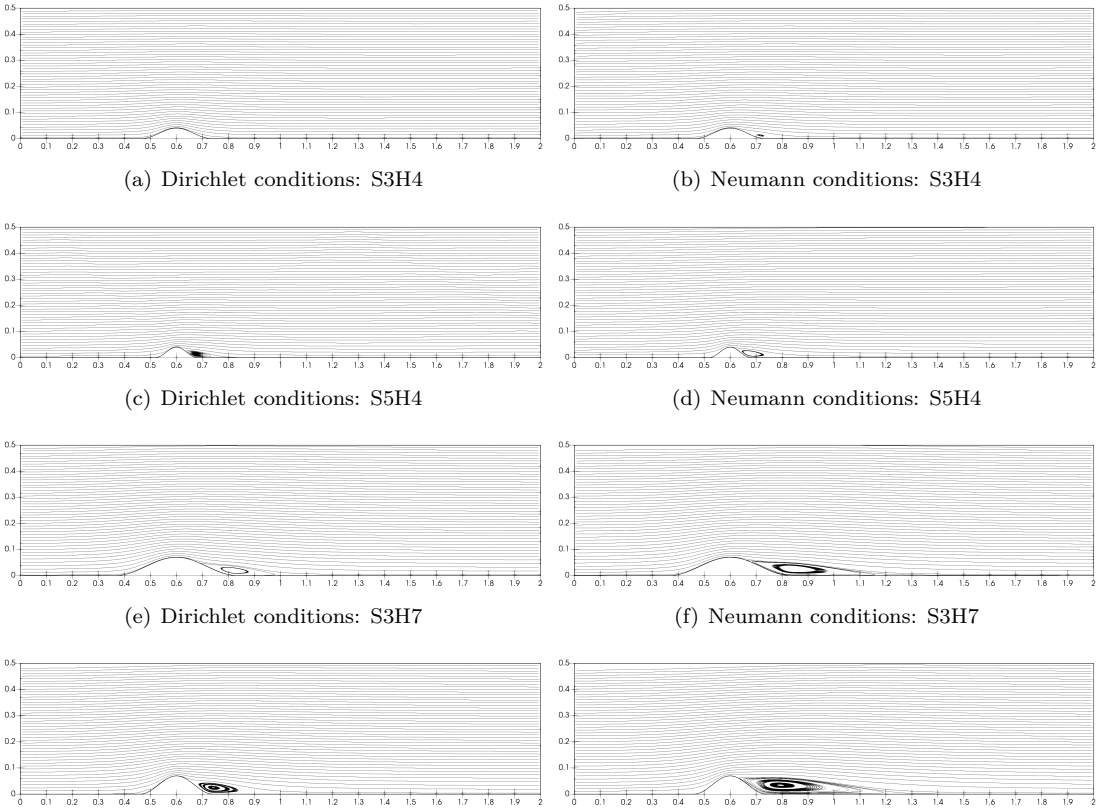

(a) Dirichlet conditions: S3H4

(b) Neumann conditions: S3H4

(c) Dirichlet conditions: S5H4

(d) Neumann conditions: S5H4

(e) Dirichlet conditions: S3H7

(f) Neumann conditions: S3H7

(g) Dirichlet conditions: S5H7

(h) Neumann conditions: S5H7

Figure 47: Comparison of boundary conditions - streamlines

For better visibility, we provide the Figure 48 with detailed region around two of the hills showing the biggest differences. It demonstrates the significant increase in the recirculation zones on the lee side of the hills. The possibility for the flow to expand through the top boundary has thus non-negligible impact on the flow near to the ground.

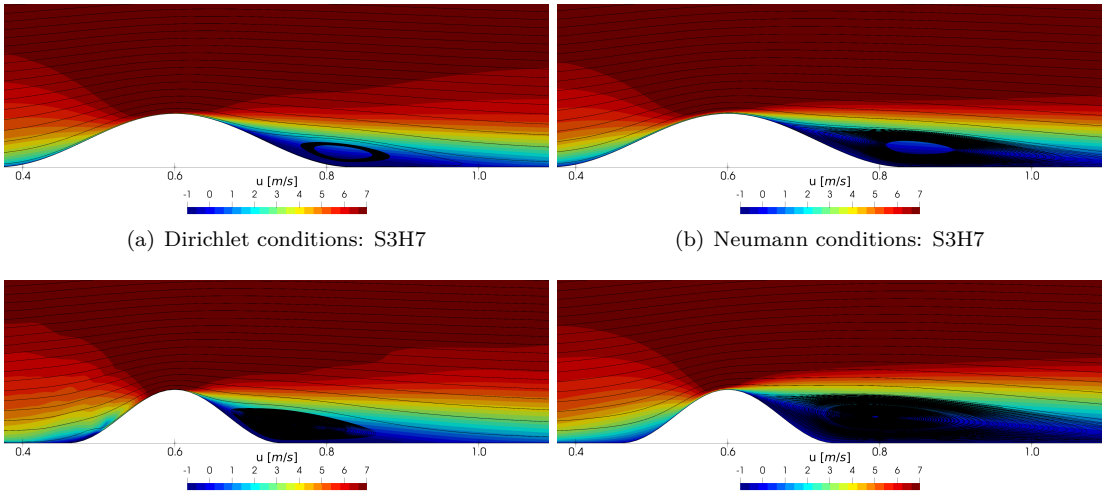

(a) Dirichlet conditions: S3H7

(b) Neumann conditions: S3H7

(c) Dirichlet conditions: S5H7

(d) Neumann conditions: S5H7

Figure 48: Comparison of boundary conditions - velocity detail fields

To be complete in the velocity description, we additionally present the vertical component in Figure 49. The contours just confirm the above stated conclusions. We can observe a decrease in te blue regions representing smaller downward movement. Dirichlet conditions cause the flow to be more attached to the ground. Neumann conditions on the other hand allow the flow to continue upwards, therefore the downward movement behind the hill is less and the reattachment occurs more slowly.

In addition, we can see an improvement in terms of oscillations. Using Dirichlet conditions has led to generally reasonably accurate results, but some quantities, including vertical velocity component w, showed visible numerical oscillations. We already provided some suggestions, how to numerically dampen the irregularities. Nevertheless, the choice of Neumann homogenous conditions visibly helped to smooth the contours of w.

It is worth reminding that both solutions were conducted on the very same gradually refined mesh and differed only in the boundary conditions. We can then interpret it as that the free stream boundary does not aggressively prescribe exact values along the entire boundary, but uses values in neighbouring cells. That allows for the values in the domain to change gradually instead of oscillating between values of neighbouring cells.

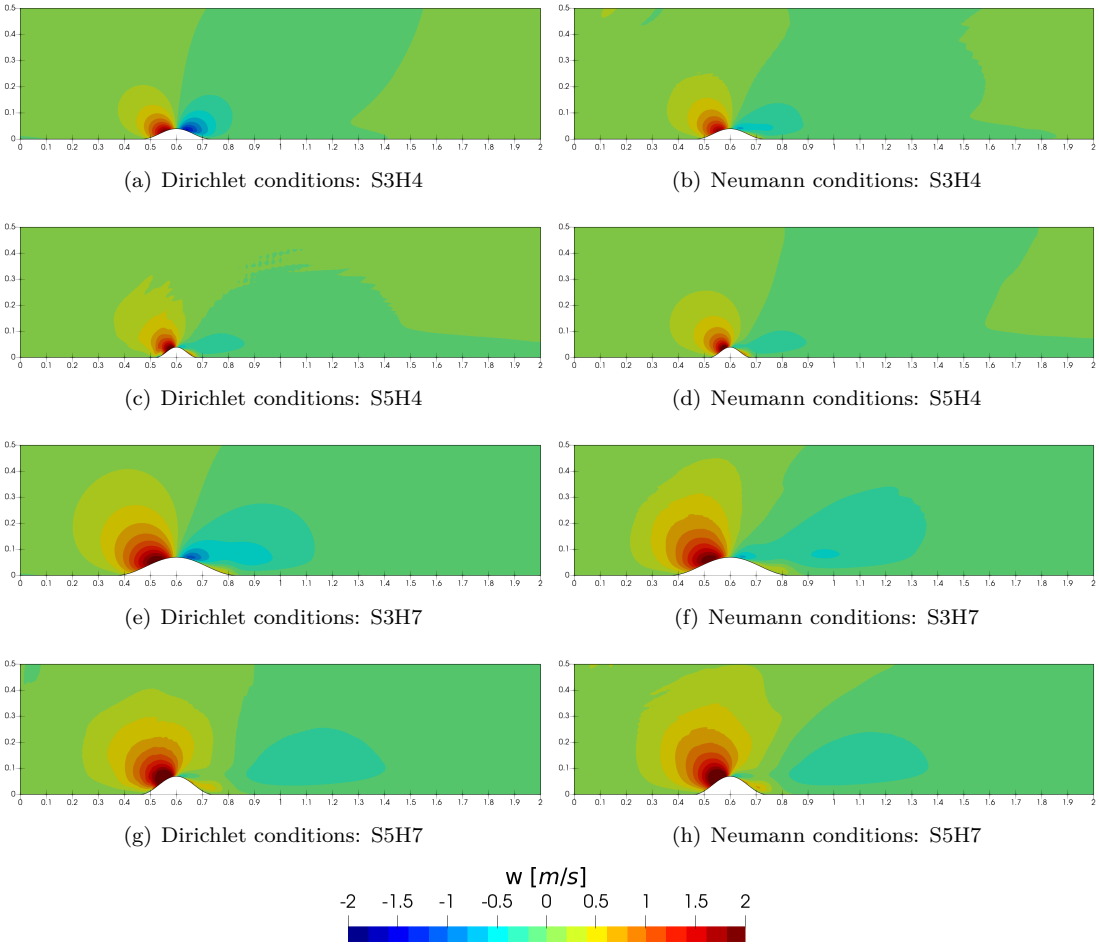

(a) Dirichlet conditions: S3H4

(b) Neumann conditions: S3H4

(c) Dirichlet conditions: S5H4

(d) Neumann conditions: S5H4

(e) Dirichlet conditions: S3H7

(f) Neumann conditions: S3H7

(g) Dirichlet conditions: S5H7

(h) Neumann conditions: S5H7

Figure 49: Comparison of boundary conditions - vertical velocity components

In conclusion, the importance and influence of the boundary conditions should certainly not be underestimated. Our effort was made to develop a setup, that more closely approximates real atmospheric flows. The change of boundary conditions is again one small step in that direction. Therefore, with many simplifications made still in mind, we will continue to further study of the flows with the free stream boundary conditions. In the next section, we will proceed with implementation of the commonly neglected density stratification.

6.2.7 Stratification impact

Now we approach to the influence of stratification. So far, we have presented and discussed the problem of turbulent flows over hills in neutrally stratified fluid medium. As explained previously in the work, assumption of constant density ρ is a common simplification, but does not fully correspond to real atmospheric flows. Therefore, in this section we present the results and comparison of neutral, stable and unstable stratification.

We then use the full system of equations (3.38), (3.39) and (3.40). The implementation and calculation of the density perturbation ρ' was already validated in the previous section. The stratification is controlled via the Richardson number Ri. We use the the values $Ri_n = 0$, $Ri_s = 1$ and $Ri_u = -1$ for neutral, stable and unstable stratification respectively. The values represent rather stronger in order to demonstrate the effects of stratification.

The setup is the same as in the previous cases, with the chosen gradually refined mesh. For boundary conditions the variant including free stream at the top boundary is imposed, as the computational domain represents part of open space in the atmospheric boundary layer. Moreover, we present the results again only on the flow over the S5H4 hill.

Figure 50 shows the contours of velocity with streamlines. The neutral stratification, investigated in all previous sections is at the top, followed by stable and unstable stratification. The

impact of stable stratification is not as significant as unstable stratification, which completely changes the nature of the flow. However, even when the general flow in stable stratified fluid is maintained, the increase in recirculation zone occurs.

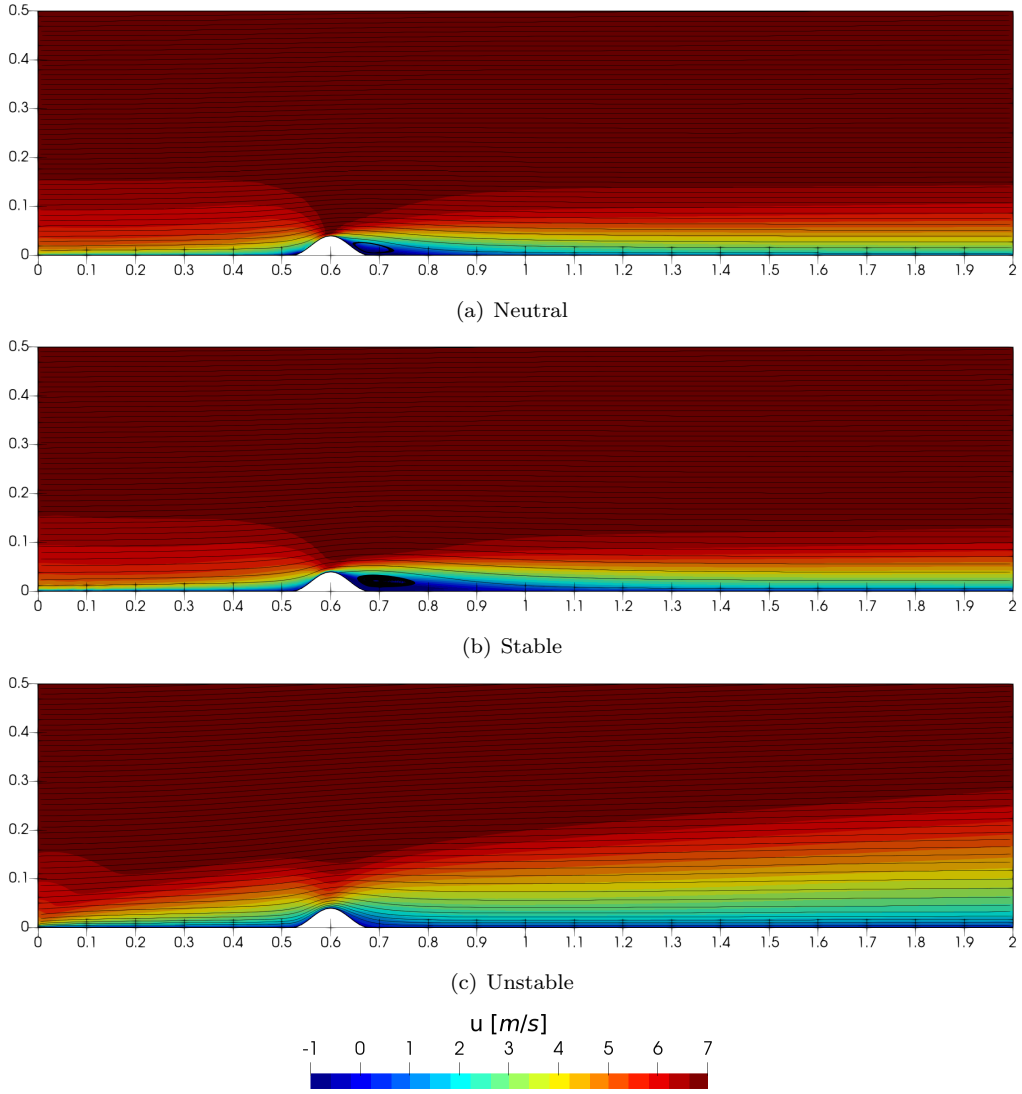

(a) Neutral

(b) Stable

(c) Unstable

Figure 50: Stratification influence - velocity fields

Unstable stratification provides visibly different results. The general flow slows considerably as it interacts with the obstacle. The velocity profile behind the hill does not return to its original form. It shows quite the contrary. The depth of the boundary layer increases steadily throughout the domain. Thus, we can see significant consequences even far from the hill itself.

Following figure 51 with streamlines demonstrates increase of the recirculation zone behind the hill in the stably stratified fluid. In contrast, no recirculation zone is formed in the unstable stratification. The horizontal velocity decreases while the vertical movement is gaining importance, deflecting the flow upwards but at the same time the fluid fills the region behind the hill. That results in the streamlines passing through the top free stream boundary and no recirculation zone is formed.

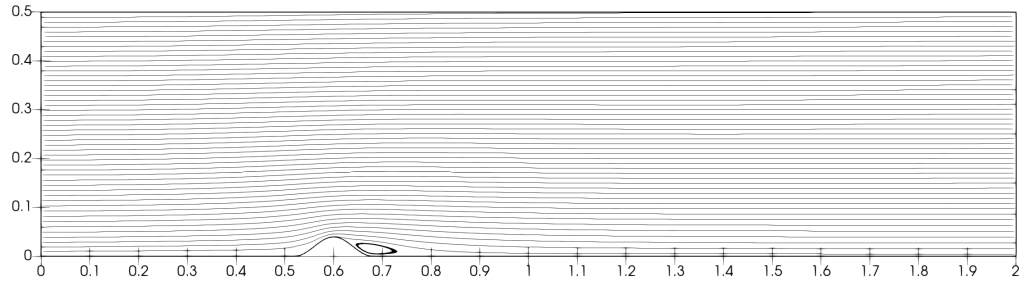

(a) Neutral

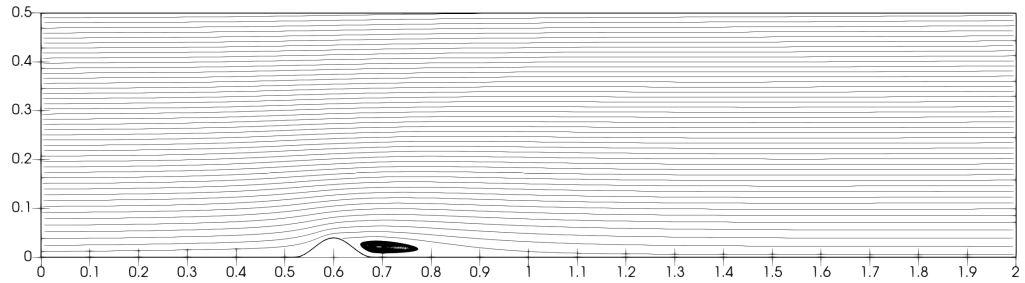

(b) Stable

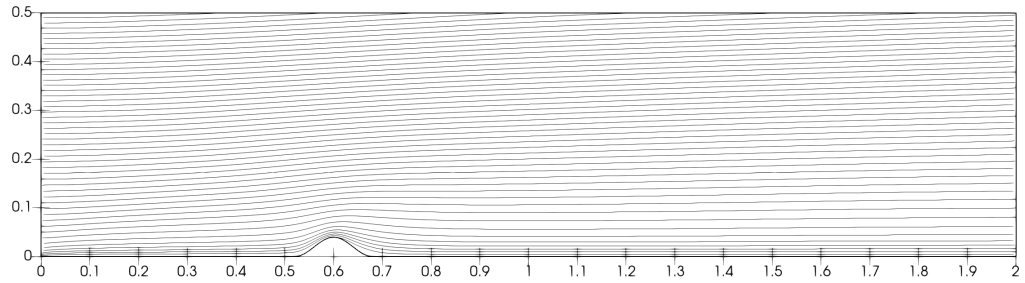

(c) Unstable

Figure 51: Stratification influence - streamlines

In the Figure 52 shows the vertical velocity component. It again confirms the above conclusions. A significant vertical movement is visible on the windward side with slower sloping behind the hill in stable stratification and the spread of the vertical movement along the whole domain can be seen in unstable stratification.

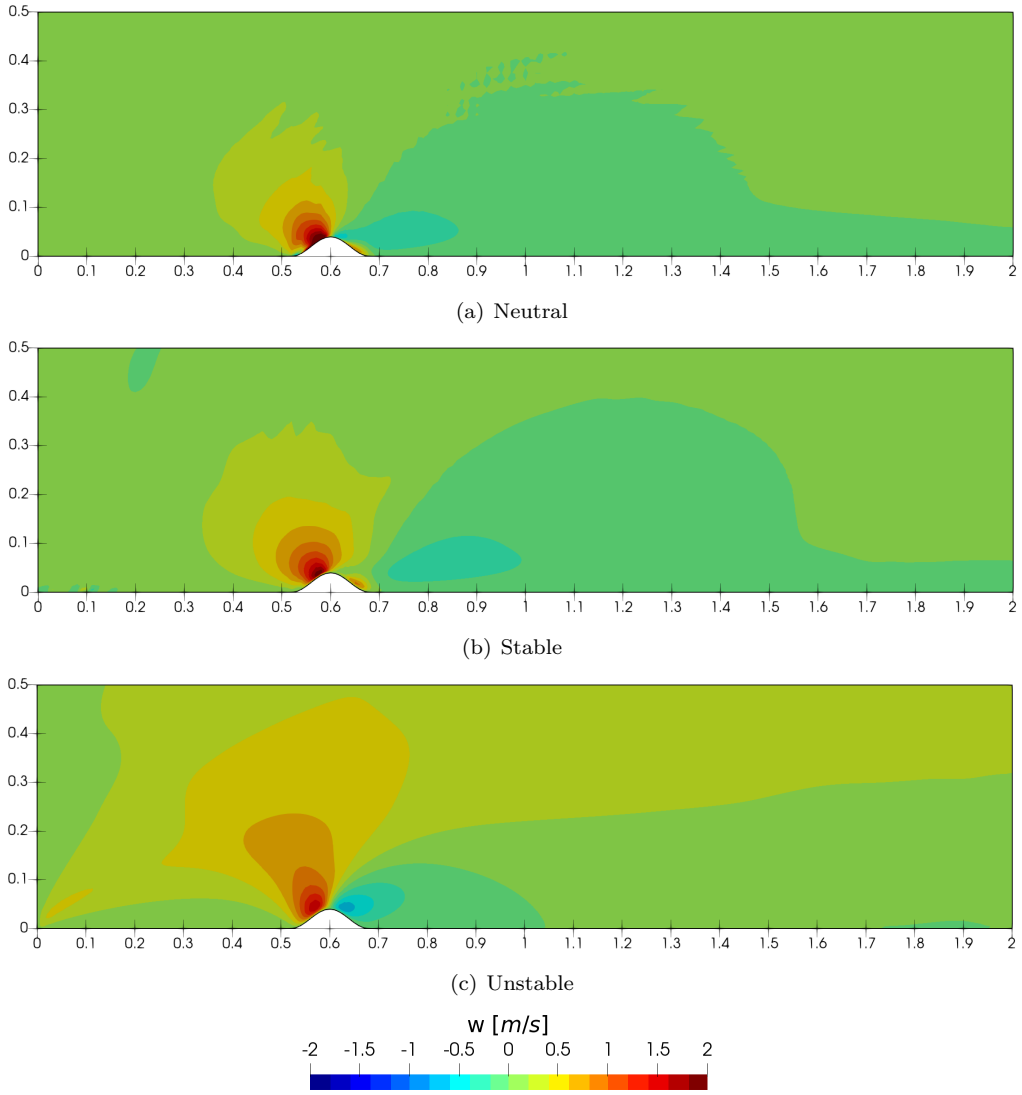

(a) Neutral

(b) Stable

(c) Unstable

Figure 52: Stratification influence - vertical velocity component w

To illustrate changes in turbulence properties due stratification, we present the kinematic viscosity ν fields. The contours of ν, including the constant laminar component $\tilde{\nu}$ and turbulent component ν_T, are depicted in Figure 53.

It is important to note that the kinematic viscosity of unstably stratified fluid is shown on different scale, that is 10 times higher than the scale used for neutral and stable stratification. Therefore, the turbulent viscosity ν_T of unstably stratified fluid is much larger than in the other cases. In the case of stable stratification, the increase in viscosity in slightly smaller than in the case of constant density. The cause of the differences is the impact of stabilization function G in the mixing length turbulence model. The verified and tested function increases or decreases the effect of the turbulence viscosity based on the type of stratification.

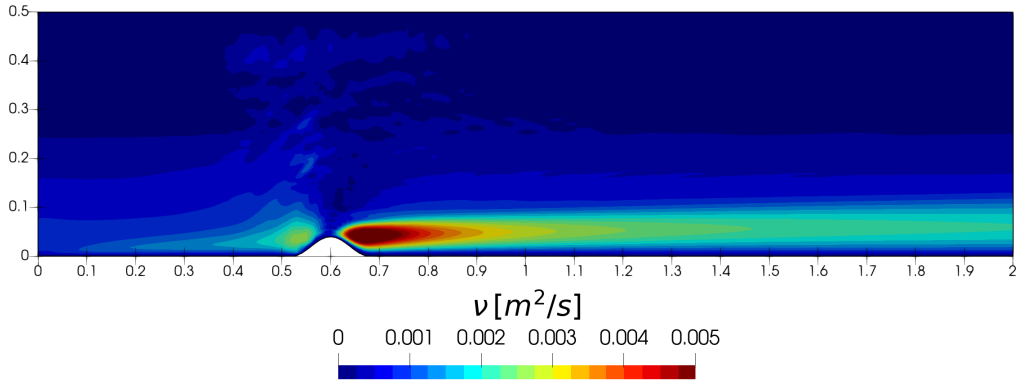

(a) Neutral

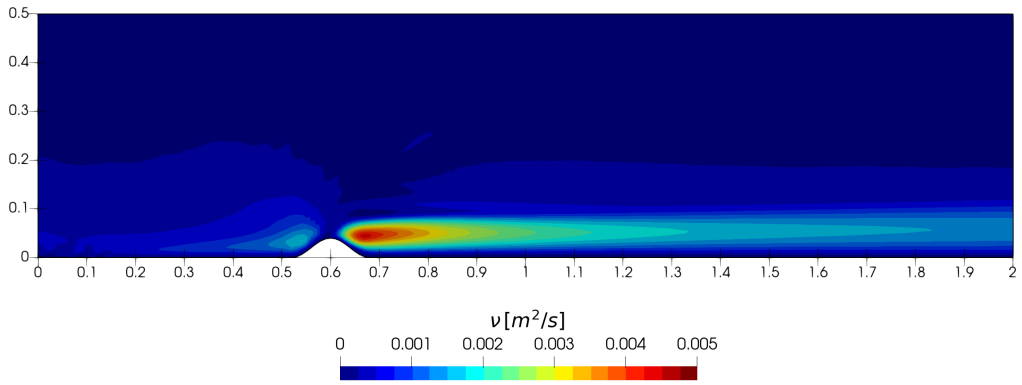

(b) Stable

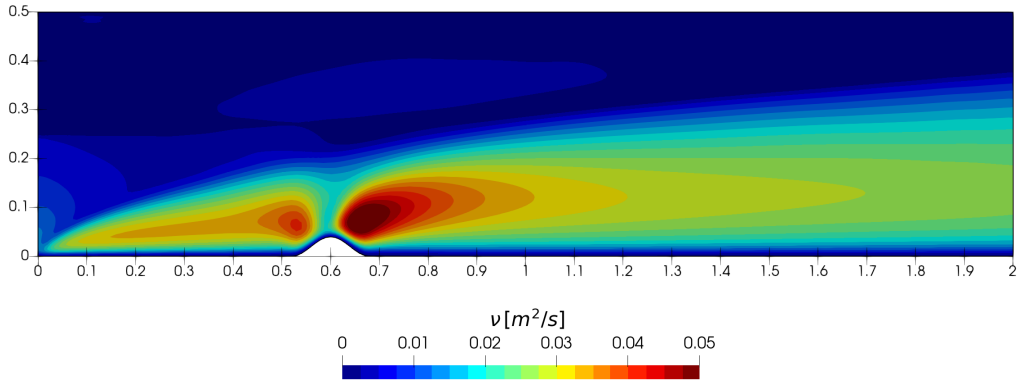

(c) Unstable

Figure 53: Stratification influence - kinematic viscosity ν fields, different scale

Kinematic viscosities on the same scales are shown in Figure 54. We see that at this scale the viscosity of neutral and stably stratified fluid appears almost constant. The turbulent component viscosity is negligible compare to the unstable stratified case.

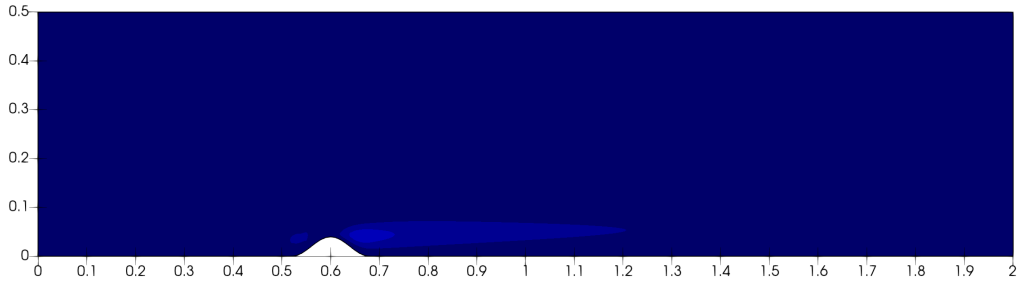

(a) Neutral

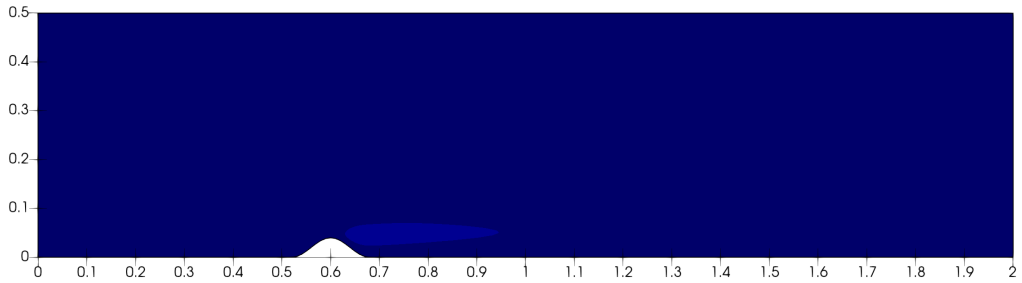

(b) Stable

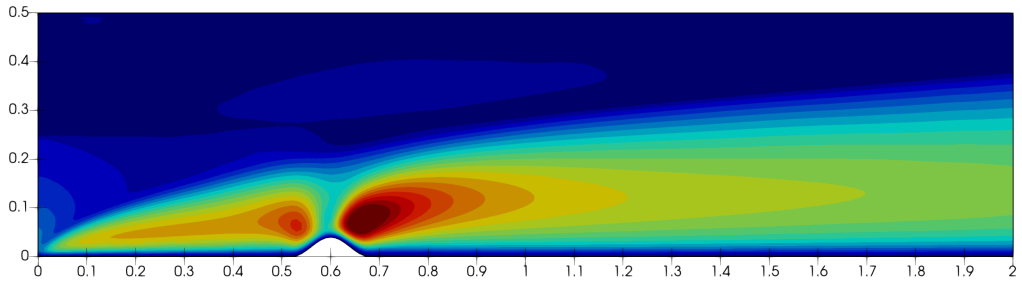

(c) Unstable

Figure 54: Stratification influence - kinematic viscosity ν fields, same scale

To complete the description of stratified fluid flows, density perturbations for each of the stratification types are depicted in Figure 55. In case of neutral stratification, the density perturbation is of course zero by definition, since the total density remains constant. On the contrary, stratified fluids both show visible but opposite action. In both cases, the density perturbation moves from the area of higher values of background density to the area of lower values.

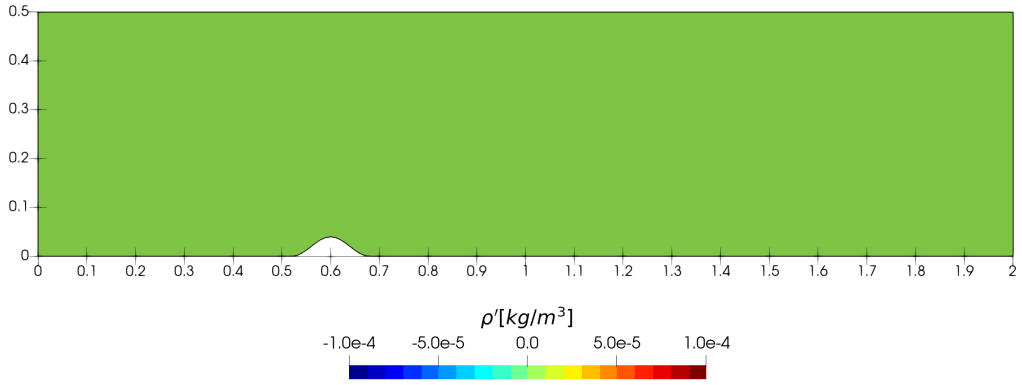

(a) Neutral

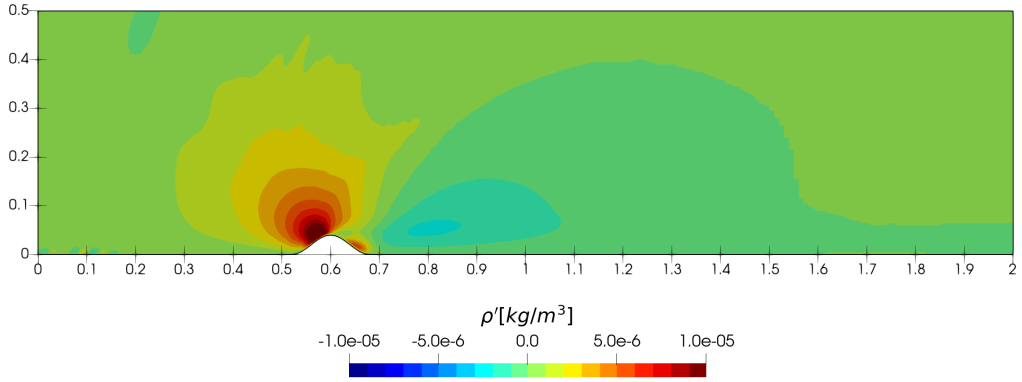

(b) Stable

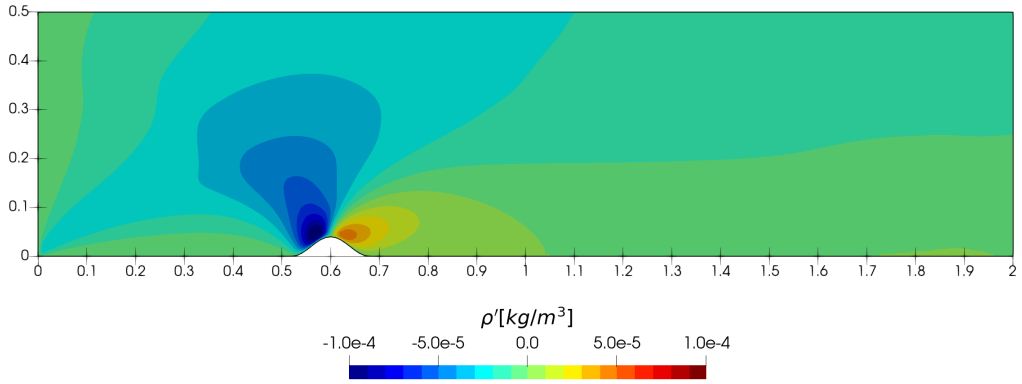

(c) Unstable

Figure 55: Stratification influence - density perturbation ρ' fields, different scale

Again, the scales of stable and unstable stratification differ by a factor of ten. For a better comparison, Figure 56 is presented, that highlights the significantly larger density perturbation in unstable stratification than in stable stratification where the perturbations are relatively negligible.

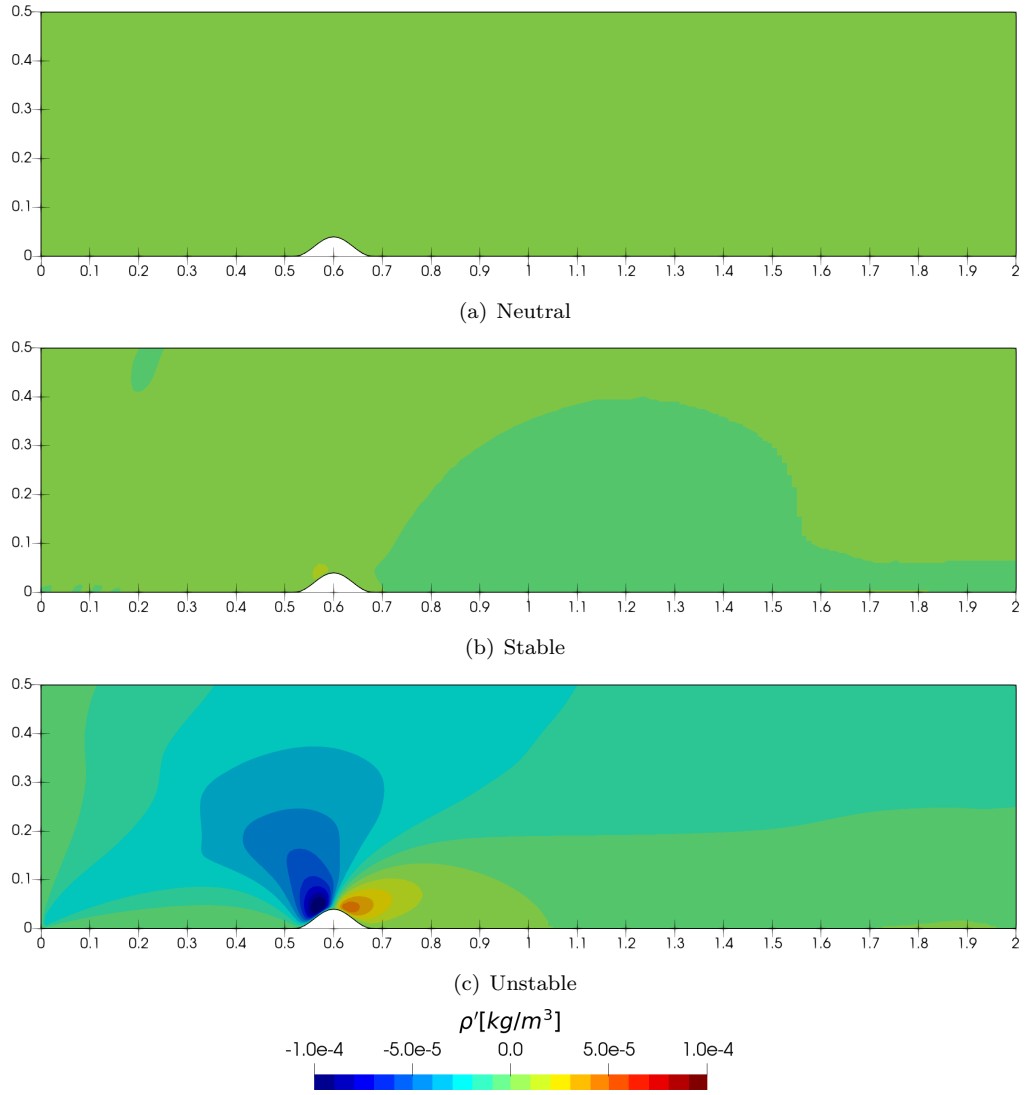

(a) Neutral

(b) Stable

(c) Unstable

Figure 56: Stratification influence - density perturbation ρ' fields, same scale

We have again provided some demonstrations of the effects of stratification. Although in many cases, the density gradient would be much smaller, the impacts should not be neglected, but rather be kept in mind when studying atmospheric flows.

In real nature, all types of stratification periodically occur in the atmosphere. All the situations and effect discussed above eventually combine. Therefore, the real situation is, as always, even more complex. However, by validating, comparing with experimental data, investigating and discussing the additional influences of numerical methods as well as effects of non-constant density, we have once again come a little closer to an accurate description of the atmospheric flows using mathematical modelling and numerical methods.

7 Conclusion & Remarks

This work has dealt with the subject of numerical simulations of atmospheric flows. All simulations have been conducted in a self-developed code from the ground up with all the described numerical methods implemented. It is a continuation of the preceding Bachelor's thesis. Therefore, it is a result of several years of work, which involved the theoretical study of the problem, pursuit of a deeper understanding of the physical phenomena in the atmospheric boundary layer, along with the efforts to derive and implement the mathematical model and apply the numerical methods. Not to mention the long hours of developing the custom code and resolving issues associated with it, and finally processing the results and the effort to present them in a structured and understandable way.

The beginning of the work has been devoted to the description of physical aspects of the atmospheric flows. Involving all complexities of the real nature situation and introducing the first simplifications made in order to model the problem virtually while maintaining practicality of the approach. Special attention has been given to the phenomenon of density stratification, that occurs in reality, but is commonly neglected in the literature and other simulations or experiments.

It has been followed by the mathematical description of the fluids flows with respect to the specifics of atmospheric boundary layer. Appropriate mathematical model involving the complete description of flows with modelling of turbulence and accounting even for the density stratification has been derived. The turbulence regime of the atmospheric flows was resolved using simple but elegant mixing length model, that when correctly implemented in the self-developed code has provided reasonably accurate and meaningful results.

The mathematical description has been extended by the section of numerical methods. That has provided explanation of the methods used: Finite Volume Method, Finite Difference Method for discretization and Artificial Compressibility Method to numerically resolve the equations. Description of the first mentioned involved a complete derivation of the discretization of the governing equations.

In the following sections, the results obtained from the simulations have been presented. First, validation of the solver has taken place. It involved two test cases, simple laminar channel flow and stratified fluid flow on a slope. The custom code has been successfully validated on both cases with different numerical methods. All performed simulations resulted in fully developed flows with velocity and density profiles consistent with the analytical solutions.

Therefore, the next section has approached more complex problems. An obstacle, representing a hill, has been introduced. Initially, the hill of simple geometry has been implemented in the laminar flow. Then, after demonstrating solid correlations between solutions using different numerical methods, a turbulent flow regime has been set up. Which has led to the main objective of the work: simulations of turbulent flows over various types of sinusoidal hills, representing simplified flow problems in the atmospheric boundary layer. The simulations have been compared to experimental data from wind-tunnel study of atmospheric flows.

Simulations using Finite Volume Method have accomplished a good agreement with the experimental data. After achieving corresponding results with the measurements, deeper investigation of the flows and numerical methods has been presented. It involved complete description of the computed fields, mesh-dependency discussion, study of boundary conditions influence and comparison of methods. Finally, the impacts of density stratification have been demonstrated to reflect the importance of wise choice of simplifications.

On the brighter side, apart from successful simulations using FVM, the effects of different hill shapes have been described in detail and the choice of the optimal mesh has been thoroughly discussed. In addition, more reality reflecting boundary conditions have been presented and the non-negligible impacts of stratification have been demonstrated. On the other hand, lack of success has occurred in the implementation of Finite Difference Method in turbulence flows, strongly different from other results. Moreover, numerical oscillations occurred in some cases. However, suggestions to resolve these problems have been provided and their implementation is considered to be high priority for any future work.

Nevertheless, to point out the progress from the preceding thesis, the work has been expanded by the turbulence modelling, Finite Volume Method, wall-fitted meshing, more sophisticated and realistic geometries and comparison with experimental data. Thus, a significant number of advances

and achievements have been made. Moreover, this work may serve as an inspiration for future works and authors to wisely choose simplifications and what approaches and mistakes to avoid.

Nevertheless, the main achievement is the good agreement with the experimental data. The numerical simulations performed with the self-developed code have provided accurate results that agree with the measurements and have lead to corresponding and meaningful conclusions. In addition, the significant impacts of density stratification in the atmospheric boundary layer have been demonstrated, as well as the emphasis on the suitable choice of parameters of numerical simulations.

In any case, the presented work also contains certain inadequacies that should be the objective of any future work. That concerns implementation of the dampening of the numerical simulations occurring in some of the results. Additional possible improvements could be to introduce more complex geometries, combination of hills with other obstacles, such as buildings or trees and extension of the simulations to three dimensions. In connection with that, more complex turbulence model could be introduced in order to compare the results or to correctly resolve more complicated problems. The use of commercial software for CFD simulations, could also be incorporated for comparison with the custom code to highlight the advantages and disadvantages of each approach.

The thesis, with its comprehensive physical description of atmospheric flows, formulation of mathematical model, description of numerical methods, validation of self-developed code and presentation of many numerical results fully meets the requirements of the assignment. All in all, the presented thesis has reached its goals and has served for the author as a tremendously valuable tool to obtain much deeper understanding of the fluid flows and helped to develop many useful skills applicable in engineering future.

References

[1] ANDERSON, J. D. *Fundamentals of Aerodynamics* atmosphere. Sixth edition. New York: McGraw-Hill Education. 2017, ISBN: 978-1-259-12991-9.

[2] BLACKADAR, A.K. The vertical distribution of wind and turbulent exchange in a neutral atmosphere. *Journal of Geophysical Research*, 67(8), 3095–3102, 1962.

[3] BODNÁR, T. *Numerical Simulation of Flows and Pollution Dispersion in Atmospheric Boundary Layer*. Thesis, Czech Technical University in Prague, 2003.

[4] BODNÁR, T. *Mathematical Modelling and Numerical Simulation of Mountain Canyon Flows*. Thesis, Czech Technical University in Prague, 2003.

[5] BOUSSINESQ, J. *Essai sur la théorie des eaux courantes*, volume Tome XXIII of *Memoires presentes par divers savants a l'Academie des Sciences de l'Institut National de France*. Imprimerie Nationale, Paris., 1877.

[6] CHASSAING, P., ANTONIA, R.A. ANSELMET, F. JOLY, L. and SARKAR, S. *Variable Density Fluid Turbulence*. Springer, 2002.

[7] CHENG, W.-CH., PORT'E-AGEL, F. A Simple Mixing-Length Model for Urban Canopy Flows *Boundary-Layer Meteorology*, 181, 1–9, 2021.

[8] CHORIN, A.J. A numerical method for solving incompressible viscous flows problems. *Journal of Computational Physics*, 2(1), 12–26, 1967.

[9] ESTOQUE, M. A., BHUMRALKAR, C. M. Flow over a localized heat source. *Monthly Weather Review*, 97(12), 850–859, 1969.

[10] FEISTAUER, M. and FELCMAN, J. and STRAŠKRABA, I. *Mathematical and Computational Methods for Compressible Flow* atmosphere. New York: Oxford University Press, Numerical mathematics and scientific computation, 2003, ISBN: 0-19-850588-4.

[11] FERREIRA, A. D., LOPES, A. M. G., VIEGAS, D. X. & SOUSA, A. C. M. Expermental and numerical simulation of flow around two-dimensional hills. *Journal of Wind Engineering and Industrial Aerodynamics*, 54/55, 173–181, 1995.

[12] FERREIRA, A. D., G., SILVA, M. C. G., VIEGAS, D. X. & LOPES, A. M. Wind tunnel simulation of the flow around two-dimensional hills. *Journal of Wind Engineering and Industrial Aerodynamics*, 38, 109–122, 1991.

[13] FLETCHER, C. A. J. *Computational Fluid Dynamics - The Basics with Applications*. McGraw-Hill, 1995.

[14] GARRATT, J. R. *The atmospheric boundary layer*. Cambridge atmospheric and space series. Cambridge University Press, 1992.

[15] HIRSCH, C. *Numerical computation of internal and external flows*, Volume 1: Fundamentals of Numerical Discretization. John Willey & Sons, 1988.

[16] HIRSCH, C. *Numerical computation of internal and external flows*, Volume 2: Computational Methods for Inviscid and Viscous Flows. John Willey & Sons, 1990.

[17] HUNT, J. C. R. & SNYDER, W. H. Experiments on stably and neutrally stratified flow over a model three-dimensional hill. *Journal of Fluid Mechanics*, 96(4), 671–704, 1980.

[18] KAIMAL, J. C. & FINNIGAN, J. J. *Atmospheric Boundary Layer Flows: Their Structure and Measurement* Oxford University Press, 1994.

[19] KIM, H. G, LEE, C. M., LIM, H. C. & KYONG, N. H. An experimental and numerical study on the flow over two-dimensional hills. *Journal of Wind Engineering and Industrial Aerodynamics*, 66, 17–33, 1997.

[20] KOZEL, K. & DVOŘÁK, R. *Matematické modelování v Aerodynamice* (in Czech) Mathematical modelling in Aerodynamics Vydavatelství ČVUT, 1996.

[21] KOZEL, K. *Numerické řešení parciálních diferenciálních rovnic* (in Czech). Numerical solution of partial differential equations Vydavatelství ČVUT, 2000.

[22] LEVEQUE, R. J. *Finite Difference Methods for Ordinary and Partial Equations*. Steady-State and Time-Dependent Problems Society for Industrial and Applied Mathematics, 2007, ISBN: 978-0-898716-29-0

[23] LIONS, P. L. *Mathematical Topics in Fluid Mechanics: Volume 1: Incompressible Models*, Oxford Lecture Series in Mathematics and Its Applications Oxford University Press, 1996, ISBN: 0-19-851487-5

[24] LONG, R. R, The motion of fluids with density stratification. *Journal of Geophysical Research*, 64(12), 2151–2163, 1959.

[25] MACCORMACK, R. W. The Effect of Viscosity in Hypervelocity Impact Cratering. *AAIA Paper*, 69–354, 1969.

[26] MAHRT, L. Stably Stratified Atmospheric Boundary Layers *Annual Reviews of Fluid Mechanics*, 46, 23-45, 2014.

[27] PESKIN, CH. S. Numerical analysis of blood flow in the heart. *Journal of Computational Physics*, 25(3), 220–252, 1977.

[28] PHILLIPS, O. M. On fluids induced by diffusion in a stably stratified fluid. *Deep Sea Research*, 17, 435–443, 1970.

[29] PIRKL, L. *Numerical Simulation of Incompressible Flows with Variable Viscosity*. Thesis, Czech Technical University in Prague, 2007.

[30] PRANDTL, L. The mechanics of viscous fluids. In W. F. Durand, editor, *Aerodynamic Theory*, volume III., chapter G., pages 35–208. Julius Springer, 1935.

[31] REYNOLDS, O. On the dynamical theory of incompressible viscous fluids and the determination of the criterion. *Philosophical Transactions of the Royal Society of London. (A.)*, 186, 123–164, 1895.

[32] SCHETZ, J. A. & FUHS, A. E. *Fundamentals of fluid mechanics*. John Wiley & Sons, 1999.

[33] SMEDMAN, AS. TJERNSTRÖM, H. & HÖGSTRÖM U. Analysis of the turbulence structure of a marine jet. *Boundary Layer Meteorology*, 66, 105–126, 1993.

[34] SPIEGEL, E.A. & VERONIS, G. On the boussinesq approximation for a compressible fluid. *Astrophysical Journal*, 131, 442–447, 1960.

[35] SULLIVAN, P. P. MCWILLIAMS, J. C. & MOENG, C.-H. A subgrid-scale model for large-eddy simulation of planetary boundary-layer flows. *Boundary-Layer Meteorology*, 71(3), 247–276, 1994.

[36] UHLÍŘ, V. *Numerical solution of stratified fluids flows*. Bachelor's thesis, Czech Technical University in Prague, 2021. (in Czech).

[37] VIOLLET, P.-L. *Méchanique des fluides à masse volumique variable*. Paris: Presses de l'Ecole Nationale des Ponts et Chaussées, 1997.

[38] WYNGAARD, J.C. *Turbulence in the Atmosphere*. Cambridge University Press, 2010.